INVESTIGATION OF FLYING QUALITIES OF MILITARY AIR-
CRAFT AT HIGH ANGLES OF ATTACK. VOLUME I. TECHNICAL
RESULTS

Donald E. Johnston, et al

Systems Technology, Incorporated

Prepared for:

Air Force Flight Dynamics Laboratory

June 1974

AFFDL-TR-74-61

INVESTIGATION OF FLYING QUALITIES OF MILITARY AIRCRAFT AT HIGH ANGLES OF ATTACK

Volume I: Technical Results

SYSTEMS TECHNOLOGY, INC.
HAWTHORNE, CALIFORNIA

TECHNICAL REPORT AFFDL−TR−74−61

JUNE 1974

Approved for public release; distribution unlimited.

AIR FORCE FLIGHT DYNAMICS LABORATORY
AIR FORCE SYSTEMS COMMAND
WRIGHT−PATTERSON AIR FORCE BASE, OHIO 45433

NOTICE

When Government drawings, specifications, or other data are used for any purpose
other than in connection with a definitely related Government procurement operation,
the United States Government thereby incurs no responsibility nor any obligation
whatsoever; and the fact that the government may have formulated, furnished, or in
any way supplied the said drawings, specifications, or other data, is not to be
regarded by implication or otherwise as in any manner licensing the holder or any
other person or corporation, or conveying any rights or permission to manufacture,
use, or sell any patented invention that may in any way be related thereto.

This report has been reviewed and cleared for open publication and/or public
release by the appropriate Office of Information (OI) in accordance with
AFR 190-17 and DODD 5230.9. There is no objection to unlimited distribution of
this report to the public at large or by DDC to the National Technical Information
Service (NTIS).

This technical report has been reviewed and is approved for publication.
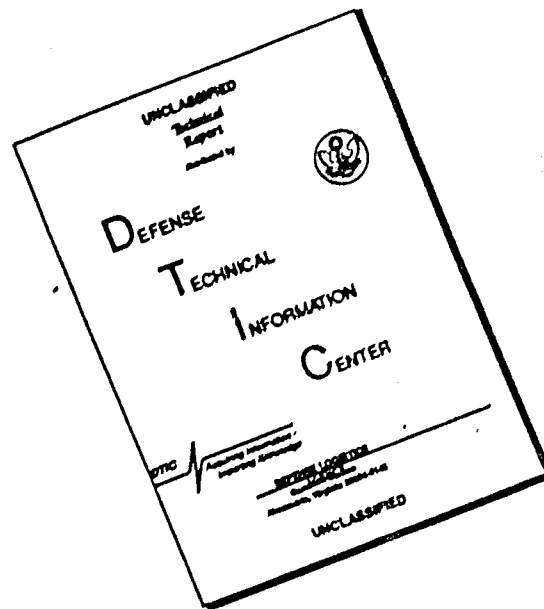
FOR THE COMMANDER:

D.R. Mayhew

DAVID R. MAYHEW
Project Engineer

E. H. FLINN, Acting Chief,
Control Criteria Branch
Flight Control Division
Air Force Flight Dynamics Laboratory

Copies of this report should not be returned unless return is required by security
considerations, contractural obligations, or notice on a specific document.

DISCLAIMER NOTICE

REPORT DOCUMENTATION PAGE		READ INSTRUCTIONS BEFORE COMPLETING FORM
1. REPORT NUMBER AFFDL-TR-74-61	2. GOVT ACCESSION NO.	3. RECIPIENT'S CATALOG NUMBER
4. TITLE (and Subtitle) Investigation of Flying Qualities of Military Aircraft at High Angles of Attack, Vol. I: Technical Results		5. TYPE OF REPORT & PERIOD COVERED Final Report 1 March 1973-1 March 1974
		6. PERFORMING ORG. REPORT NUMBER TR-1033-1
7. AUTHOR(s) Donald E. Johnston Irving L. Ashkenas Jeffrey R. Hogge		8. CONTRACT OR GRANT NUMBER(s) F33615-73-C-3101
9. PERFORMING ORGANIZATION NAME AND ADDRESS Systems Technology, Inc. 13766 S. Hawthorne Blvd. Hawthorne, California 90250		10. PROGRAM ELEMENT, PROJECT, TASK AREA & WORK UNIT NUMBERS Project 1917 Task 191700
11. CONTROLLING OFFICE NAME AND ADDRESS AFFDL/FGC		12. REPORT DATE June 1974
		13. NUMBER OF PAGES 159
14. MONITORING AGENCY NAME & ADDRESS(if different from Controlling Office)		15. SECURITY CLASS. (of this report) UNCLASSIFIED
		15a. DECLASSIFICATION/DOWNGRADING SCHEDULE

16. DISTRIBUTION STATEMENT (of this Report)

Approved for public release, distribution unlimited.

17. DISTRIBUTION STATEMENT (of the abstract entered in Block 20, if different from Report)

18. SUPPLEMENTARY NOTES

19. KEY WORDS (Continue on reverse side if necessary and identify by block number)

Stall
Departure
Handling qualities
Stability and control

20. ABSTRACT (Continue on reverse side if necessary and identify by block number)

Attention has been focused on departure (e.g., nose slice, wing rock) and recovery as opposed to spin entry. The approach has been to analytically identify and validate key flying quality parameters, to qualitatively assess and verify these through piloted simulation, and to measure and quantify effects on key dynamic parameters of pilot describing functions.

Flying qualities are influenced by open- and closed-loop parameters. Most past studies have concentrated on open-loop parameter contributions and on symmetric

DD FORM 1473 EDITION OF 1 NOV 65 IS OBSOLETE   UNCLASSIFIED

20. Abstract (Concluded)

($\beta=0$) aircraft trim conditions. Since the pilot is generally in active
control when departure occurs, this study places most emphasis on key
closed-loop parameters and recognizes that, at high α, it is common for
sideslip to exist either intentionally (e.g., rudder maneuvering) or
unintentionally (e.g., adverse aileron yaw, mistrim, etc.). As a direct
result, new open- and closed-loop parameters are identified which relate
to nose slice departures and to wing rock. Physical insight to the
phenomena is achieved by tracking through the root aerodynamic flow,
effective stability derivative, equation of motion, and transfer function
relationships.

The influence of the parameters on departure and recovery characteristics
was validated in a fixed-base simulation utilizing a nonlinear five-degrees-
of-freedom airframe model and a head-up air-to-air tracking task. Results
indicate the departure to be influenced primarily by the new closed-loop
parameters while recovery is influenced by a combination of open-loop
parameters and severity of the initial departure.

FOREWORD

TABLE OF CONTENTS

LIST OF FIGURES

LIST OF TABLES

LIST OF SYMBOLS

a_y	Lateral acceleration at c.g. (ft/sec^2)
a_{y_c}	Lateral acceleration at cockpit (g)
a_{z_c}	Normal acceleration at cockpit (g)
AR	Amplitude ratio
A	Coefficient of highest order term in polynomial
A_k	Amplitude of kth sine wave of the Describing Function Analyzer forcing function
AF	Airframe
b	Wing span (ft)
c	Wing chord (ft)
$\bar{c}$	Mean aerodynamic chord (ft)
C_ℓ	Aerodynamic non-dimensional rolling moment coefficient
$C_\ell(\alpha, \beta, \delta_e)$	Non-dimensional rolling moment coefficient as a function of α, β, and δ_e — body axis system
C_{ℓ_i}	$\partial C_\ell / \partial i$
C_m	Aerodynamic non-dimensional pitching moment coefficient
C_{m_i}	$\partial C_m / \partial i$
C_n	Aerodynamic non-dimensional yawing moment coefficient
$C_n(\alpha, \beta, \delta_e)$	Non-dimensional yawing moment coefficient as a function of α, β, and δ_e — body axis system
C_{n_i}	$\partial C_n / \partial i$
$C_{n_{\beta dyn}}$	$C_{n_\beta} - (I_z/I_x)\alpha C_{\ell_\beta}$
D	Aerodynamic drag (lb)
DOF	Degree of freedom
$e(t)$	Time dependent error
$E(j\omega_k)$	Frequency dependent error

g	Gravitational acceleration constant
h	Altitude (ft)
i	State variable, e.g., α, β, θ, etc.
$i(t)$	Input, function of time
I_x, I_y, I_z	Moments of inertia referred to aircraft body centerline axis (slug-ft^2)
I_{xz}	Product of inertia referred to aircraft body centerline axis
$j\omega$	Imaginary part of Laplace transform variable $s = \sigma + j\omega$
K_θ	Pitch attitude feedback gain
K_φ	Roll attitude feedback gain
K_{p_i}	Pilot gain in closing the i loop
ℓ_i	Moment arm or distance from aircraft c.g. along body axis defined by subscript
L	Aerodynamic lift (lb)
$\mathcal{L}$	Aerodynamic rolling moment about aircraft body (centerline) axis
$\mathcal{L}'_i$	Total incremental change in rolling acceleration due to incremental change in state variable quantity
m	Mass
$m(t)$	System output, function of time
M	Mach number
M	Pitching moment about aircraft body axis
M_i	$(\partial M/\partial_i)\,(1/I_y)$
n_z	Normal load factor (g)
N	Yawing moment about aircraft body axis
N'_i	Total incremental change in yawing acceleration due to incremental change in state variable quantity
N^i_j	Vehicle transfer function numerator relating output, i, to control deflection, j, (i = p, q, r, etc.; j = δ_a, δ_e, δ_r)

$N_{j_1 j_2}^{i_1 i_2}$	Vehicle transfer function coupling numerator particularized by superscripts and subscripts
$N_j^{i}{}'$	Primed numerator indicates that inner loop closed previously affects the quantity considered
p	Perturbed roll angular velocity about body x-axis
P	Total roll rate about x-axis
q	Perturbed pitch angular velocity about body y-axis
Q	Total pitch rate about y-axis
$\bar{q}$	Dynamic pressure (lb/ft^2)
r	Perturbed yaw angular velocity about body z-axis
R	Total yaw rate about z-axis
s	Laplace operator ($\sigma \pm j\omega$)
S	Aircraft wing area (ft^2)
TEU	Trailing edge up
t	Time
t_R	Run time (sec)
T	Thrust (lb)
T_p	First order time constant of the overdamped phugoid mode
T_q	First order time constant of the pitch rate numerator
T_r	First order time constant of the yaw rate numerator
T_R	First order time constant of the roll subsidence mode
T_s	First order time constant of the spiral divergence mode
T_{θ_1}, T_{θ_2}	First order time constants of the conventional low and high frequency zeros of the pitch attitude numerator
T_{θ_3}	First order time constant of the pitch attitude numerator which results from unsymmetric flight
T_{ϕ_1}, T_{ϕ_2}	First order time constants of the overdamped roll attitude numerator
$T_{\theta\phi_1}$, $T_{\theta\phi_2}$	First order time constants of the coupling numerator $N_{\delta_e \delta_a}^{\theta \phi}$

u	Perturbed linear velocity component along x axis (ft/sec)
U_o	Steady state velocity component along x-axis (ft/sec)
V_T	Total velocity along wind or path axis (ft/sec)
w	Perturbed linear velocity along z axis (ft/sec)
W	Weight (lb)
x_{cg}	Location of aircraft c.g. along body fixed x-axis
X, Y, Z	Aerodynamic forces along an axis system with the x axis aligned with the total velocity vector, the z axis in the aircraft plane of symmetry pointing down, and the y axis orthogonal to the x and z axes and positive out the right wing
X_i, Y_i, Z_i	$[\partial(\ )/\partial_i] /m$
Y_c	Controlled element transfer function
Y_{p_i}	Pilot describing function as particularized by subscript
α	Angle of attack
β	Sideslip angle
γ	Flight path angle
δ_i	Surface deflection particularized by subscript
Δ	Transfer function denominator
ζ_i	Damping ratio particularized by subscript
φ, θ, ψ	Conventional perturbed attitude angles
Φ, Θ, Ψ	Conventional Euler angles between gravity-oriented inertial axis and aircraft body axis
ξ	Angle between thrust axis and aircraft centerline x axis
σ	Real part of Laplace transform variable
$\omega(\ )$	Natural frequency of the denominator or numerator root particularized by the subscript

Math Symbols

$(\dot{\ })$	d/dt
$\angle$	Phase angle
dB	Decibels, $20 \log_{10}(\ \ )$
∂	Partial Derivative
$<$	Less than
$>$	Greater than
$\longrightarrow$	Feedback to

Subscripts

a	Aileron
d	Dutch roll
e	Elevator
o	Initial trim value
p	Phugoid
r	Rudder
s	Spoiler
sp	Short Period
SR	Coupled spiral-roll-subsidence (lateral phugoid)
T	Target
R	Right
L	Left

SECTION I

INTRODUCTION

Modern and advanced military aircraft often fly at high, near-stall angles of attack in tactical operations and "normal" maneuvering. In fact, superior flight characteristics in this marginal regime are key effectiveness factors in the world of fighter and fighter-bomber competitions and contests. They are also central issues in survival, since slight miscues at these boundary conditions can lead to out-of-control departures and spins. High performance aircraft are often very difficult to recover from such situations, so the loss of control can be very dangerous.

Unfortunately, understanding of high-angle-of-attack flight is not compatible with its level of operational importance. A variety of uncontrolled high-angle-of-attack dynamic phenomena have been observed and catalogued; some have been analyzed for underlying physical causes. However, there is little present appreciation and quantification of the impact of root deficiencies in high-angle-of-attack aircraft dynamics on pilot-controlled flying qualities just before, during, and just after stall departure. For instance, analytical methods for efficient treatment of the total pilot/aircraft system have not been applied specifically to high-angle-of-attack flying qualities problems. Most criteria have evolved from open-loop (airframe alone) considerations yet departure itself represents a dividing line in the nature of the approaches necessary to modeling and analysis requirements. Before departure the control situation is primarily regulatory, closed loop; after departure, the control situation through recovery is ideally time-optimal programmed (i.e., largely open-loop). In view of the newly re-recognized importance of high-angle-of-attack flight, and because the application of the general pilot/vehicle systems analysis methods to the attendant closed-loop control problems is very promising, the time for a breakthrough in understanding was considered to be at hand.

The specific goals of this program were:

- Enhanced understanding of high angle-of-attack open- and closed-loop dynamic phenomena

- Identification of key effective controlled element flying quality parameters

- Improved appreciation for interactions between high angle-of-attack flying qualities, controlled element dynamics, and pilot technique

- Definition of multi-input, multi-output pilot models appropriate in the stall/departure/recovery phases of flight

- Development and validation of quantitative design guides and criteria relevant to stall/departure/ recovery

- Formulation of an automated closed-loop pilot/vehicle digital design analysis methodology

- Recommendations for further work and approaches to be taken by the AFFDL

With the exception of the automated digital closed-loop pilot/vehicle design analysis method, all of these goals have been attained.

Attention has been focused on departure (e.g., nose slice, wing rock) and recovery as opposed to spin entry and recovery. The approach has been to analytically identify and validate key flying quality parameters, to qualitatively assess and verify these through piloted fixed-base simulations, and to measure and quantify effects on key dynamic parameters of pilot describing functions.

Flying qualities are influenced by open- and closed-loop parameters. Most past studies (e.g., Refs. 1-4) have concentrated on the open-loop lateral-directional parameter contributions (e.g., $N_{\beta_{dyn}}$, $\mathcal{L}'_\beta$, N'_p, $\mathcal{L}'_p$) although some recognition has been given to the closed-loop parameters ω_ϕ and ω_d (e.g., Refs. 5 and 6). These efforts have also focused on symmetric ($\beta = 0$) aircraft trim conditions.

2

The key parameters investigated in this program are identified in Table 1. Since the pilot is generally in the loop when departure occurs, we place most emphasis on key closed-loop parameters and then relate these to open-loop parameters (which in this case are aircraft stability derivatives). Several of these parameters are new and result primarily from recognizing that, at high α, it is common for sidelip to exist either intentionally (e.g., rudder maneuvering) or unintentionally (e.g., adverse aileron yaw, mistrim, etc.). As a direct result the new open- and closed-loop parameters have been identified which evolve from longitudinal-lateral coupling associated with unsymmetric flight. These new parameters relate to the zeros $(1/T_{\theta_3}, \omega_\theta)$ of the pitch attitude transfer function reaching unfavorable locations at angles-of-attack below that for stall and at relatively small sideslip angles. Conventional feedback of pitch attitude (or rate) to elevator (either automatic or manual) then produces a coupled longitudinal-lateral divergence known as nose slice.

The Section II analysis is focused primarily on the A-7 aircraft which exhibits a severe nose slice departure characterized by large rapid yaw followed by rapid roll. Limited analysis and simulation of the F-4 wing rock is also reported. Physical insight to the nose slice phenomena is achieved by tracing through the equation of motion, effective stability derivative, transfer function, and root aerodynamic flow relationships. Eighth order transfer functions are obtained for all state variables for a sweep of α and β in the vicinity of stall. It is found that the pitch

TABLE 1

KEY PARAMETERS INVESTIGATED

DEPARTURE CHARACTERISTIC	PARAMETERS INVESTIGATED	
	CLOSED-LOOP	OPEN-LOOP
Nose Slice	$1/T_{\theta_3}$, ω_θ ω_{SR} , ω_p	N'_α , $\mathcal{L}'_\alpha$, Z_p , Z_r $N_{\beta_{dyn}}$
Wing Rock	$\zeta_d \omega_d$, ω_p/ω_d	nonlinear N_β N'_p , $\mathcal{L}'_p$, $\mathcal{L}'_\beta$ M_β

attitude numerator undergoes a marked change with non-zero β in which one root becomes non-minimum phase (moves into the right half plane of a conventional root locus plot). This portends a closed loop instability. The cause of this right half plane zero is traced through the 9 x 9 equation of motion matrix to the dominant coupling terms. Two of these, $\mathcal{L}'_\alpha$ and N'_α, are aerodynamic while the other two, Z_p and Z_r, are kinematic coupling.

The potential closed-loop unstable mode is identified as a first order lateral-directional divergence despite its appearance in a longitudinal numerator. The phenomenon is verified by open- and closed-loop time histories obtained from nonlinear six degree-of-freedom digital and five degree-of-freedom analog simulations using nonlinear aerodynamic coefficents. The results are further validated in a fixed base piloted simulation using the five degree-of-freedom nonlinear airframe model. Section III contains a description of the simulation including head-up display, tracking tasks and pilot parameter measurements.

Nine aircraft dynamic configurations are employed in the departure/recovery flying quality assessment simulation. These and the simulation results are analyzed in Section IV. An in-trail target-tracking task was flown by two USAF test pilots experienced in the A-7. This task led the subjects into a level, 1 g, stall departure. Initial values of each of the parameters of Table 1 were varied to provide the nine departure/recovery characteristics ranging from mild to severe nose slice and with one providing a tendency to wing rock.

Analytic predictions are validated; however, resolution of pilot commentary required additional analysis which led to further identification and separation of key parameter effects and possible analytic predictive techniques. Departure characteristics are found to be determined by the closed-loop parameters of Table 1. Recovery techniques are found to be in agreement with A-7 flight results and the preferred method is release of all controls; however, in some cases application of forward stick is acceptable. Therefore recovery characteristics are strongly influenced by the open-loop parameters of Table 1. Departure characteristics and piloting technique also highly influence recovery.

4

Pilot/vehicle describing function measures and pilot dynamic models obtained for three incipient departure conditions are summarized in Section V. The task is again representative of a situation in which aircraft stall is inadvertently approached and the pilot is attempting to maintain track without inducing aircraft departure. Describing function measures were obtained for multiloop, pitch, roll, and heading tracking tasks. The crossover model was found to be valid for each loop closure. The precision pilot model provided an excellent fit to the data except that in pitch the crossover was close to the longitudinal short-period mode and required the pilot to adopt a second-order lead equalization approximately the inverse of the longitudinal short period. The gain and low-frequency lag-lead equalization employed in the roll loop closure was found to differ depending upon whether the roll loop was an outer (roll tracking) or inner (heading tacking) loop. Coupling between the airframe lateral and longitudinal dynamics was found to increase the pilot workload but did not appreciably affect the equalization employed.

The one goal not achieved — the automated digital closed-loop pilot/vehicle design analysis method — was set forth as a continuation and multi-input, multi-output extension of the various "paper pilot" models (Refs. 7, 8, and 9). As such it was anticipated to draw on the existing data base relating pilot ratings with first-order lead generation requirements and task performance measures in establishing a rating functional. However, this preconceived concept did not fully recognize the grossness of the maneuvers, pilot control activity, and performance measures associated with stall/departure/recovery phases of flight. Departure is, by definition, the attainment of aircraft motion uncommanded by the pilot, i.e., loss of control. The motion is generally large and rapid. It is found in this study that departure (nose slice or wing rock) is severely aggravated, if not caused, by closed-loop pilot-vehicle interaction. With the possible exception of holding forward stick, recovery is best achieved by the pilot releasing all controls. Any other control activity during recovery greatly aggravated the departure/recovery maneuver. The pilot ratings received for closed-loop recovery were therefore much higher (worse) than for open-loop airframe-alone recovery. Thus a pilot-centered function is not applicable to recovery.

In the pre-departure phase where closed-loop considerations are valid, it was found the the pilot adopts a second-order lead in pitch attitude control — apparently in an attempt to cancel short period pitch attitude excursions which might trigger departure. This second-order complex lead generation has been observed before (Refs. 10 and 11); however, there are insufficient pilot rating data to establish a functional. The only other known rating data is in Ref. 10 and it, together with the data obtained herein, provides essentially no rating spread. The vast amount of data obtained for first-order lead generation is not applicable. Thus at this point it appears a paper pilot design function is somewhat premature.

Nevertheless, a pilot model of a different sort has been obtained for the high-angle-of-attack, pre-departure flight phase. However, much more data is required before trends can be established between pilot parameters, pilot ratings, and performance measures.

A key problem with ratings exists because loss of control is involved. That is, accomplishment of the primary task, whatever it may be, has resulted in the aircraft approaching stall/departure. If the task is pursued, it presumably will result in departure — loss of control. Departure prevention then requires abandonment of the primary task and shifting full priority to safety of flight. Thus Level 3 flying qualities[*] are involved and the problem arises of establishing the Level 3 boundary, i.e., loss of control. On the Cooper-Harper (Ref. 13) scale this is the boundary between 9 and 10 (there is no 9.5). If an airplane will depart, then there is no question regarding the existence of the Cooper-Harper boundary, but merely a question of how much of the potential flight envelope must be traded for flight safety. Thus a mission performance, usable load factor, flight safety, or some related index becomes paramount.

---

[*]From Ref. 12, Level 3:

"Flying qualities such that the airplane can be controlled safely, but pilot workload is excessive or mission effectiveness is inadequate, or both. Category A Flight Phases can be terminated safely, and Category B and C Flight Phases can be completed.

In summary, the study reported herein was intended to unify into a systematic framework a wide variety of empirical, analytical, and theoretical data into analytical models which describe high-angle-of-attack aircraft dynamics and flying qualities. Besides providing the basis for enhanced knowledge, this work also was intended to develop and validate quantitative design guides and associated flying qualities and flight test criteria relevant to the stall/departure/recovery regime. Spin aspects are specifically excluded. However, because of the complexity involved in non-linear aerodynamics and multi-input, multi-output pilot characteristics, the effort has been a comprehensive and systematic first cut. It is anticipated that the insight and initial flying qualities results provided will serve in planning a longer-term program which attacks the overall problem of stalls and spins.

SECTION II

SYSTEMS ANALYSIS IDENTIFICATION OF KEY PARAMETERS

A. NOSE SLICE

This section presents the analytical development of and possible
physical explanation for new open- and closed-loop parameters which appear
to underlie the nose slice departure of the A-7 aircraft. The initial
analysis is based on a nonlinear six-degree-of-freedom digital model which
incorporates lookup table aerodynamic coefficients as functions of α, β,
and δ_e. A succession of fixed operating point, partial derivative
expressions and linearized transfer function evaluations over a range of
angles of attack and sideslip provided the initial clues to potential key
parameters. Open- and closed-loop time responses were then obtained for a
nonlinear six-degree-of-freedom digital and a simplified five-degree-of-
freedom analog simulation. These models are validated via comparisons with
actual flight traces of an A-7 departure. The closed-loop nose slice diver-
gence phenomena is traced through effective stability derivatives and related
to previous aerodynamic flow studies.

1. Trim Conditions

Low Mach aero data developed by the manufacturer were supplied by the
USAF Flight Dynamics Laboratory. These data cover the range $0 < \alpha < 90°$ and
$-20° < \beta < +20°$. The data supplied by the SAF was in stability axes, and
was transformed into body centerline axes for this analysis and simulation.
Volume II contains the body axis data.

Trim conditions for this analysis and simulation are as follows

$$W = 22,299 \text{ lb} \qquad \gamma_0 = \Phi_0 = 0$$
$$h = 13,200 \text{ ft} \qquad \text{Landing gear — Up}$$
$$x_{cg} = 29.6\% \text{ MAC} \qquad \text{Flaps — Up}$$

The velocity was varied to obtain an angle-of-attack range $10 < \alpha < 24$ deg. Since the clean aircraft stalls at $\alpha \doteq 21$ deg, this range provided an ample view of the vehicle dynamic characteristics before, through, and following stall. It was subsequently determined that an α range of from 17 to 24 deg is adequate to demonstrate departure/recovery characteristics for this aircraft.

The linearized, fixed operating point derivatives and transfer function factors were obtained through use of standard digital programs. These programs utilize the equations of motion summarized in Fig. 1 and the nonlinear lookup table aero data of Appendix II. The programs trim the aircraft to the specified flight condition, perturb each of the state variables to obtain the partial (stability) derivatives, and compute the specified transfer function factors.

The initial analysis at $\beta = 0$ showed rather conventional uncoupled dynamic characteristics and provided no clues to a nose slice type departure. The tabulated data in Appendix III show that dutch roll frequency decreases and damping increases as angle of attack is increased. The conventional roll subsidence and spiral modes couple into a lateral-oscillation (hereafter termed "lateral phugoid") that eventually becomes divergent between 20 and 21 deg angle of attack. Longitudinal dynamics are well behaved with no indication of pitch-up or other longitudinal departure characteristics.

Because of these "negative" results for $\beta = 0$ and because previous exposure to the A-7 (Ref. 14) indicated that some models had a pronounced tendency to change in directional trim during accelerating or decelerating flight, the effect of non-symmetrical flight was investigated. Six-degree-of-freedom transfer function factors for three sideslip values at $\alpha \doteq 19$ deg are shown in Table 2. It may be noted from the characteristic equation (Δ) factors that the open-loop longitudinal modes are little affected by sideslip. The major influence is on the open-loop lateral directional modes. Increasing sideslip causes the roll subsidence and spiral to couple into a lateral oscillation much as does increasing angle of attack. The damping of the lateral phugoid decreases with increasing β and goes unstable between 6 and 15 deg of sideslip. Comparing the dutch roll and lateral phugoid, it appears that there is an interchange in damping between these modes. That is, as sideslip increases, damping of the dutch roll increases while that of the lateral-phugoid decreases.

$$\dot{\alpha} = Q - P \cos \alpha \tan \beta - R \sin \alpha \tan \beta + \frac{1}{mV_T\cos \beta}\Big\{W(\sin \Theta \sin \alpha + \cos \Theta \cos \phi \cos \alpha)$$
$$- T \sin(\alpha + \xi_o) - L\Big\}$$

$$\dot{\beta} = P \sin \alpha - R \cos \alpha + \frac{1}{mV_T}\Big\{W(\cos \Theta \sin \phi \cos \beta + \sin \Theta \cos \alpha \sin \beta - \cos \Theta \cos \phi \sin \alpha \sin \beta)$$
$$- T \sin \beta \cos(\alpha + \xi_o) + Y_A \cos \beta + D \sin \beta\Big\}$$

$$\dot{V}_T = \frac{1}{m}\Big\{T \cos \beta \cos(\alpha + \xi_o) + W[\cos \Theta \cos \phi \sin \alpha \cos \beta - \sin \Theta \cos \alpha \cos \beta + \cos \Theta \sin \phi \sin \beta]$$
$$+ Y_A \sin \beta - D \cos \beta\Big\}$$

$$\dot{P} = (C_1 R + C_2 P)Q + C_3 \mathcal{L} + C_4 N$$

$$\dot{Q} = C_5 RP + C_6(R^2 - P^2) + C_7 M$$

$$\dot{R} = (C_8 P + C_9 R)Q + C_4 \mathcal{L} + C_{10} N$$

$$\dot{\Psi} = (R \cos \phi + Q \sin \phi)/\cos \Theta$$

$$\dot{\Theta} = Q \cos \phi - R \sin \phi$$

$$\dot{\phi} = P + \dot{\Psi} \sin \Theta$$

$$G = 1/(I_x I_z - I_{xz}^2)$$

$$C_1 = G\{(I_y - I_z)I_z - I_{xz}^2\}$$

$$C_2 = G\{I_x - I_y + I_z\}I_{xz}$$

$$C_3 = G I_z$$

$$C_4 = G I_{xz}$$

$$C_5 = (I_z - I_x)/I_y$$

$$C_6 = I_{xz}/I_y$$

$$C_7 = 1./I_y$$

$$C_8 = G\{(I_x - I_y)I_x + I_{xz}^2\}$$

$$C_9 = G\{I_y - I_z - I_x\}I_{xz}$$

$$C_{10} = G I_x$$

Figure 1. Equation Summary

TABLE 2. SURVEY OF TRANSFER FUNCTIONS WITH CHANGE IN β

	α	β	A	$1/T_s(\zeta_{SR})$	$1/T_R(\omega_{SR})$	ζ_d	ω_d	ζ_p	ω_p	ζ_{sp}	ω_{sp}	
												$1/T_q$
Δ	18.84	0	1.0	.096	.425	.333	.847	.167	.165	.186	1.91	0
	18.84	6	1.0	(.653)	(.310)	.371	.860	.139	.175	.185	2.07	-.082
	19.3	15	1.0	(-.459)	(.299)	.871	.62	.326	.199	.161	2.53	-.06
								$1/T_{\theta_1}$	$1/T_{\theta_2}$			$1/T_p$
$N^q_{\delta_e}$	18.84	0	-2.92	.096	.425	.333	.847	-.013	.326	.186	1.91	-.038
	18.84	6	-2.92	(.383)	(.205)	.278	1.38	-.393	.949	.189	1.89	-.033
	19.3	15	-2.80	(.411)	(.206)	.231	2.04	-.690	.991	.196	1.79	-.023
$N^\theta_{\delta_e}$	18.84	0	-2.92	.096	.425	.333	.847	-.013	.326			—
	18.84	6	-2.92	(.49)	(.192)	.267	1.37	-.449	.926			—
	19.3	15	-2.80	(.545)	(.192)	.215	2.03	-.719	.982			—
						ζ_φ	ω_φ					$1/T_p$
$N^p_{\delta_a}$	18.84	0	.430			.288	.525	.167	.165	.186	1.91	-.038
	18.84	6	.431			.386	.384	.146	.167	.189	1.89	-.033
	19.3	15	.381			.544	.305	-.004	.172	.196	1.79	-.023
$N^\varphi_{\delta_a}$	18.84	0	.440			.268	.538	.167	.166	.186	1.91	—
	18.84	6	.441			.375	.386	.148	.166	.186	1.91	—
	19.3	15	.391			.572	.304	.016	.163	.183	1.87	—
						ζ_r	ω_r					$1/T_r$
$sN^\psi_{\delta_a}$	18.84	0	.032			.407	.984	.167	.166	.186	1.91	.449
	18.84	6	.032			.424	.457	.140	.166	.196	2.5	.586
	19.3	15	.031			.525	.258	-.064	.143	.162	3.7	.58
						ζ_r	ω_r					$1/T_r$
$N^r_{\delta_r}$	18.84	0	-.996			.320	.763	.167	.166	.186	1.91	.439
	18.84	6	-.998			.228	1.16	.171	.166	.185	1.95	.398
	19.3	15	-.942			.234	.78	.203	.171	.167	2.32	.417
						$1/T_{r_1}$	$1/T_{r_2}$					
$N^\varphi_{\delta_r}$	18.84	0	1.06			+1.32	-1.67	.167	.166	.186	1.91	—
	18.84	6	1.06			+1.99	-2.40	.168	.165	.188	1.91	—
	19.3	15	1.04			+1.6	-1.95	.182	.165	.193	1.86	—

On the other hand, it may be noted from the lateral-directional numerator factors that sideslip has little effect on the zeros of the lateral or longitudinal degrees of freedom. However, there is a significant difference for the pitch rate and pitch attitude to elevator numerators. These show $1/T_{\theta_1}$ to be small but negative (non-minimum phase) at zero sideslip and to rapidly move to much larger negative values as sideslip increases. At the same time $1/T_{\theta_2}$, which is initially positive, moves to much larger positive values with increasing sideslip. In fact, the movement of $1/T_{\theta_1}$ and $1/T_{\theta_2}$ are precisely the opposite to that of the denominator roots $1/T_S$ and $1/T_R$. The pitch numerator roots move away from each other as sideslip is increased whereas the denominator roots move towards each other and coalesce into the lateral-phugoid mode. The large negative value of $1/T_{\theta_1}$ indicates a potential instability upon closure of either the pitch-rate- or pitch-attitude-to-elevator loops. This is of considerable concern since we would assume the pitch attitude loop would be tightly closed by the pilot at high angle of attack. Furthermore, this would seem to indicate a longitudinal departure mode instead of a lateral departure mode. Attention was therefore turned to the matrix formulation to identify key off-diagonal, or coupling, terms which might be influencing these shifts in numerator and denominator roots.

2. Identification of Key Parameters

Figure 2 presents the nine by nine matrix (three body axis moments, three flight path forces, and three Euler angle transformation equations) for coupled, non-symmetric flight obtained from the partial derivative expansion of the Fig. 1 equations. Only off-diagonal terms which analysis determined to have a significant effect on the transfer function are identified. For the A-7, the major coupling is provided by the terms within the heavy borderlines. Two of these, $\mathcal{L}'_\alpha$ and N'_α, are aerodynamic and two, $\beta_0 \cos \alpha_0$ and $\beta_0 \sin \alpha_0$, are nonlinear kinematic terms.* [The coupling derivative M_β is

---

*The earliest known discussion of this coupling phenomena was documented in 1916 (Ref. 15) for a six-degree-of-freedom analysis of the B.E.-2 biplane in which the octals were factored by hand! This aircraft exhibited $\mathcal{L}_\alpha \doteq \mathcal{L}_\beta$; $N_\alpha = 2N_\beta$; and $M_\beta \doteq M_u$. The conclusion:

"It would be difficult to build a machine in other respects satisfactory which would remain completely stable under very rapid side-slipping. A small change either in increase or decrease of rudder area would be liable to cause either a spiral dive or an

essentially zero for the A-7 as computed from the available data.] Also shown in each matrix element is the magnitude of the term evaluated at $\alpha_o = 18.8$ deg and $\beta_o = 6$ deg.

Note in the Z equation that the effective derivative $Z_p \equiv \beta_o \cos \alpha_o$ is roughly one-third the value of Z_w while $Z_r \equiv \beta_o \sin \alpha_o$ is about one-tenth of Z_w. Thus, one might expect these coupling terms to alter the pitch numerator zero $1/T_{\theta_2}$ since for the uncoupled case $1/T_{\theta_2} \doteq -Z_w$. In the roll equation, $\mathcal{L}_\alpha'$ is about three-quarters the magnitude of $\mathcal{L}_\beta'$ and of opposite sign; thus, for this trim condition (positive β), an increase in α results in a moment which tends to cancel the roll static stability. In the yaw equation N_α' is about eight times the magnitude of N_β' and of the same sign. Both N_α' and N_β' are negative and would indicate a strong directional divergence characteristic with increasing α or β.

The effect of the off-diagonal terms on pitch attitude transfer function pole-zero locations is demonstrated in Fig. 3. Figure 3a shows a completely uncoupled six-degree-of-freedom case, for reference, in which the two lateral-directional modes (ω_d and ω_{SR}) have cancelling pole-zero dipoles as would be expected. The longitudinal poles and zeros reflect the near stall condition in which $1/T_{\theta_2}$ becomes small and negative $1/T_{\theta_1}$ might be expected. Figure 3d presents the pole-zero locations for the completely coupled six-degree-of-freedom case which shows the poles to be little affected by coupling, whereas a major shift occurs in zero locations. The most significant movement is in the two real zeros because, as will be shown later, closure of the $\theta \rightarrow \delta_e$ loop will drive one closed-loop root toward the right half plane (RHP) zero and system instability. Of secondary concern is the separation of the dutch

(continued from preceding page)

> instability of spin, necessarily followed by a nose dive either with or without previous stalling, in order to obtain the necessary speed to overcome the instability. The large decrease in the damping factor of the phugoid oscillation would tend to accelerate this performance."

A similar development to the above but employing a five-degree-of-freedom model is presented in Ref. 16 for a swept-wing transport aircraft. The same coupling terms were found to dominate at much lower angle of attack but comparable sideslip range (e.g., 6 to 15 deg). In the Ref. 16 study, the coupling primarily produced an oscillatory aerodynamics/kinematic interchange in short-period energy between p and α via L_α.

Figure 2. Matrix for Coupled Equations with $\beta \neq 0$
[Data for $\alpha_0 = 18.8°$, $\beta_0 = 6°$]
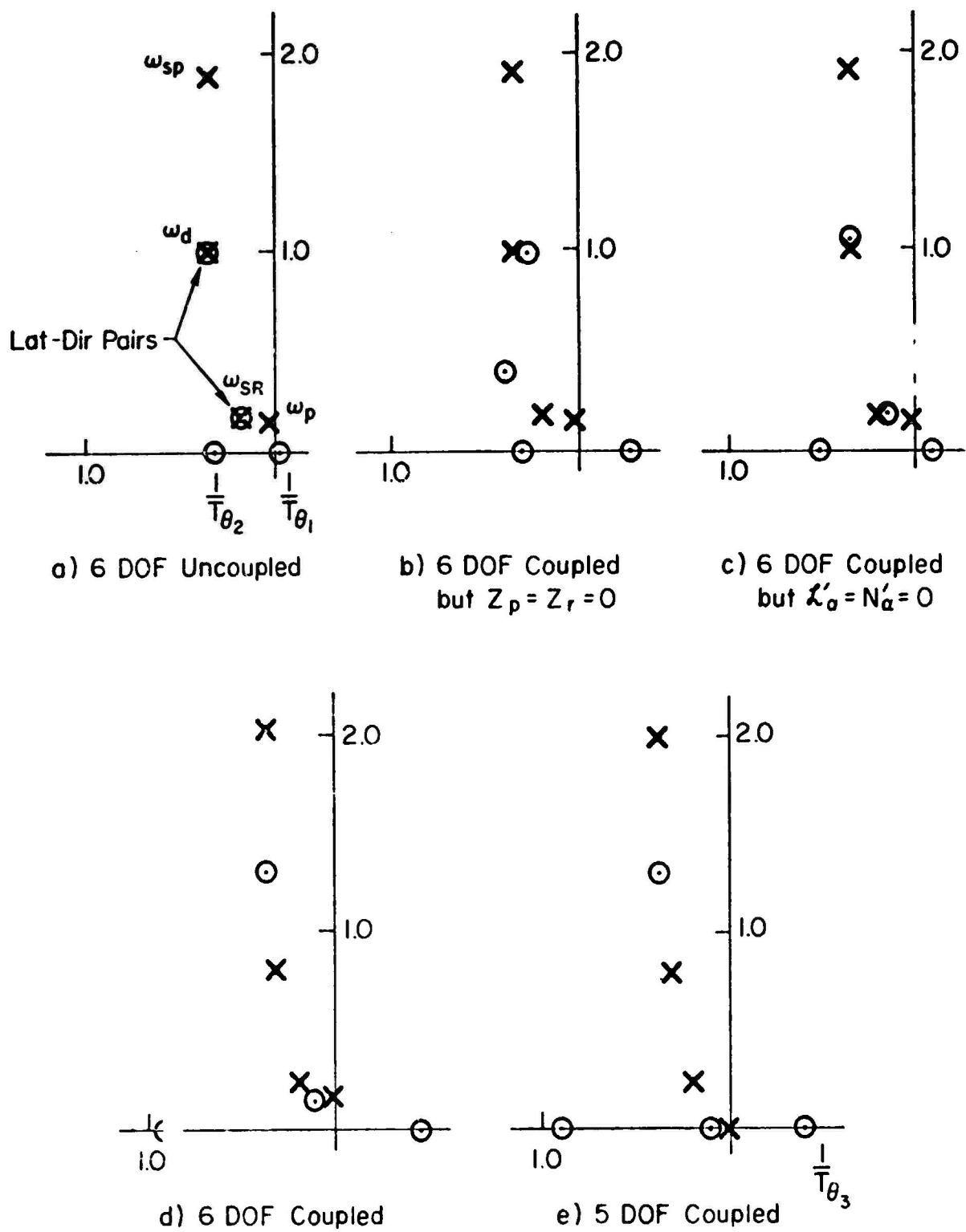
Figure 3. Survey of $N'_{\delta_e}\Delta$ Approximations for $\alpha_0 = 13.8°$, $\Gamma_0 = 1°$

roll dipole pair which indicates considerable modal response excitation via elevator (i.e., longitudinal to lateral coupling).

The influence of the individual pair of coupling terms is identified in Figs. 3b and 3c. In Fig. 3b the Z equation off-diagonal terms are set to zero; in Fig. 3c the L and N equation off-diagonal terms are removed. Both result in similar influences on the various zeros and indicate these "effective" derivatives must occur in combined or multiplicative form in the transfer function numerator.

As an aid in identification of the modes reflected by the poles and zeros of Fig. 3, the longitudinal dynamics were reduced to a short-period approximation by deletion of the X equation, which usually eliminates the $1/T_{\theta_1}$ zero and replaces the complex phugoid pole with a first-order pole at the origin. However, Fig. 3e shows the zeros previously identified as $1/T_{\theta_1}$ and $1/T_{\theta_2}$ to remain unchanged from the complete six-degree-of-freedom case. The complex zero previously identified as ω_{SR} has become a first-order zero near the origin. The phugoid mode is transformed into a first-order pole at the origin as expected. Because the pole-zero configuration of Fig. 3e reflects coupled lateral-longitudinal modes (compare with Fig. 3d), the real zero in the right half plane previously labeled $1/T_{\theta_1}$ will be identified as $1/T_{\theta_3}$ in subsequent analysis since this is a new, coupled lateral-longitudinal mode.

In a further attempt to identify the pitch attitude zeros, the matrix for the five-degree-of-freedom pitch attitude numerator was expanded in literal terms and the polynomial coefficients obtained. Approximations containing only the most significant terms are presented in Eq. 1.

$$N_{\delta_e}^{\theta} = M_{\delta_e}[As^5 + Bs^4 + Cs^3 + Ds^2 + Es + F] \tag{1}$$

where (coupling terms are underlined):

$$A = 1$$

$$B \doteq Z_w' + \mathcal{L}_p' + (N_r' + Y_v)$$

$$C \doteq \mathcal{L}_p'(Z_w + N_r') - \mathcal{L}_\beta' \sin \alpha - \underline{\mathcal{L}_\alpha' Z_p}$$

$$D \doteq -\mathcal{L}_\beta'[(g/U_o) \cos \theta - (Z_w + N_r') \sin \alpha] - N_\beta'(Z_w + \mathcal{L}_p') \cos \alpha$$

$$E \doteq \mathcal{L}_\beta'(g/U_o) \cos \theta[(Z_w + N_r') - (Z_{\delta_e}/M_{\delta_e})M_w] + \underline{Z_p(\mathcal{L}_\beta' N_\alpha' - N_\beta' \mathcal{L}_\alpha')}$$

$$F \doteq -\mathcal{L}_\beta'(g/U_o) \cos \theta N_r' Z_w$$

It may be observed that the off-diagonal coupling terms are multiplicative and primarily influence the C and E coefficients. An attempt was made to factor this equation into literal expressions for the roots. However, this task proved too time consuming and was abandoned.

a. Single-Loop Control

A single-loop system-survey for elevator control of pitch attitude with the six-degree-of-freedom coupled airframe in non-symmetrical flight is shown in Fig. 4. The transfer function is shown in the upper left.[*] The root locus in the top right of the figure reflects root migrations for a pure gain closure. Note that the roots starting at ω_{SR} rapidly move to the real axis and then split into two real roots; one of which moves towards $1/T_{\theta_2}$, the other moves towards $1/T_{\theta_3}$. The rapidity of the movement of these closed-loop poles towards the zeros is demonstrated by a Bode-siggy plot in the bottom half of Fig. 4. The heavy solid and dashed lines of the Bode correspond to the path of the closed-loop roots along the real (σ) axis in the root locus above. As the loop gain is increased, the complex poles emanating from ω_{SR} meet the real axis at the apex of the solid curve in the Bode-siggy plot. Further increase in gain moves one closed-loop root to a lower frequency or towards the origin while the other root moves to higher frequency and, at very high gain, asymptotically approaches the $1/T_{\theta_2}$ zero at 0.866 rad/sec. The root that goes toward the origin passes into the right half plane as shown in the root locus. This is represented in the Bode-siggy by the dashed line which reflects the mirror image of the closed-loop pole asymptotically approaching the $1/T_{\theta_3}$ zero at −0.3 rad. If the pilot is to achieve effective control of pitch attitude, he must close the loop so the gain line lies below the low-frequency asymptote of the Bode plot. It is obvious that this then results in a closed-loop pole in the right half plane. If the pilot closes the loop so that unity gain "crossover" is achieved in the region of 1-3 rad/sec, which covers the range of usual "loose" to "tight" piloted pitch attitude control, it may be seen that the closed-loop poles will lie very close to the open-loop zeros. For example, a unity dc gain provides a crossover between 1.5 and 2.5 rad/sec and

---

[*]Throughout this report a shorthand notation is used in presenting transfer functions: $(s + a) \equiv (a)$; $[s^2 + 2\zeta\omega s + \omega^2] \equiv [\zeta, \omega]$.
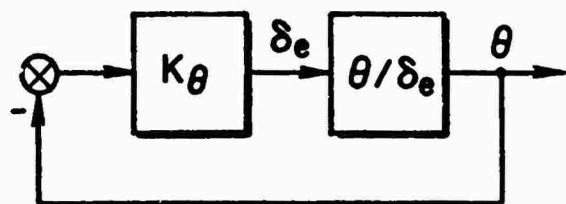
$$\frac{\theta}{\delta_e} = \frac{-2.9(.3)(.866)[.28,.185][.27,1.4]}{[.163,.167][.71,.29][.36,.88][.185,2.1]}$$
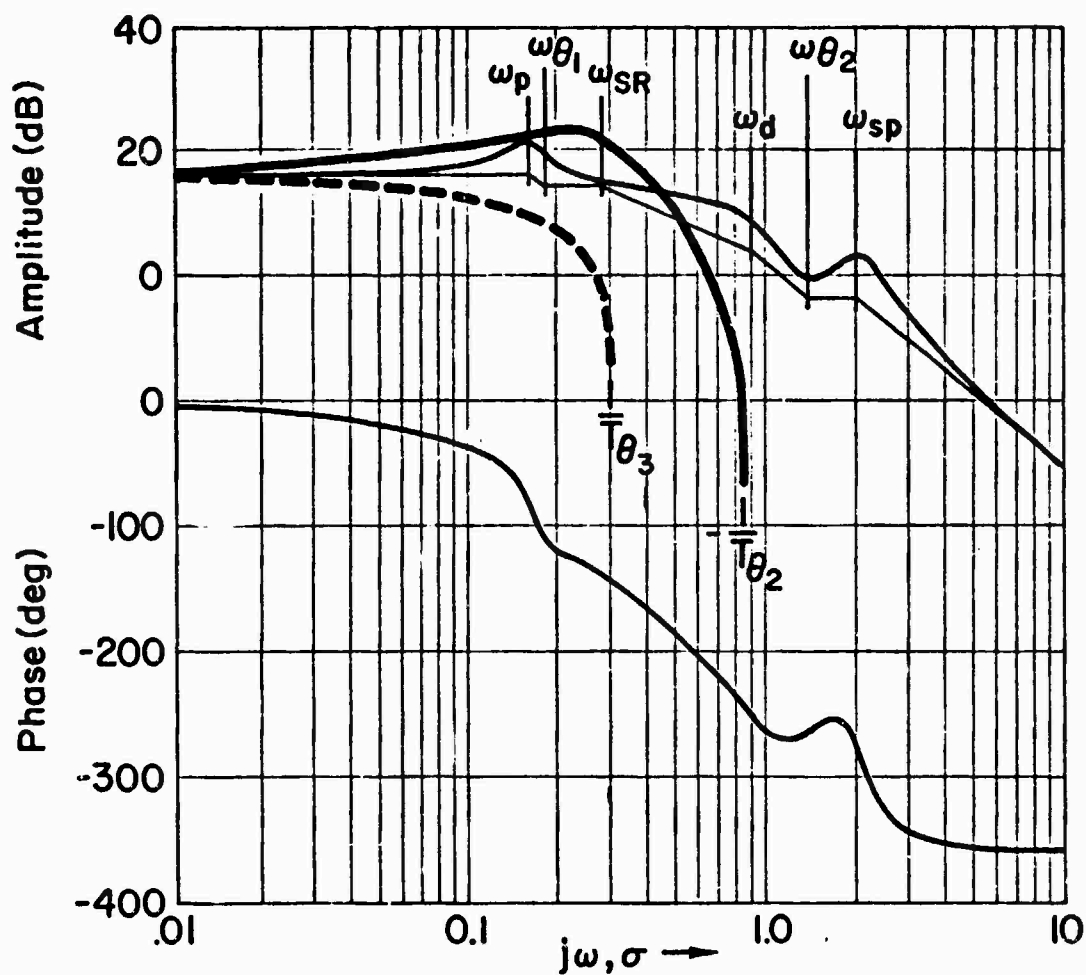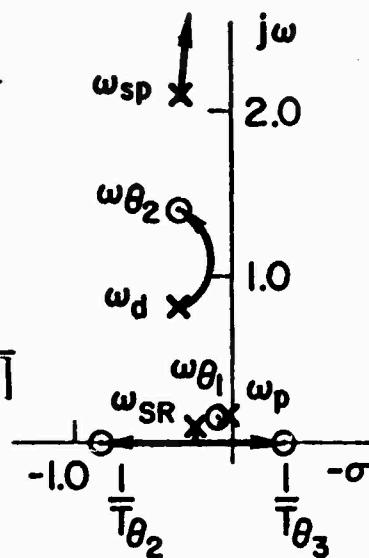
Figure 4. Pitch Attitude Closure Survey, $\alpha_0 = 18.8^\circ$, $\beta_0 = 6^\circ$

closed-loop roots at −0.28 and +0.66 rad/sec. The resulting first-order divergence has a time constant of about 3.6 sec.

The difference in open- and closed-loop responses may be observed from time traces of the six-degree-of-freedom digital simulation using nonlinear aerodynamic lookup tables. Figure 5 shows the open-loop lateral and longitudinal time traces for the A-7 trimmed at an initial 17.3 deg α and 0 deg β and a ramp δ_e input of 1.2 deg/sec. An aileron doublet is also introduced at 4 sec to provide some excitation of the lateral modes. The traces indicate that a slow directional divergence starts at approximately 8 sec and 24 deg α. It then couples with p (and α) to form a divergent oscillation with a period of approximately 11 sec. This will be shown in subsequent sections to be an unstable lateral-phugoid mode. If the aircraft were trimmed at a small initial β the open-loop response would remain nearly the same but the divergence would develop at a slightly lower α because of the combined effect of β and α on the lateral phugoid as noted previously.

Figure 6 shows the system response when the pitch attitude loop is closed with unity gain (as in Fig. 4) and a step θ_c of 0.01 rad is introduced. The aircraft is initially trimmed for steady flight at α = 18.8 deg, β = 6 deg, and φ = 5 deg. The predicted first-order divergence is seen to start immediately and to dominate the r, ψ, p, θ, and α traces. The divergence time constant is approximately 3.6 sec, as measured in the r, p, θ, and α traces, consistent with the closed-loop right half plane root location predicted in Fig. 4. By the time 24 deg α is reached the aircraft is well departed. These responses verify the closed-loop mode to be coupled longitudinal-lateral motion. They also appear to match the description of the classic A-7 nose slice departure described in Ref. 17 as an initial high yaw rate followed by a high roll rate. The traces of Fig. 6 show that at 9 sec, which is just before the high roll rate (departure) develops:

$$r \doteq -15 \text{ deg/sec (extrapolated)}$$

$$p \doteq -4.9 \text{ deg/sec}$$

$$\beta \doteq +13.5 \text{ deg}$$
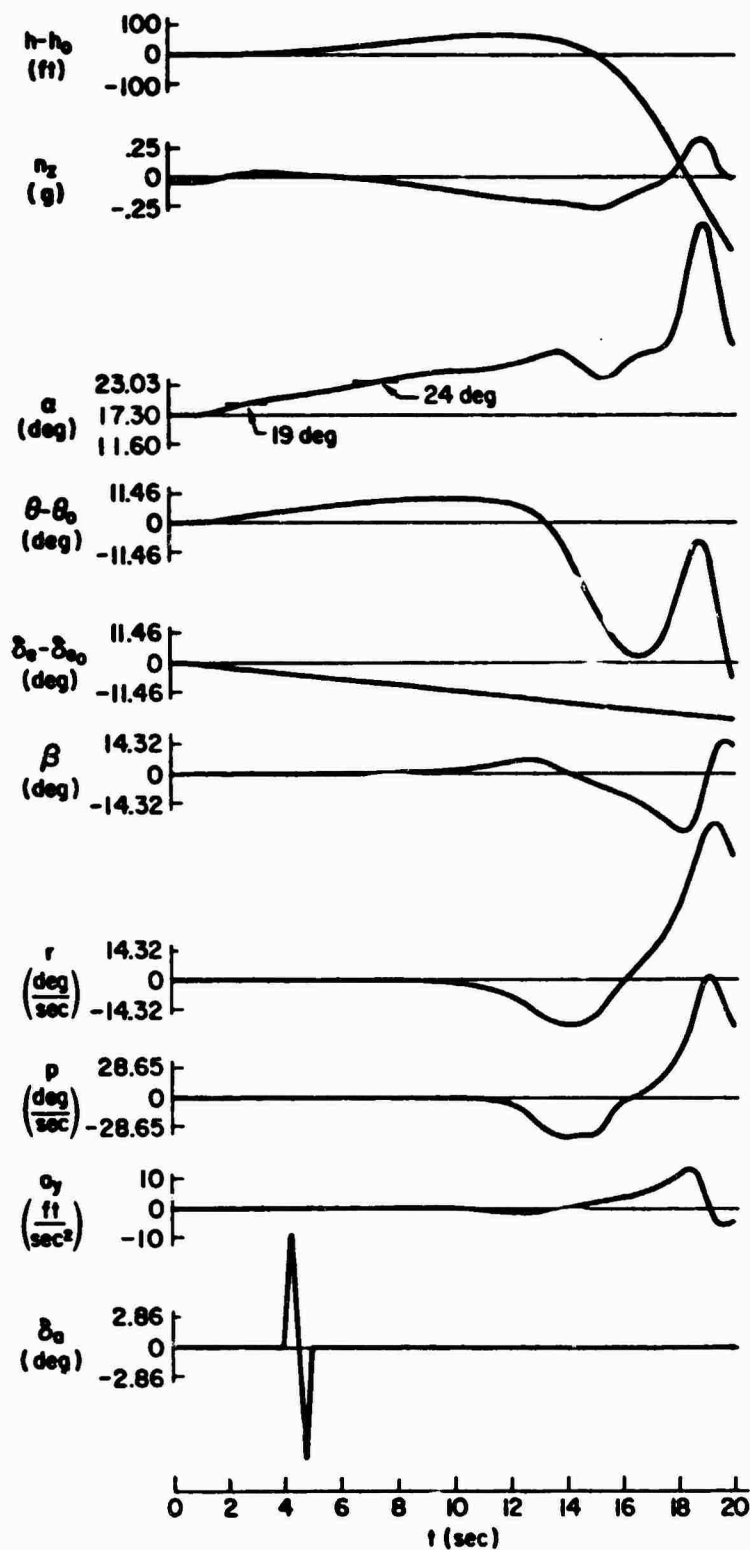
Figure 5. Open-Loop Six-Degrees-of-Freedom Digital
Simulation Response to Ramp δ_e
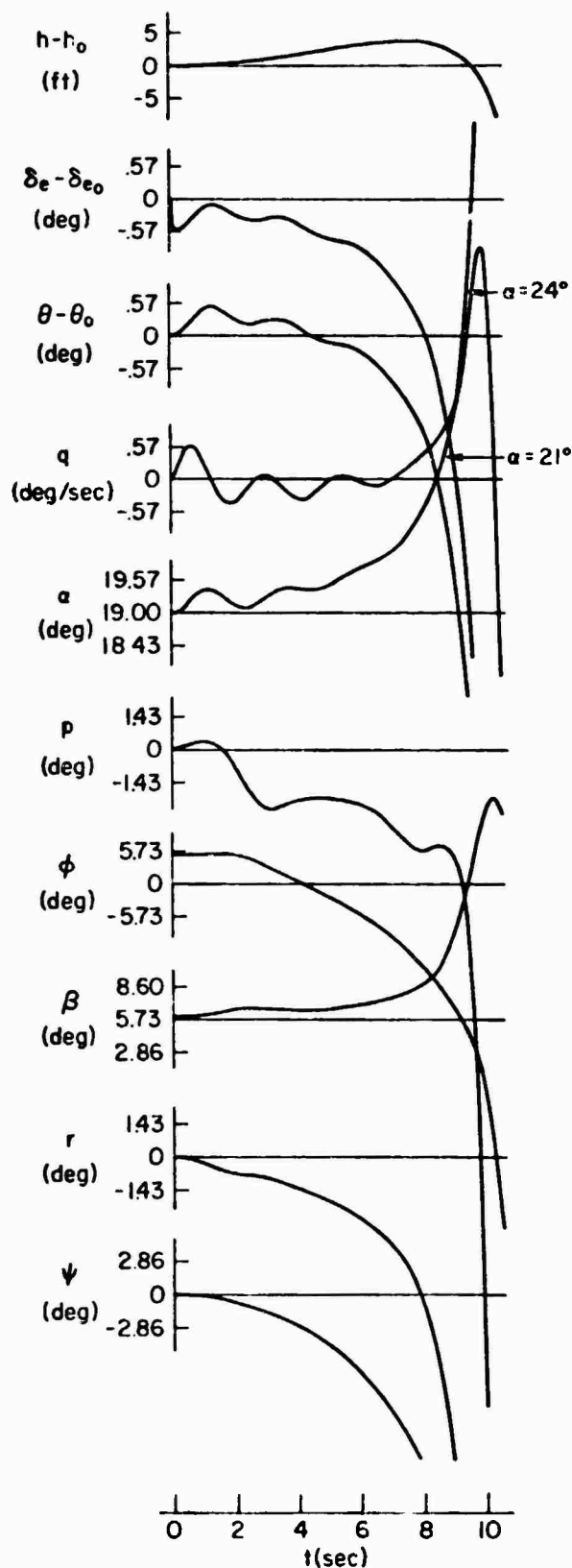
Figure 6. Closed-Loop Digital Simulation Response to Step h_c; $\alpha_0 = 19.8°$, $t_0 = 5°$

They also show that the initial longitudinal command excites considerable roll rate. It will be shown later that both the longitudinal short period and the lateral dutch roll contain considerable roll rate response. These two modes then result in the "beat frequency" shape of the roll rate time trace.

b. Multiloop Control

Lateral control is used very sparingly at high angles of attack because it tends to aggravate directional departure. Nevertheless, it is pertinent to assume that a pilot would tend to close a simple (pure gain) bank-angle-to-aileron loop, shown in Fig. 7, under the lateral-directional departure
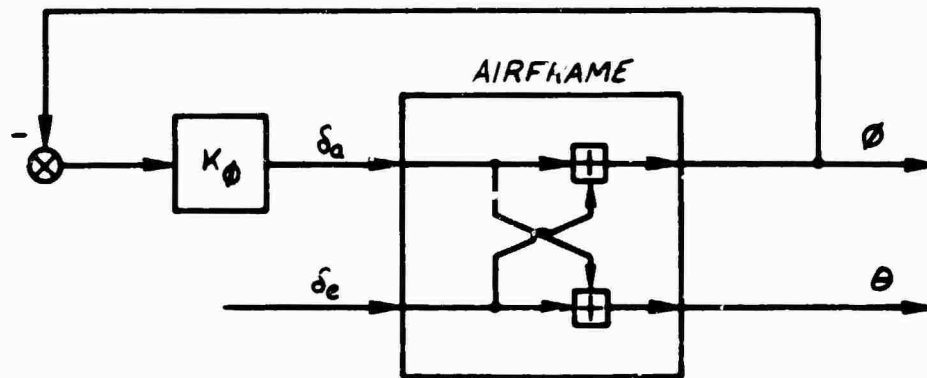
Figure 7. Closed-Loop Roll Coupling into Pitch

circumstances indicated in Fig. 6. The use of a second control surface input (e.g., roll control via aileron) with the coupled airframe dynamics modifies the effective pitch attitude numerator, $N_{\delta_e}^{\theta}$, as shown in Eq. 2.

$$N_{\delta_e}^{\theta}\bigg|_{\varphi \leftarrow \delta_a} = N_{\delta_e}^{\theta} + K_{\varphi}N_{\delta_a\delta_e}^{\varphi \theta} = N_{\delta_e}^{\theta'}$$

$$= -2.9(-.3)(.86)[.28,.18][.27,1.4] \qquad (2)$$

$$+ K_{\varphi}\{-1.3(-.046)(.29)[.3,.6]\}$$

That is, the effective $\theta \leftarrow \delta_e$ numerator is the sum of the basic open-loop pitch numerator, $N_{\delta_e}^{\theta}$, and a coupling numerator, $N_{\delta_a\delta_e}^{\varphi \theta}$, term "weighted" by

the roll loop gain, K_φ. The roots of each term are shown in Eq. 2 evaluated at $\alpha = 18.8$ deg and $\beta = 6$ deg. If K_φ is small (i.e., $\varphi \rightarrow \delta_a$ essentially open loop), then the roots of $N_{\delta_e}^{\theta'}$ are essentially the same as those of $N_{\delta_e}^{\theta}$. However, if K_φ is very large then the coupling term dominates and, within the frequency range of interest, the roots of $N_{\delta_e}^{\theta'}$ will be those of $N_{\delta_a \delta_e}^{\varphi \theta}$. For intermediate values of K_φ the root locations may be defined in terms of the root locus $1 + (K_\varphi N_{\delta_a \delta_e}^{\varphi \theta} / N_{\delta_e}^{\theta})$, which is sketched in Fig. 8. Note that
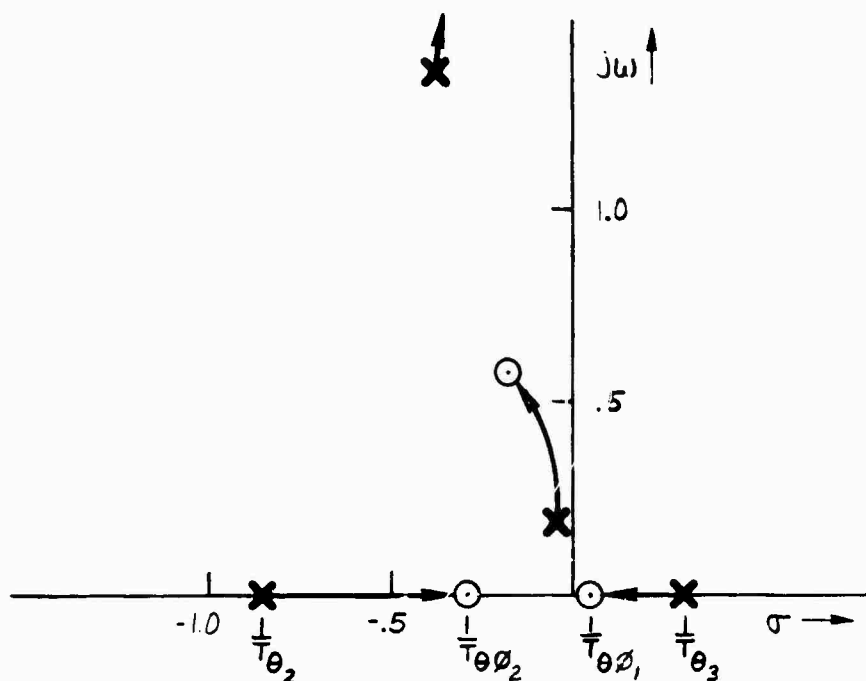
Figure 8. $N_{\delta_e}^{\theta'}$ Root Migration with Increasing K_φ

both the numerator and denominator have roots in the right half plane. Therefore, $1/T_{\theta z}'$ (the root emanating from $1/T_{\theta 3}$) is driven toward and eventually into $1/T_{\theta \varphi_1}$, the coupling numerator term as K_φ increases. Thus, closure of the $\varphi \rightarrow \delta_a$ loop decreases the potential divergence rate caused by the $\theta \rightarrow \delta_e$ closure but is not able to completely stabilize the motion because a zero of $N_{\delta_e}^{\theta'}$ always remains in the right half plane. In fact, the first-order divergence will lead to eventual saturation of aileron control (if used) as the divergence progresses.

It is important to recognize that in an analogous manner to Fig. 7 closure of the $\theta \to \delta_e$ loop will modify the $\varphi \to \delta_a$ numerator as shown in Eq. 3.

$$N_{\delta_a}^{\varphi}\bigg|_{\theta \to \delta_e} = N_{\delta_a}^{\varphi} + K_\theta N_{\delta_a \delta_e}^{\varphi \ \theta} = N_{\delta_a}^{\varphi'}$$

$$= .44[.15, .16][.35, .41][.19, 1.9] \tag{3}$$

$$+ K_\theta\{-1.3(-.046)(.29)[.3, .6]\}$$

Note that both Eqs. 3 and 2 have the same coupling numerator. Therefore, tight closure of the $\theta \to \delta_e$ loop will result in the effective numerator $N_{\delta_a}^{\varphi'}$ having a right half plane zero. Tight closure of both $\varphi \to \delta_a$ and $\theta \to \delta_e$ will result in identical effective numerators having right-half-plane zeros in both loops and, since the closed-loop poles are driven into the zeros, the same divergence in each loop.

The sensitivity of the right-half-plane zeros $1/T_{\theta_3}$ and $1/T_{\theta\varphi_1}$ to change in trim sideslip, angle of attack, or bank angle is shown in Table 3. It can be observed that increasing angle of attack or sideslip (or both) rapidly moves both zeros further into the right half plane, and divergence time constants of two seconds or less would be expected.

TABLE 3

EXAMPLE VARIATION OF RIGHT-HALF-PLANE ZEROS
DUE TO PITCH-ROLL COUPLING

α_o	β_o	φ_o	$1/T_{\theta_3}$	$1/T_{\theta\varphi_1}$
18.8	6	5.14	−0.3	−0.05
18.8	6	0	−0.45	−0.15
20.9	6	5.5	−0.442	−0.445
19.3	15	0	−0.72	−0.31

If the pilot were to use rudder instead of aileron to oppose the lateral divergence, the results would be similar to those above, because the coupling numerators $N_{\delta_e \delta_r}^{\theta \; p}$ and $sN_{\delta_e \delta_r}^{\theta \; \psi}$ also have a right-half-plane root:

$$N_{\delta_e \delta_r}^{\theta \; \varphi} = -3(-.016)(.33)(2.03)(-2.47) \tag{4}$$

$$sN_{\delta_e \delta_r}^{\theta \; \psi} = 3.1(\; .014)[.99 , .35][.23 , 1.23] \tag{5}$$

Thus, use of rudder along with elevator will not stop the divergence and will result in saturation of the rudder control as well.

c. Model Validation

It was previously indicated (Fig. 3) that a 5 DOF model of the pitch transfer function exhibit the same key pole-zero values as does the 6 DOF model. Figure 9 shows time traces of a departure obtained with a nonlinear 5 DOF analog simulation of the A-7. As in Fig. 3, the X equation, or speed degree of freedom, has been eliminated. The same trim conditions prevail as for the 6 DOF time traces of Fig. 6: $\alpha_o = 18.8$ deg, $\beta_o = 6$ deg, level flight, pitch attitude loop closed with unity dc gain, and a 0.01 rad θ_c introduced to disturb the trim. The dashed lines on the α, p, and β traces indicate the response obtained from the nonlinear 6 DOF digital model. The 6 DOF and 5 DOF time traces are identical for yaw rate. The dotted curves in Fig. 9 are time responses for α, p, β, and r obtained from an actual nose slice departure* in an A-7 aircraft (Ref. 17) but with the flight trace shifted in time to achieve an effective overlay of p traces. The close agreement between the three sets of time traces is considered to be a validation of both the five- and six-degree-of-freedom models.

In Fig. 10 the $\varphi \rightarrow \delta_a$ loop has been closed along with $\theta \rightarrow \delta_e$. This results in somewhat closer agreement between flight and the 5 DOF analog model α and p traces. However, the sideslip is not in quite as close agreement as it is in Fig. 9. It was subsequently learned (Ref. 18) that the flight traces reflect use of rudder, not aileron, to oppose the nose slice. The rudder was

---

*W = 22,699 lb x_{cg} = 29.6 % MAC

h = 14,400 ft Φ_o = 75 deg

Figure 9. Time History Comparison of Departure

26
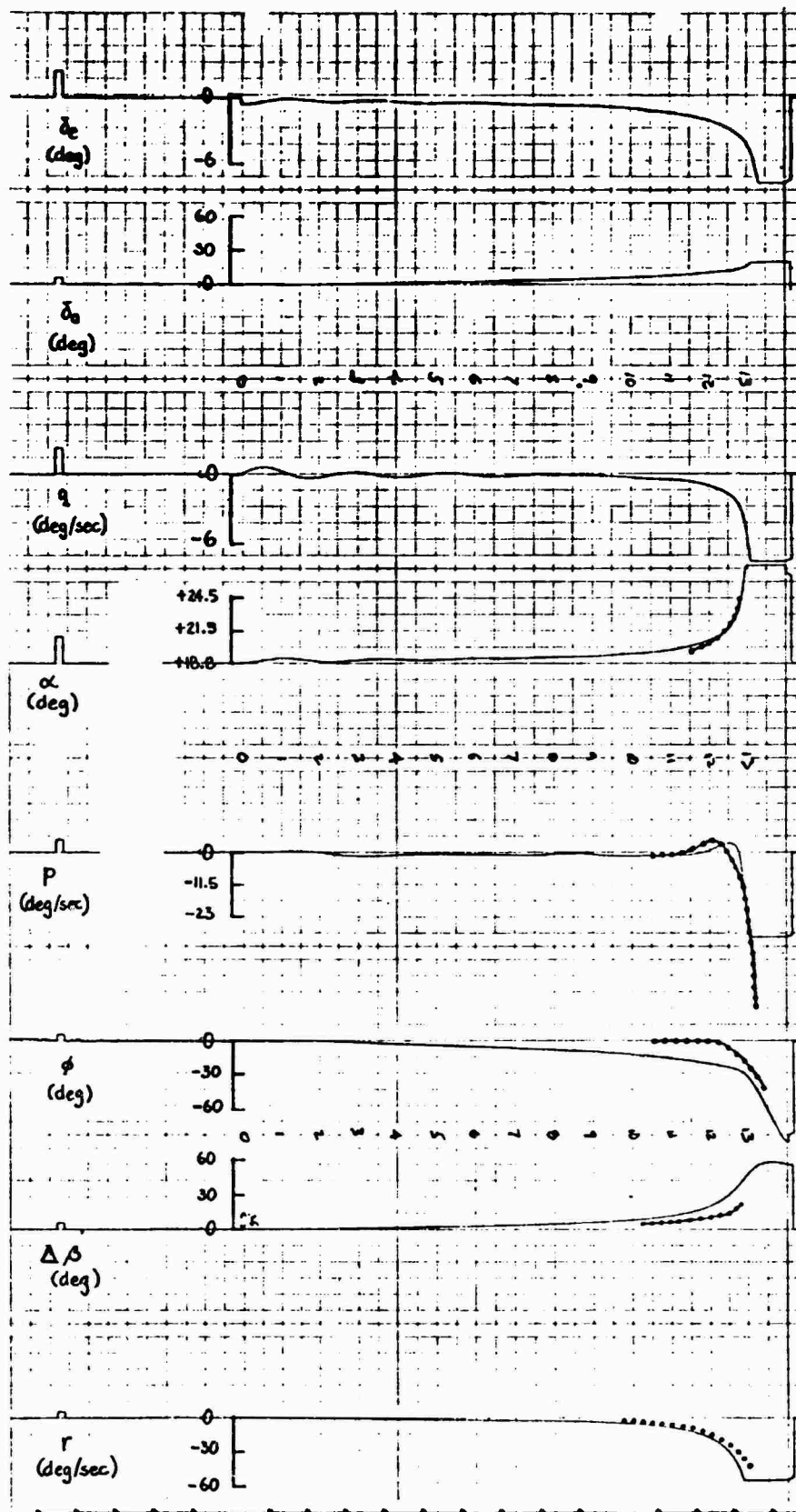
$\alpha'_0 = 18.8$ deg

$\beta_0 = 6$ deg

$K_\theta = -1$; $K_\phi = 5$

$\theta - \delta_e$, $\phi - \delta_a$

Closed-loop response
to 0.01 rad θ_c

— 5 DOF Analog

---- Flight

Figure 10. Departure Time Traces with Both Pitch and Roll Loops Closed

ineffective in preventing the departure, and showed a first-order divergence to full deflection similar to that shown for the aileron trace in Fig. 10. This is consistent with the previous coupling numerator analysis. Also, comparing the time traces of Fig. 9 and 10, closure of the bank-angle-to-aileron loop reduces the departure rate, but does not prevent departure; verifying the analytic prediction.

Several additional points emerge from an examination of Fig. 10 as follows. The roll rate remains relatively small until approximately 12.5 sec beyond which it builds very rapidly for both the five-degree-of-freedom model and for the actual aircraft. The yaw rate traces match pretty well, but the computed sideslip is approximately twice that for the actual aircraft. Angle of attack for both flight and computed traces match very well. Thus, based on either computed or actual time histories, the aircraft motion initially is a yawing, sideslipping response which rapidly builds to large values before an appreciable roll rate develops (as described in Ref. 17).

Relative to stall and post-stall recovery, Refs. 17 and 18 indicate that such is best accomplished by neutralizing the cockpit controls or, preferably, "letting go" of the stick. This opens the loop and returns the aircraft roots to the stable open-loop pole positions, as shown in Fig. 4; the aircraft then should recover by itself.

On the basis of the foregoing, it is concluded that the right-half-plane zero of the $N^{\theta}_{\delta_e}$ numerator is the key parameter in the A-7 nose slice departure. The relatively close agreement among analysis, simulation traces, actual flight traces, and recovery procedures recommended by LTV is considered to validate our model.

3. Source of $\mathcal{L}'_\alpha$, N'_α

Preceding analysis has shown that the zero $1/T_{\theta_3}$ is strongly influenced by the stability derivatives $\mathcal{L}'_\alpha$ and N'_α. These are generated in the 9×9 matrix of Fig. 2 as the partial derivatives of $\dot{p}$ with respect to α and of $\dot{r}$ with respect to α, as shown in Table 4. These partials are expanded in both literal and numerical terms in Table 4. In both cases the first term in the sum of partial derivatives dominates: $\mathcal{L}'_\alpha$ from the partial of roll moment with respect to α but at a trim δ_e and β; N'_α from the partial of the yaw moment with respect to α

TABLE 4. PARTIAL DERIVATIVE EXPANSION FOR $\mathcal{L}'_\alpha$ AND N'_α

$$\mathcal{L}'_\alpha = \frac{\partial \dot{p}}{\partial \alpha} = \frac{\bar{q}\,Sb}{I_x I_z - I_{xz}^2}\left(I_z \frac{\partial C_\ell}{\partial \alpha} + I_{xz}\frac{\partial C_n}{\partial \alpha}\right)$$

$$N'_\alpha = \frac{\partial \dot{r}}{\partial \alpha} = \frac{\bar{q}\,Sb}{I_x I_z - I_{xz}^2}\left(I_{xz}\frac{\partial C_\ell}{\partial \alpha} + I_x \frac{\partial C_n}{\partial \alpha}\right)$$

$$\frac{\partial C_\ell}{\partial \alpha} = \frac{\partial C_\ell(\delta_e,\alpha,\beta)}{\partial \alpha} + \frac{\partial C_\ell(\alpha,\delta_{a_R})}{\partial \alpha} - \frac{\partial C_\ell(\alpha,\delta_{a_L})}{\partial \alpha} + \text{sgn}\,\delta_a \frac{\ell C_\ell(\alpha,\delta_a)}{\partial \alpha} + \delta_r \times \frac{\partial C_{\ell\delta_r}}{\partial \alpha}$$

$$+ \frac{b}{2V}\left[\frac{\partial C_{\ell p}(\alpha)}{\partial \alpha} \times p_o + \frac{\partial C_{\ell r}(\alpha)}{\partial \alpha} \times r_o\right]$$

$$= 0.092826 - 0.004011 - 0.002865 - 0.003037 + 0.002132 + 0.000248 + 0.0001782$$

$$\frac{\partial C_n}{\partial \alpha} = \frac{\partial C_n(\delta_e,\alpha,\beta)}{\partial \alpha} + \frac{\partial C_n(\alpha,\delta_{a_R})}{\partial \alpha} - \frac{\partial C_n(\alpha,\delta_{a_L})}{\partial \alpha} + \text{sgn}\,\delta_a \frac{\partial C_n(\alpha,\delta_a)}{\partial \alpha} + \delta_r \times \frac{\partial C_{n\delta_r}}{\partial r}$$

$$+ \frac{b}{2}\left[\frac{\partial C_{np}(\alpha)}{\partial \alpha} \times p_o + \frac{\partial C_{nr}(\alpha)}{\partial \alpha} \times r_o\right]$$

$$= -0.147994 - 0.0021945 - 0.013723 - 0.001662 + 0.000820 + 0.0001752 - 0.0002495$$

but at a trim δ_e and β. Plots of these coefficients are presented in Figs. 11 and 12. Figure 11 shows C_{ℓ_α} is positive over the region 15-22 deg α. At approximately 22-23 deg α the slope is zero, and for higher angles of attack the slope reverses. The slope also increases as trim sideslip increases. Figure 12 shows a decided break in C_{n_α} at approximately 13 deg α and large negative slope to approximately 30 deg where the slope becomes zero. For larger α this coefficient becomes positive. Thus, in the region between 13 and 24 deg α, there is a large yawing moment with change in angle of attack.

Referring back to the time traces of Figs. 9 or 10 and the matrix of Fig. 2, a strong correlation between the aircraft motions and the slopes C_{ℓ_α} and C_{n_α} can be detected. For example, Fig. 2 indicates that at roughly 19 deg α and 6 deg β, $\mathcal{L}'_\alpha$ and $\mathcal{L}'_\beta$ are of opposite sign and of nearly the same magnitude. Thus, with β and α increasing positively we would expect the resulting rolling moments contributions to nearly cancel. This is reflected in both Figs. 9 and 10 as a relatively low roll rate up to an angle of attack of approximately 21-22 deg. Above this, C_{ℓ_α} changes sign, $\mathcal{L}'_\alpha$ and $\mathcal{L}'_\beta$ then augment one another and, on the time traces, roll acceleration suddenly becomes very large. The large negative value of N'_α results in a large negative $\dot{r}$ and positive β as α is increased. Again, this is reflected in the time traces of Figs. 9 and 10. Thus, the departure characteristics of the A-7 appear closely related to the C_{n_α} and C_{ℓ_α} characteristics between 15 and 24 deg α in Figs. 11 and 12. Similar conclusions are reported in Ref. 19 regarding the effect of C_{n_α} and C_{ℓ_α} at $\beta \neq 0$ (e.g., Fig. 13) influencing the spin entry and recovery characteristics of one version of the F-100.

Results of wind tunnel tests conducted by LTV are reported in Ref. 18. Of particular interest are tuft studies showing airflow over the wing, aft fuse-lage, and vertical tail at 16-19 deg α and 0-16 deg β. Figure 14 (from Ref. 18) depicts tuft activity over the wings at 17 deg α and various sideslip angles. At 17 deg α and zero β, an area of steady flow exists over a portion of the center section of each wing. As β increases the area of separation moves rapidly inboard on the leading and outboard on the trailing wing center sections. The larger area of separated flow on the leading wing does not mean that surface will stall first, since tufts are not necessarily reliable
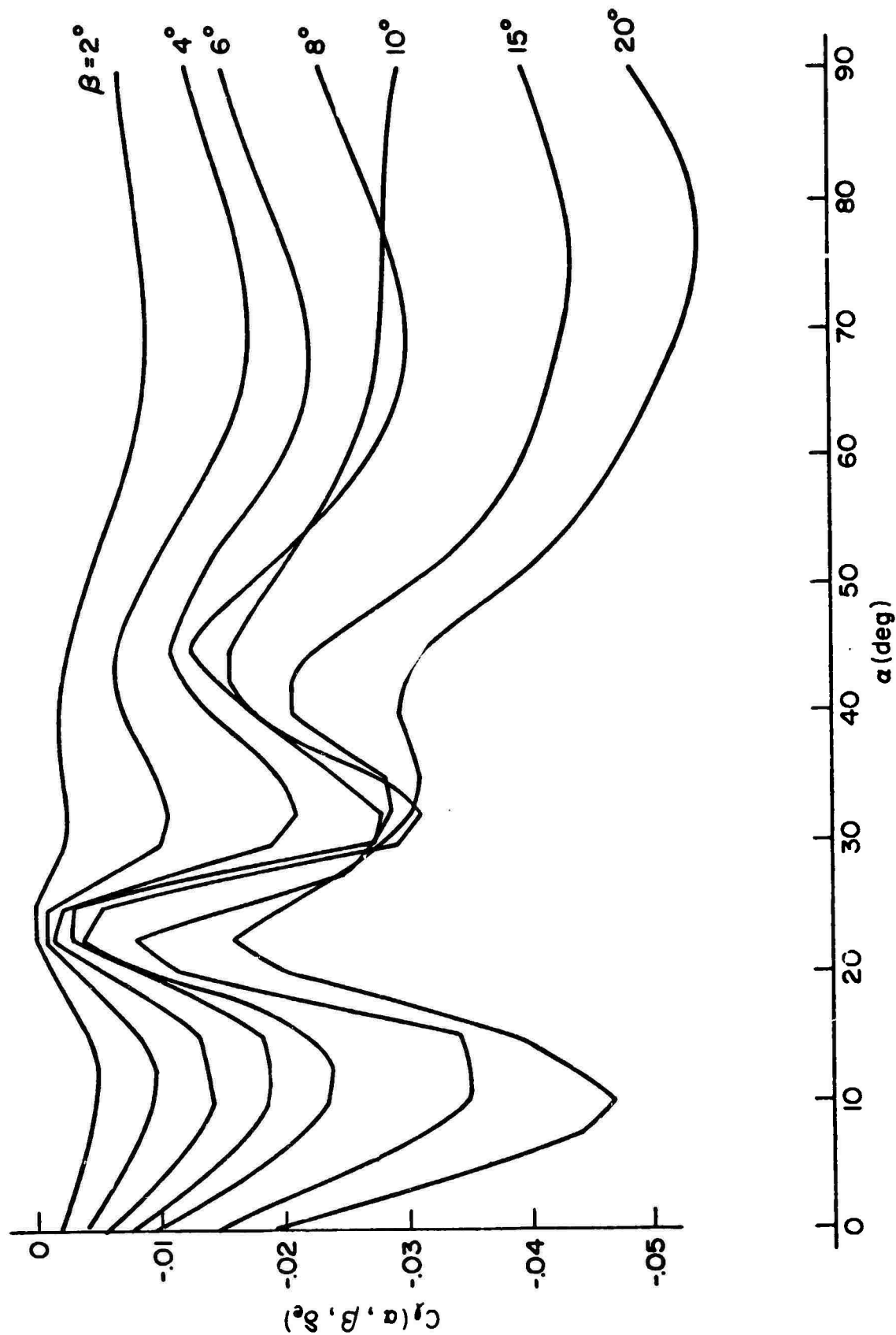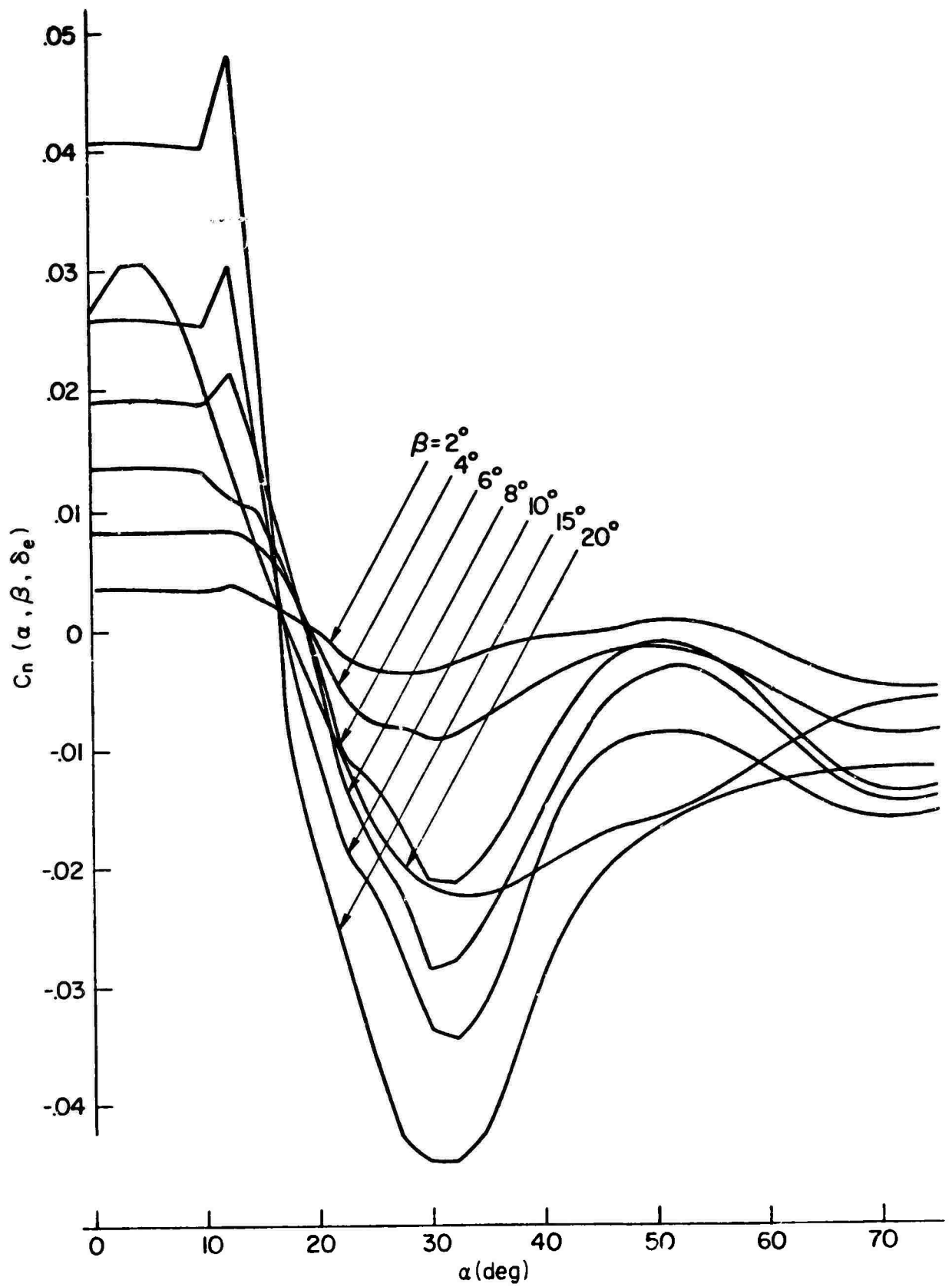
30

Figure 11. $C_l(\alpha, \beta, \delta_e)$ vs. α at $\delta_e = -15^o$ and $0^o < \beta < 20^o$

31

Figure 12. $C_n(\alpha, \beta, \delta_e)$ vs. α at $\delta_e = -15$ deg and $0 < \beta < 20$ deg

32
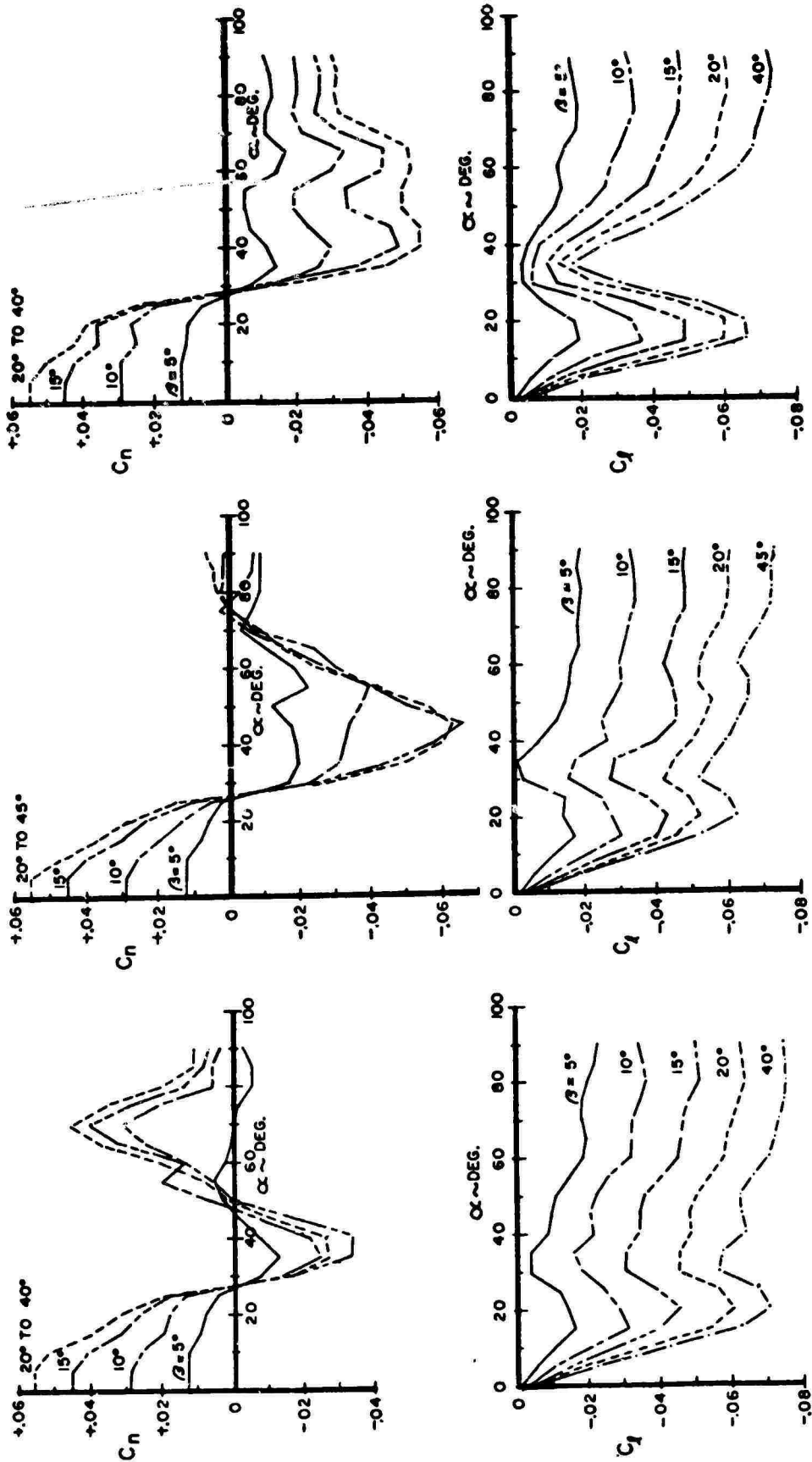
Figure 13. F-100F Static Moment Coefficients Used in IBM Calculations (from Ref. 19)

33
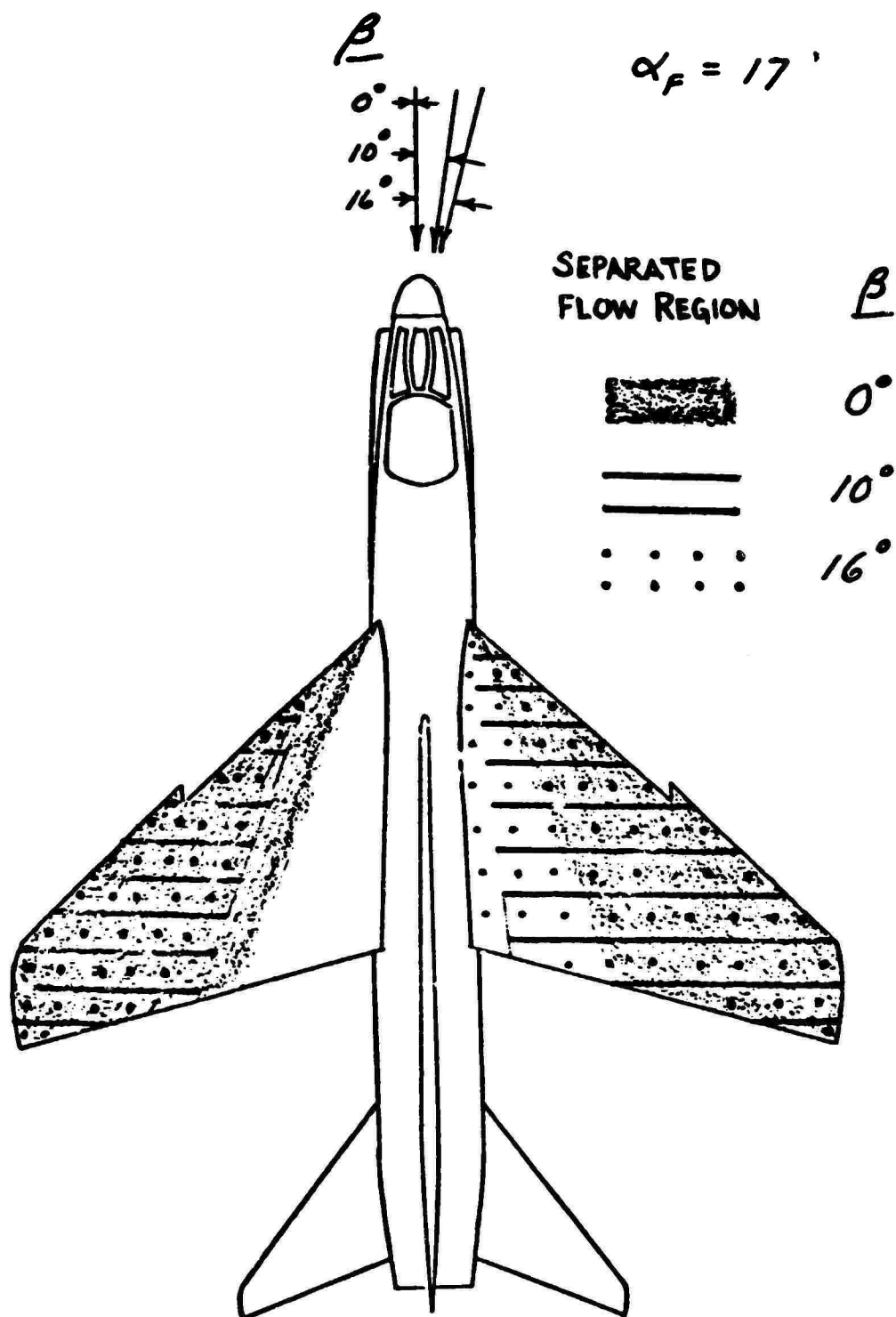
Figure 14. A-7 Wing Tuft Activity; Basic Airplane (from Ref. 18)

indicators of the level of lifting performance. However, there is strong
evidence that separated flow develops on the wing center section coincident
with the α's and β's which show a marked reduction in airplane directional
stability. Figure 15 (also from Ref. 18), for 19 deg α and 6 deg β, shows
a disturbance of the tufts near the tip and on the downwind or lee-side of
the fin. The orientation of the tufts on the fuselage (not shown in Fig. 15)
and on the vertical tail indicate the disturbance is due to a vortex system
which originates at the intersection of the wing and fuselage. It would
appear that if sideslip were increased to greater than 6 deg this vortex
would clear the vertical tail and stability would again increase. However,
the LTV studies showed the pattern of wing center section flow separation
with α and β is such that the separation on the upwind panel and the attached
flow on the downwind panel induces a vortex system off the wing surface which
has the same sense of rotation as the wing fuselage vortex just noted. Thus,
the two systems reinforce each other and create a strong vortex which results
in the local flow redirection at the vertical tail leading edge. This flow
orientation would produce destabilizing forces and account for the directional
stability decrease with increasing α and/or β. The LTV tuft studies indicated
that both the leading and trailing wings stalled at between 24 and 25 deg α.
This is quite consistent with the zero slope points on Fig. 11.

Thus, Ref. 18 relates the decrease in directional stability to the vortex
activity from the fuselage and wing center panel impinging on the downwind
side of the vertical fin. It appears that this activity can equally be related
to the inflections in the coefficient plots of Figs. 11 and 12, to the sta-
bility derivatives $\mathcal{L}_\alpha'$ and N_α' and, eventually, to the nose slice parameter, $1/T_{\theta_3}$.

4. Conclusions

The foregoing analysis and simulation has indicated that the nose slice
departure of the A-7 aircraft can occur at α's considerably below the normal
stall. The nose slice is caused by a chain of events which evolve from
directional mistrim or failure to suppress sideslip in maneuvers. This
sideslip results in shed vortices which give rise to aerodynamic moments,
N_α' and $\mathcal{L}_\alpha'$. A nonlinear kinematic coupling also occurs between the sideslip
and yawing or rolling of the aircraft to give rise to pseudo-derivatives, Z_p
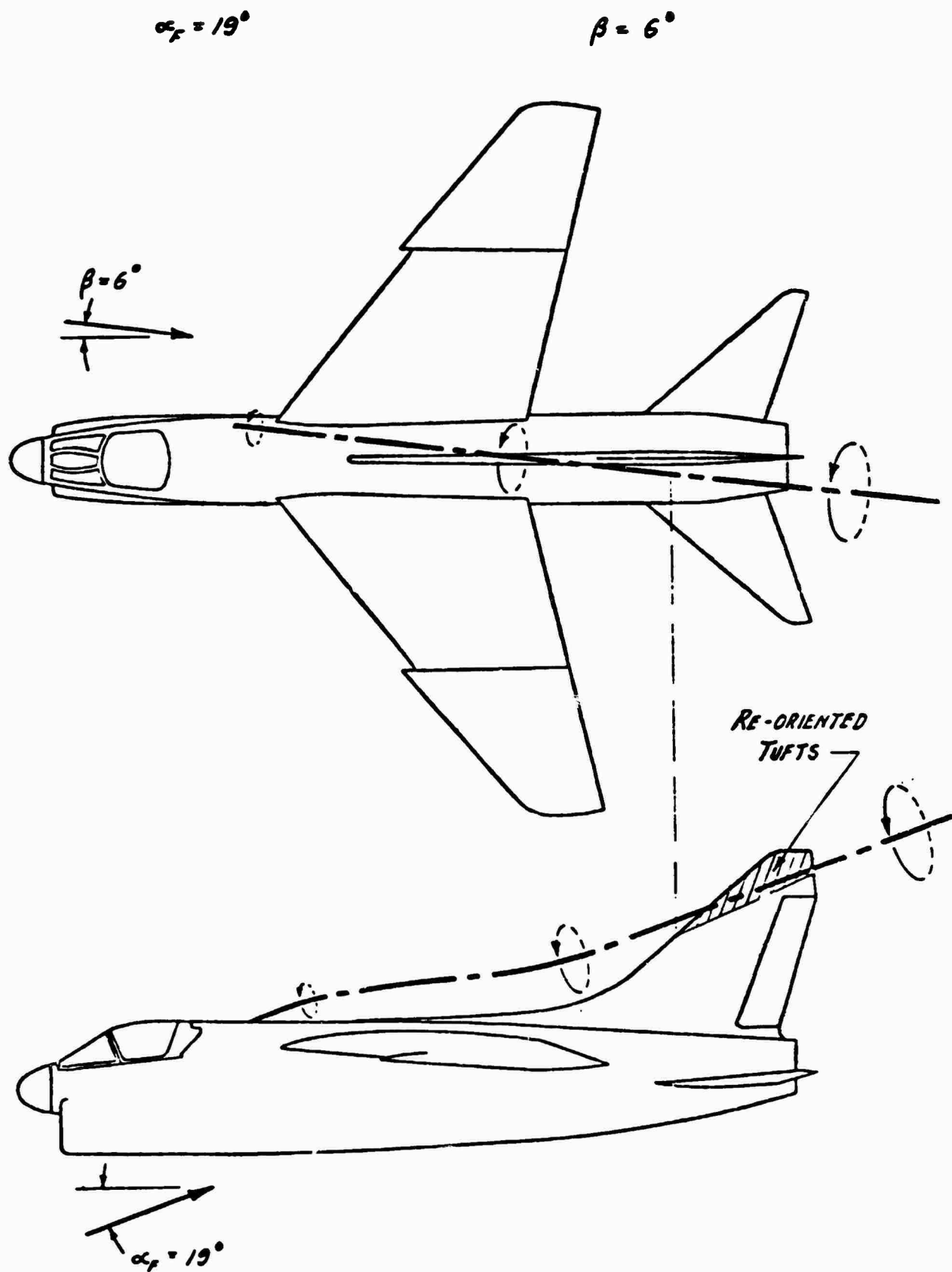
Figure 15. A-7 Wing-Fuselage Vortex Path (from Ref. 18)

and Z_r (see **Fig.** 2). These combined coupling effects result in a right-half-plane zero in the pitch-attitude-to-elevator numerator. Normal pitch attitude control activity then drives the aircraft unstable. The instability starts as a first-order divergence in lateral, directional, and longitudinal modes. Pilot attempts to oppose the motion rapidly lead to saturation of control in all axes. The principal means of recovery is to open the pitch attitude loop, that is, to let go of the stick.

A quasi-linearized five-degree-of-freedom model containing the coupling terms $\mathcal{L}'_\alpha$, N'_α, Z_p, and Z_r only, and with appropriate derivatives changed as a function of angle of attack and sideslip provides very good agreement with actual flight traces. This model can be utilized for the piloted simulations discussed later.

B. WING ROCK

Another common departure, or pre-departure, characteristic is wing rock. This generally is described as a fairly large-angle roll oscillation but there is considerable disagreement as to whether it is an open-loop or closed-loop (i.e., pilot-aggravated) phenomenon. Wing rock is exhibited by several current high-performance aircraft; however, the F-4 has received the most notoriety in this respect. Wing rock reportedly is encountered in the F-4 starting at about 20 deg α and, if α is further increased, this is followed by nose slice at about 25 deg. The underlying open-loop cause has been attributed to nonlinear C_{n_β} (Refs. 3 and 20) and/or the partitioning of the total roll damping coefficients

$$C_{\ell_r} - C_{\ell_{\dot\beta}} \cos \alpha$$

$$C_{\ell_p} - C_{\ell_{\dot\beta}} \sin \alpha$$

into the basic $\dot\beta$, r, and p contributions (Ref. 21). The underlying closed-loop cause is generally attributed to "classical" ω_ϕ/ω_d effects (e.g., Ref. 6).

Several F-4 simulations of varying degrees of complexity and fidelity have been made to exhibit "wing rock"; however, the principal means of achieving it have also varied considerably. For example, Ref. 22 indicates wing rock could only be obtained when all of the following were present simultaneously.

1. With some form of control (pilot or autopilot) to prevent the aircraft from departing before wing rock could develop.

2. By assuming an asymmetrical moment from the stabilator (i.e., an $\mathcal{L}_{\delta e}$ and $N_{\delta e}$).

3. With $\varphi \rightarrow \delta_a$ loop closed.

The asymmetrical moment from the stabilator was required to start a lateral motion. It should be noted that this study did not include an M_β coupling derivative. M_β will be shown later to have a significant magnitude for the F-4. Another approach to achieving closed-loop wing rock has been to significantly reduce the damping derivative L_p.

In an effort to gain better insight and physical understanding of this phenomenon, the tack taken here has been to review the potential causal factors noted previously, to seek new parameters through the same analytic techniques applied to nose slice, and finally, to incorporate the most promising of these causal factors into the A-7 dynamic model to see if wing rock can be induced in this aircraft which has never been reported to have a wing rock.

1. Dynamic Model

Nonlinear aerodynamic data for the F-4 were supplied in the form of digital lookup tables as $f(\alpha, \beta)$ in listings and card decks by Mr. J. R. Chambers of NASA Langley Research Center. The trim configuration selected was based on a flight condition and loading which produced wing rock during the flight tests reported in Ref. 23:

$$h = 14{,}000 \text{ ft} \qquad I_x = 26{,}000$$
$$W = 37{,}200 \text{ lb} \qquad I_y = 166{,}000$$
$$\text{c.g.} = 29.3 \ \bar{c} \qquad I_z = 183{,}500$$
$$\text{Flaps and gear up} \qquad I_{xz} = 5{,}000$$

Open-loop time traces from the nonlinear digital simulation trimmed for level flight at $\alpha = 20$ deg and $\beta = 1$ deg are shown in Fig. 16. A negative rudder
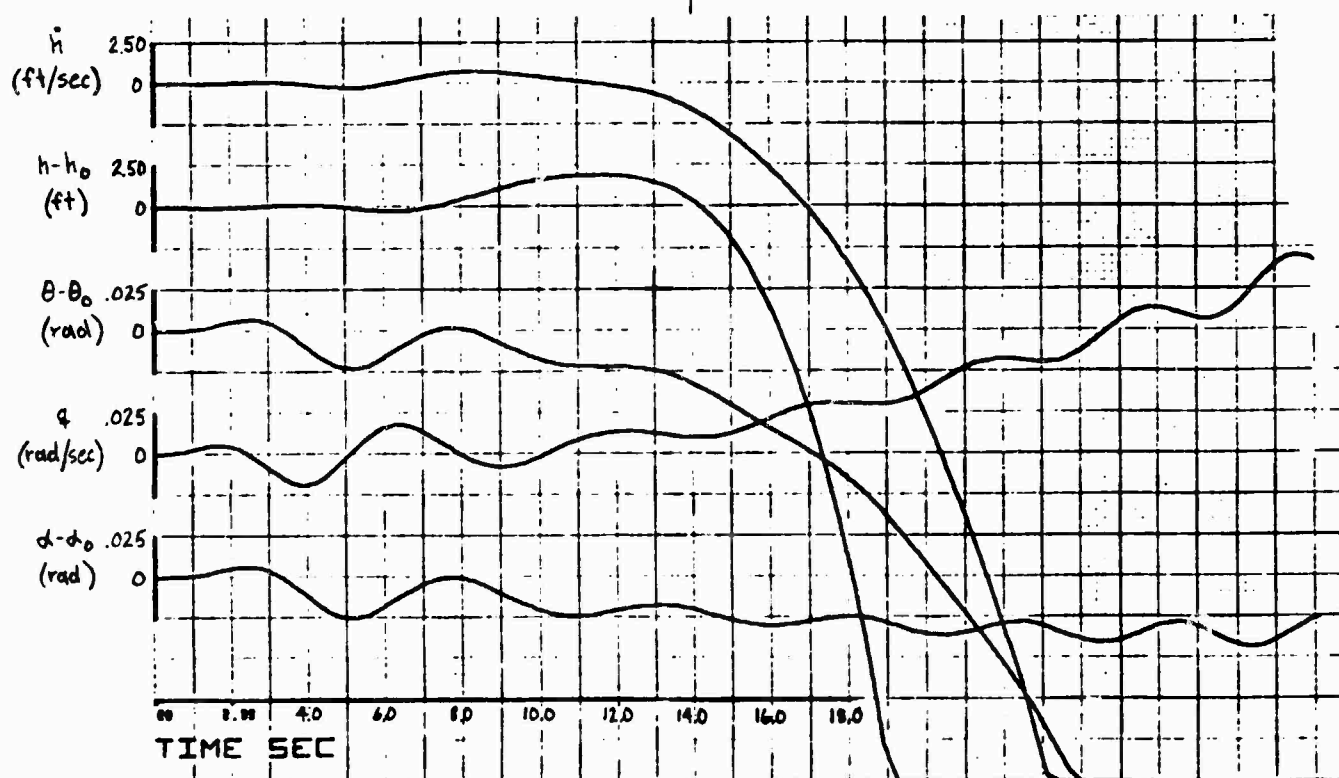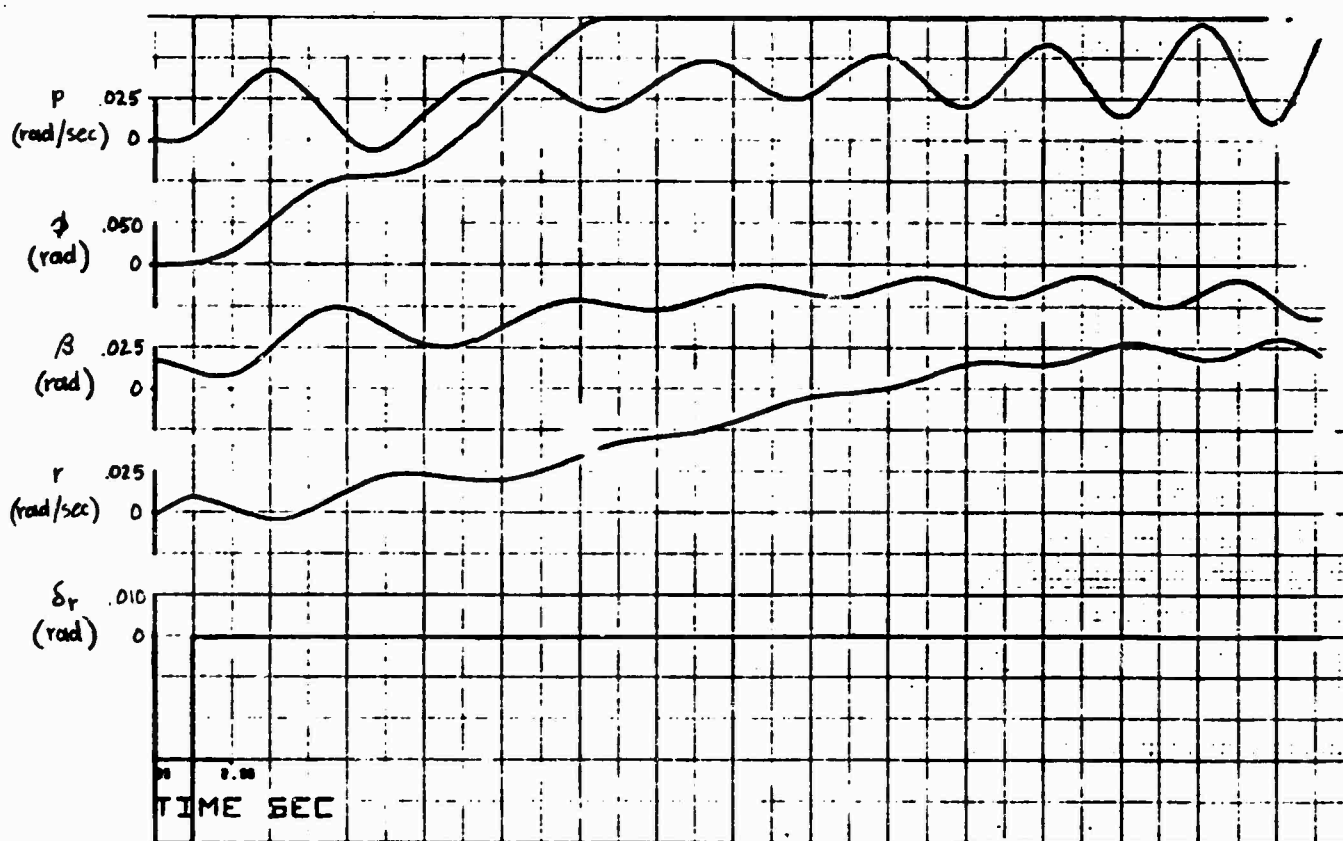
Figure 16. F-l Open-Loop Response to a Rudder Pulse ($\alpha_0 = 20^\circ$, $\beta_0 = 1^\circ$)

pulse was used to excite the unaugmented airframe. Although the traces exhibit an oscillation that is obviously self-sustaining (see p trace) it bears little resemblance to the large amplitude roll usually seen in flight traces and therefore cannot be considered wing rock per se.

Stability derivatives calculated for three different combinations of trim α and β are presented in Table 5. One case for the A-7 is also shown for comparison. Derivatives reflecting significant differences between the two aircraft are $\mathcal{L}_\beta'$, $\mathcal{L}_r'$, N_β', N_p', and M_β. Of these the most startling are $\mathcal{L}_\beta'$, which has a change in sign and an order-of-magnitude difference, and M_β, which has no counterpart in the A-7 data. Note that N_α' and $\mathcal{L}_\alpha'$ are comparable for similar trim conditions.

A plot of C_m versus β is shown in Fig. 17, where it can be seen than C_{m_β} is negligible for $\beta < \pm 5$ deg and $\alpha < 15$ deg but becomes significant for $\alpha = 17.5$ deg and above. This is precisely the region where wing rock is encountered. A check of the M_β contribution to vehicle dynamics was made by calculating the transfer functions with and without M_β. The results are shown in Fig. 18 for the $\alpha_0 = 20$ deg, $\beta_0 = 1$ deg case. It appears that for this
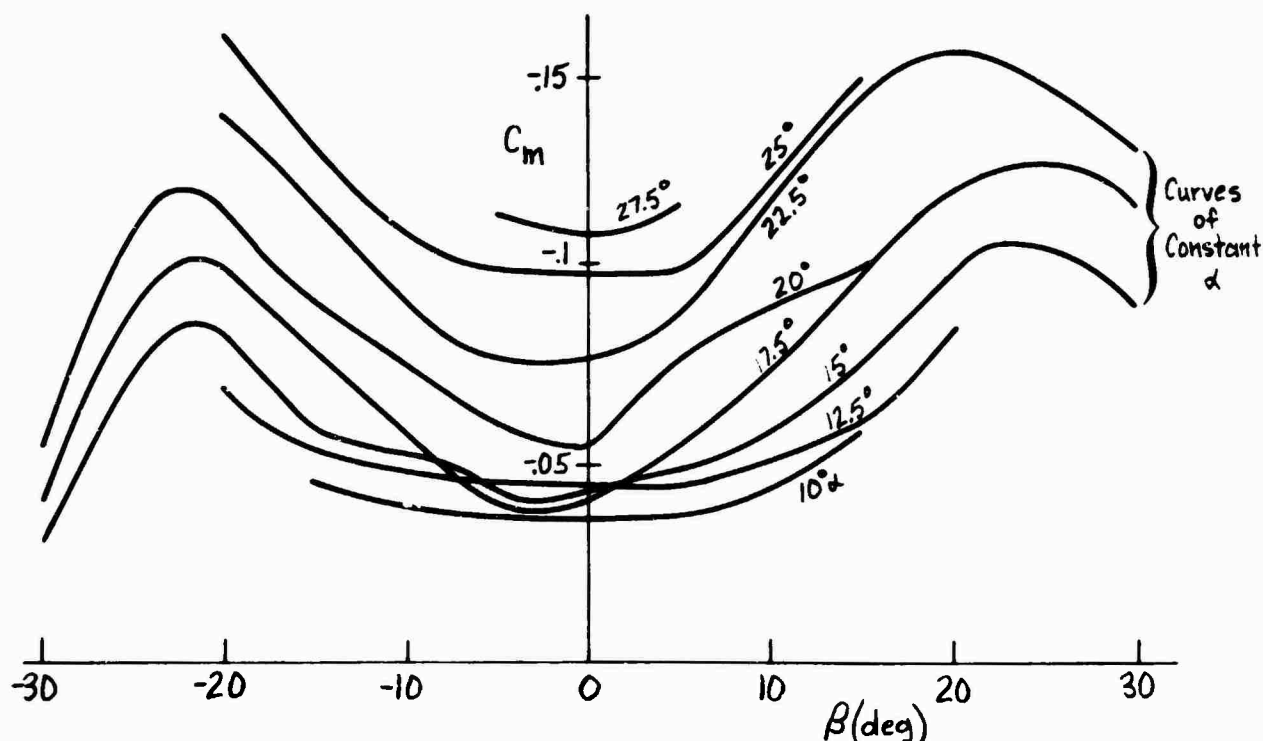
Figure 17. C_m Versus β from F-4 Lookup Tables

TABLE 5. BODY AXIS DIMENSIONAL DERIVATIVES (F-4 AND A-7)

	F-4			A-7
U_o	287.6	293	295	
α_o	22.94	20.84	20	20.9
β_o	0	4	1	6
ϕ_o	0	2.5	0	5.6
Y_v	-.0426	-.0527	-.058	-.094
Y_α	-.0006	-.0281	.0077	.0145
$1-Y_r$	.9182	.9306	.935	.934
Y_p	.3922	.358	.345	.357
Y_{δ_a}	—	-.00077	-.0017	—
Y_{δ_r}	---	.0077	.0069	.0234
Y_{δ_e}	—	.0006	.00013	-.0025
L'_β	.2912	.1613	.191	-2.45
L'_α	-.3307	5.62	3.28	3.75
L'_r	1.737	1.4	1.27	.3338
L'_p	-.688	-.4515	-.36	-.655
L_{δ_a}	-.815	-1.138	-1.34	.373 (in./sec²)
L_{δ_r}	.063	.175	.134	1.4
L_{δ_e}	—	—	—	-.383
N'_β	-.477	.0952	.32	-.6293
N_α	-.00043	-1.62	-.505	-1.55
N'_r	-.2425	-.2252	-.218	-.113
N'_p	-.03385	-.0446	-.0488	.032
N_{δ_a}	.06	.069	.078	.0235 (in./sec²)
N_{δ_r}	-.2462	-.297	-.28	-.88
N_{δ_e}	—	—	—	.134
$M_{\dot{}}$	-.4636	-1.608	-1.63	—
M_α	-2.231	-2.335	-2.83	-3.884
M_q	-.554	-.574	-.592	-.3081
M_u	.00025	.00023	.00022	-.00003
M_{δ_e}	-.557	-1.205	-1.41	-2.72
$Z_{\dot{}}$	-.0131	-.0374	-.0403	—
Z_α	-.1352	-.0865	-.0816	-.23
Z_q	.9396	.9423	.941	1.0
Z_u	-.00051	-.00061	-.00061	-.0009
Z_r	0	-.0249	-.006	-.0375
Z_p	0	-.0553	-.015	-.0982
Z_{δ_e}	-.015	-.028	-.031	-.06
$X_{\dot{}}$	-.5105	-2.10	-2.91	-2.47
X_α	-16.28	-10.11	-14.37	-13.19
X_u	-.08815	-.0807	-.078	-.075
X_{δ_r}	—	.159	.035	.612
X_{δ_e}	-1.408	-2.505	-2.2	-4.76
η_{dyn}	-.552	.030	.236	.284
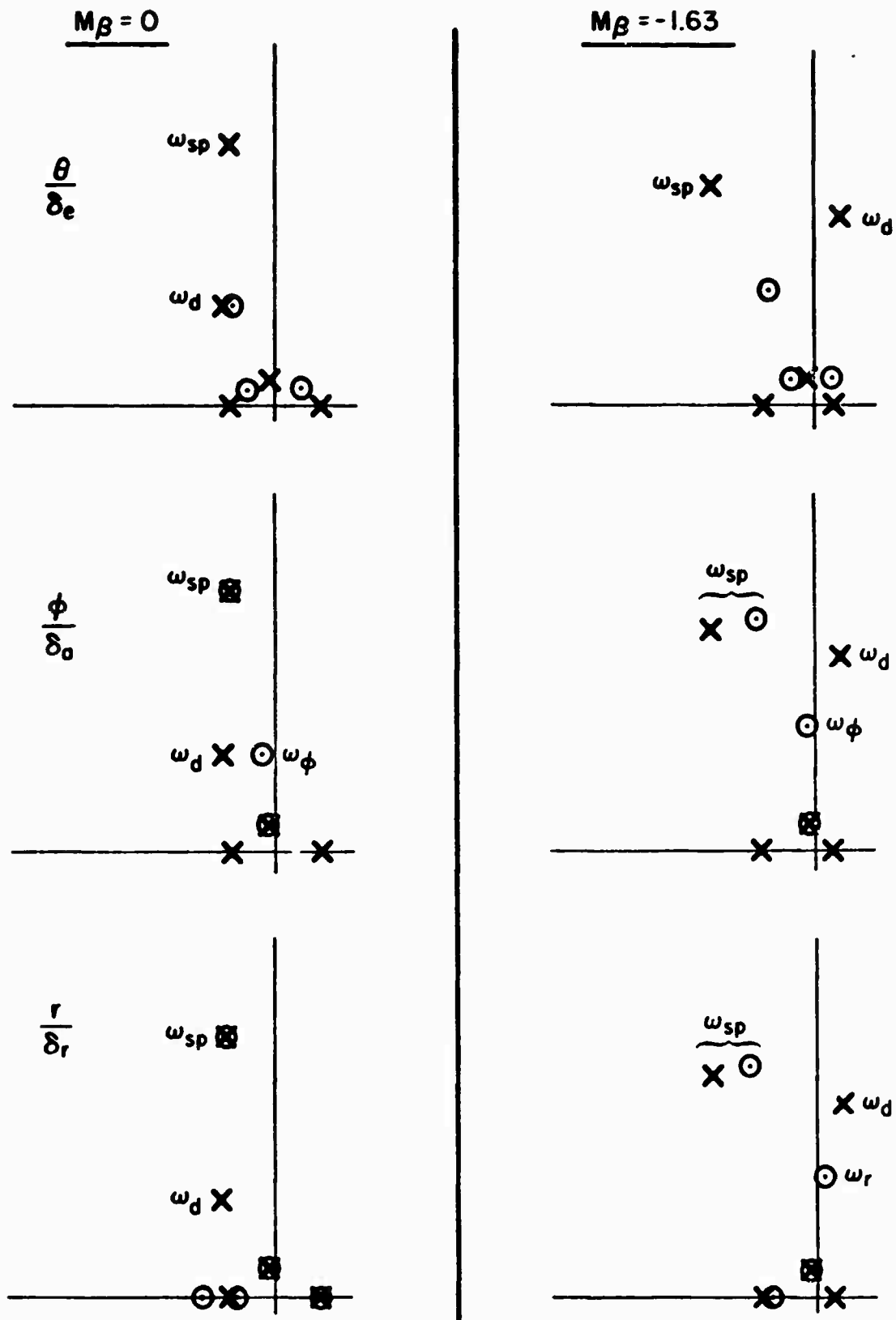
Figure 18. Effect of M_β on F-4 Poles and Zeros
($\alpha_0 = 20°$, $\beta_0 = 1°$)

42

case the M_β principally affects the lateral and longitudinal short-period modes with a resultant increase in ζ_{sp} and decrease in ζ_d. Further, it appears that with $M_\beta = -1.63$, closure of any or all of the three loops shown in Fig. 18 could easily result in an unstable dutch roll mode. These loops could be closed by the pilot (θ and φ) and the yaw rate damper.

The effect of M_β was verified with a 5 DOF analog simulation which produced a stable dutch roll for $M_\beta = 0$ and divergent dutch roll of $M_\beta = -1.6$. [It should be noted in passing that a similar shift in short-period modes was obtained in the Ref. 16 analysis of nonsymmetric flight effects. However, this was attributed to the coupling derivative l'_α.]

Figure 17 indicates that C_{m_β} changes sign depending upon the sign of β such that $M_\beta\beta$ is always negative. For M_β positive, linear analysis indicates the migration of the longitudinal short-period and dutch roll modes to be reversed from that shown in Fig. 18. That is, the longitudinal short period moves toward the right half plane while the dutch roll moves to the left. However, as shown below, other factors in the nonlinear 6 DOF model apparently bias the aircraft motion towards an unstable dutch roll.

At the request of the USAF, McDonnell-Douglas Aircraft Co. provided a collection of wing rock traces obtained during flight test of the slatted-wing aircraft. Typical of these are the 1 g stall traces shown in Fig. 19 (reproduced from Ref. 24) which reflect trim conditions very similar to those selected for the preceding analysis, i.e.:

$$h = 17,500 \text{ ft}$$
$$W = 37,410 \text{ lb}$$
$$\text{c.g.} = 29.5\% \text{ MAC}$$
$$M = 0.36$$

Clean aircraft

The traces indicate that:

   a. Wing rock is not a controls-fixed oscillation but
       appears to be caused by or aggravated by the pilot
       (i.e., a closed-loop phenomenon).

43

b. It is not uncommon to have a bias sideslip of one or more degrees during wing rock.

c. Relatively large bank-angle and sideslip excursions but small angle-of-attack oscillations are exhibited.

It was determined from the traces that the average gain between roll angle and lateral stick excursions reflect a pilot gain $K_{p_\varphi} \doteq 0.2$ deg/deg. Therefore, a closed-loop simulation was run utilizing the nonlinear 6 DOF airframe and a simple pilot model, $Y_p = 0.2\ e^{-.3s}$. The resulting traces are shown in Fig. 20 for an initial $\beta_0 = +1$ deg and Fig. 21 for an initial $\beta_0 = -1$ deg. These attempts at modeling the real aircraft traces show, in Fig. 20, that roll oscillations for $\beta_0 = +1$ deg grow much greater than the longitudinal oscillations. The roll divergence has approximately a 10 sec time to double amplitude and hence, over a time period of 30 to 40 seconds, could develop into a roll rate of about 30 deg/sec amplitude which would approximate that shown in the flight trace of Fig. 19. Figure 21 ($\beta_0 = -1$ deg) does not show the same oscillating divergence tendencies but it should be noted that the sideslip is steadily building toward a positive value which would then diverge as in Fig. 20. This is particularly interesting since the majority of the flight traces in Ref. 24 indicate the same bias toward ANL (positive) β. Thus, it appears that positive β, negative M_β, and pilot closure (intentional or inadvertent) of roll (attitude, rate, or acceleration) to aileron may be a significant contributor to wing rock.

Another investigation of possible sources of the F-4 wing rock included separation of the total roll damping coefficients

$$C_{l_r} - C_{l_{\dot\beta}} \cos \alpha$$

$$C_{l_p} + C_{l_{\dot\beta}} \sin \alpha$$

into the basic $\dot\beta$, r, and p contributions. The separation was based upon the coefficient data of Ref. 21 and resulted in the following sets of derivatives for the $\alpha_0 = 23$ deg, $\beta_0 = 0$ deg case:
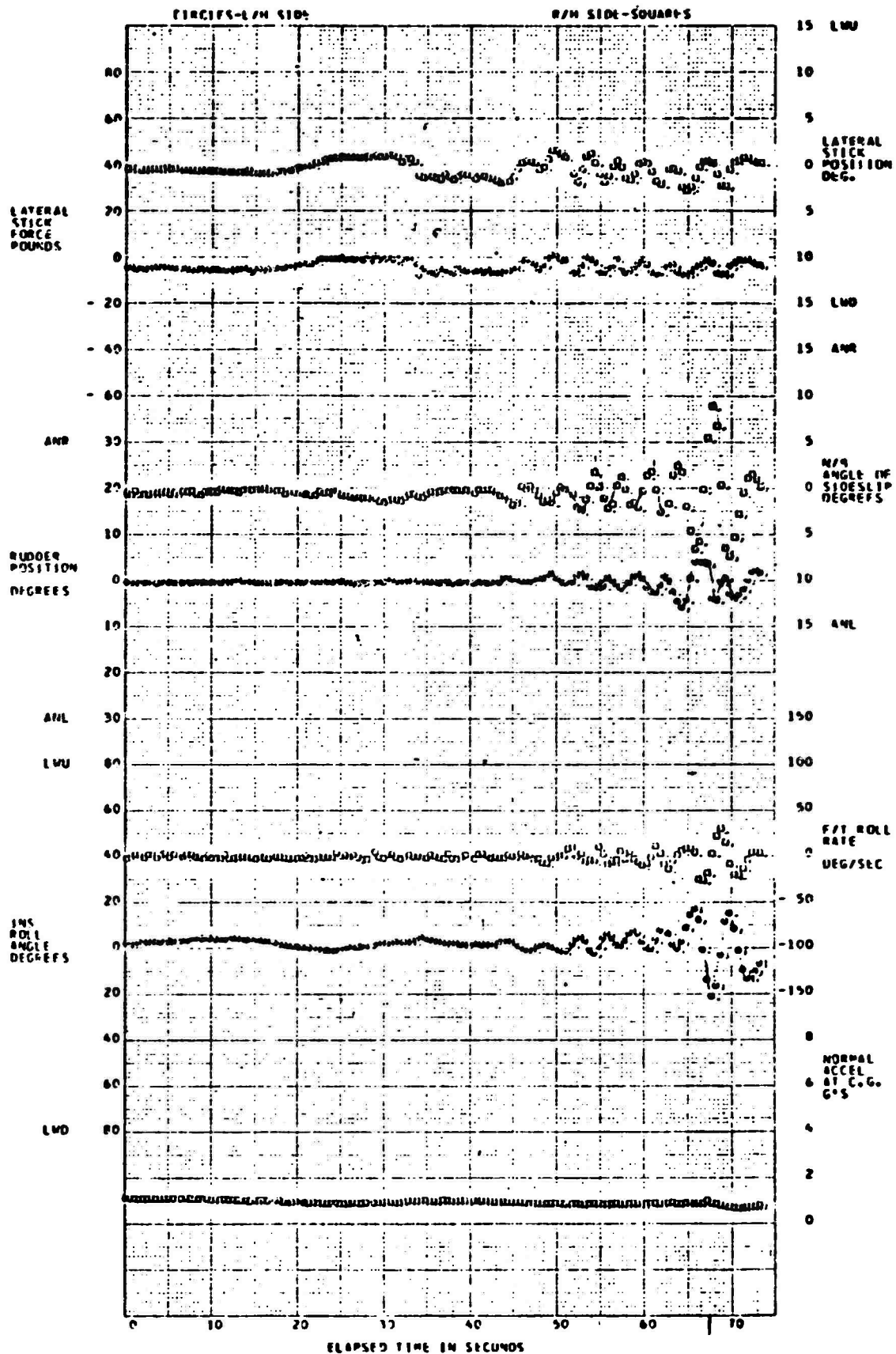
Figure 19. — Wing Rock
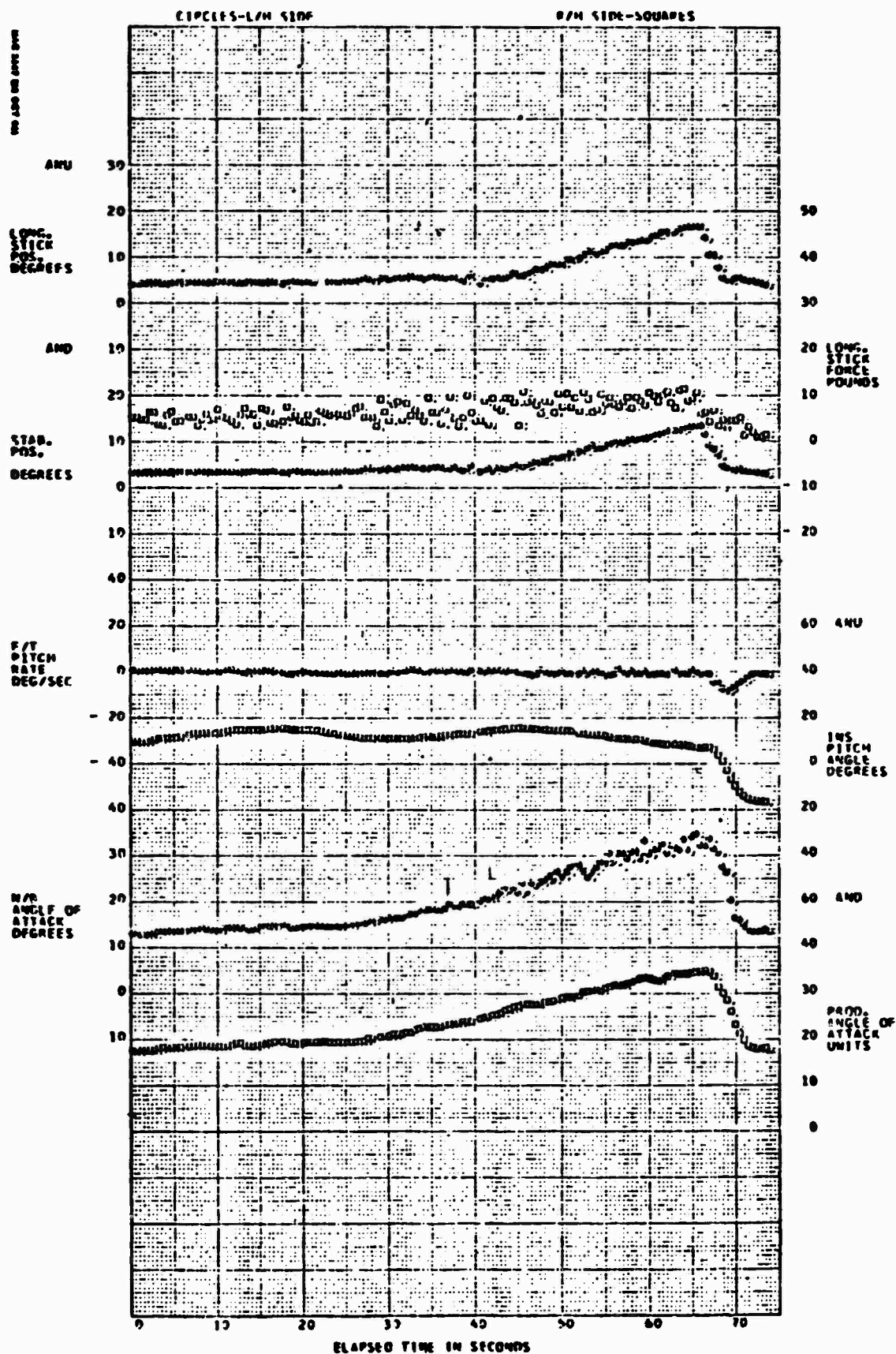
Figure 19. (Concluded)

46
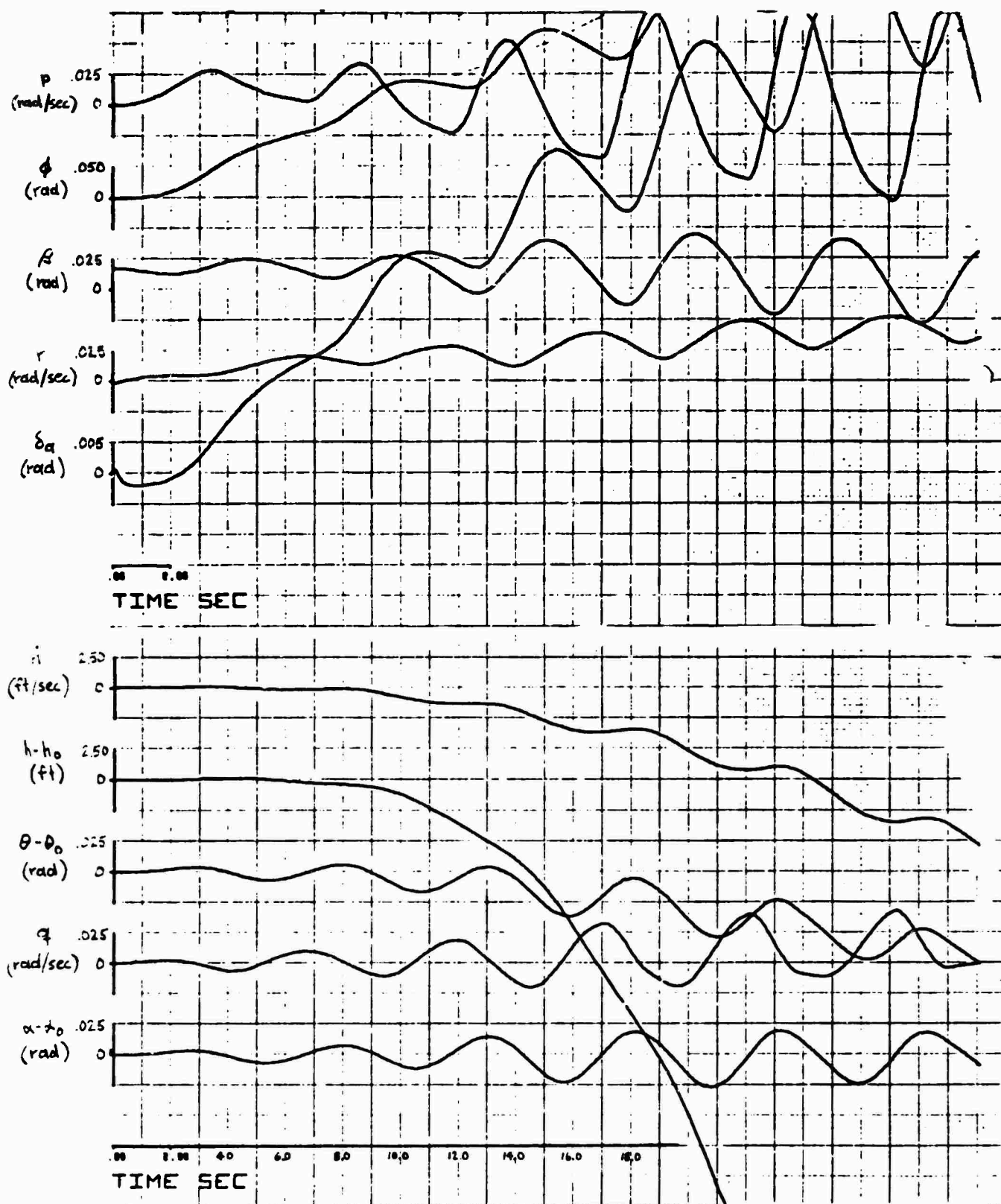
Figure 20. Closed-Loop Response for $\beta_0 = +1$ deg

47
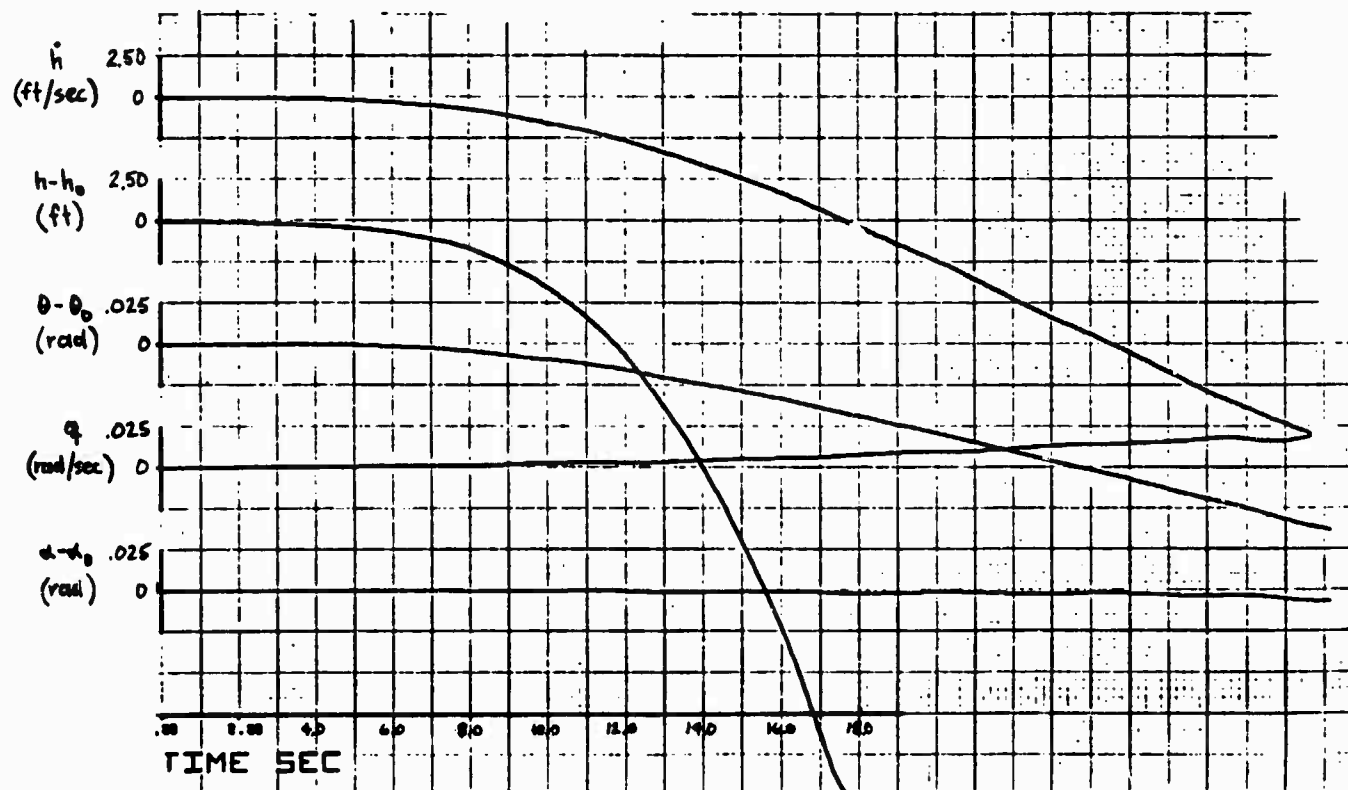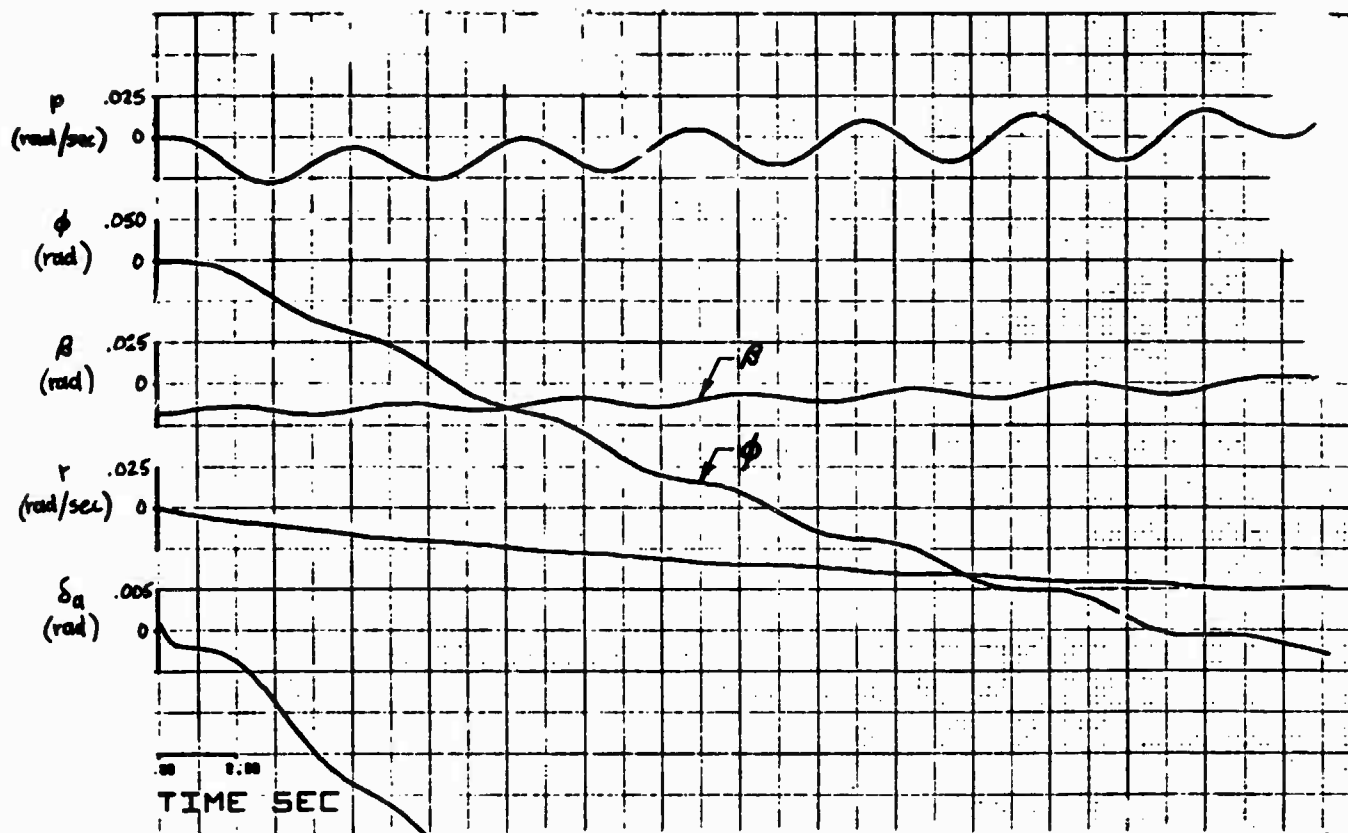
Figure 21.   Closed-Loop Response with $\beta_0 = -1$ deg

48

Before Separation	After Separation
$\mathcal{L}_{\dot{\beta}}' = 0$	$\mathcal{L}_{\dot{\beta}}' = -1.45$
$\mathcal{L}_r' = 1.74$	$\mathcal{L}_r' = 0.289$
$\mathcal{L}_p' = -0.688$	$\mathcal{L}_p' = 0$

Note this is for __symmetric__ ($\beta_o = 0$) flight. The effects were assessed via literal expansion of the three-degree-of-freedom lateral matrix and an analog simulation. Both showed little difference in the resulting lateral-directional dynamic characteristics and verified the acceptability of lumping all roll damping into an effective $\mathcal{L}_r'$ and $\mathcal{L}_p'$.

The possible influence of nonlinear C_{n_β} (Refs. 3 and 20) was also investigated using the five-degree-of-freedom analog simulation. In this instance the nonlinearity in N_β' was modeled after the C_{n_β} slopes indicated in Refs. 3 and 20, i.e., C_{n_β} reversals at 5 to 10 deg β. The results were similar to those of a bang-bang control system operating with a large dead zone; the aircraft drifted through the unstable β range and then developed a limit cycle type oscillation __about__ the stable C_n vs. β intercept point (e.g., 10 deg β). This is not compatible with flight traces. Similar nonlinear representations of C_{ℓ_β} and C_{n_β} were attempted with no improvement in results.

Since the most promising causal factors appeared to be the basic longitudinal-lateral coupling of the F-4 in nonsymmetric flight, an attempt was made to induce wing rock in the A-7 by modifying key stability derivatives. The principal difference between the derivatives of the F-4 and A-7 at comparable high α has been shown previously to be in $\mathcal{L}_r'$, N_α', $\mathcal{L}_\beta'$, N_β', and M_β. Therefore, these A-7 derivatives were rescaled on the basis of the differences in vehicle mass, inertia, wing area, etc., and new derivatives obtained for a "pseudo F-4." These are summarized as follows:

	F-4	A-7	PSEUDO
α_0	20	18.8	18.8
β_0	1	6	6
$\mathcal{L}_r'$	1.268	0.3323	1.21
$\mathcal{L}_\beta'$	0.1908	−4.46	0.16
N_α'	−0.505	−1.425	−0.67
N_β'	0.32	0	0.424
M_β	−1.63	0	−1.54

These new values were incorporated in the nonlinear five-degree-of-freedom analog simulation of the A-7 and evaluated as a potential configuration for the piloted simulation discussed in Section IV. The change in derivatives did result in an oscillatory behavior quite similar to that shown in Fig. 16 but having a lower frequency and larger amplitude about all three axes. When assessed by the evaluation pilots in a target tracking task the behavior was not considered representative of wing rock (open or closed loop). Rather, the nose of the aircraft tended to describe a circular motion about the target. This simulation was not pursued further.

2. Summary and Conclusions

Various open- and closed-loop parameters and aerodynamic coefficient anomalies which have been suggested in the technical literature as potential causal and/or contributing factors to the F-4 wing rock have been investigated. The only situation found to produce open-loop oscillatory characteristics in a nonlinear, six-degree-of-freedom digital model is nonsymmetric $(\beta \neq 0)$ flight at high α. The principal factor appears to be the coupling derivative M_β which has a destabilizing influence on the short-period (lateral and/or longitudinal) modes. The resulting oscillatory motion is apparent as angular rates and displacements about all three aircraft axes of approximately equal magnitudes and therefore does not specifically resemble wing rock.

Study of all available flight traces which present aircraft motion and control input (or surface) provide strong evidence that the F-4 phenomena is

closed loop. Significant lateral stick activity is generally observed to accompany the predominately rolling/sideslipping wing rock motion. Incorporation of a simple roll control pilot model in the above nonlinear, six-degree-of-freedom digital simulation and adjustment of the feedback gain to match that observed in flight traces resulted in an oscillatory roll divergence which could grow into wing rock.

An attempt to change the departure characteristic of the A-7 aircraft from nose slice to wing rock proved partially successful. Scaling of five key stability derivatives to resemble those of the F-4 did result in an oscillatory characteristic; however, it did not have the predominate roll characteristic of wing rock.

SECTION III

SIMULATION DESCRIPTION

This section describes in general terms the five-degrees-of-freedom piloted simulation. Details are contained in Volume II, Appendix IV.

The simulation involved two basic tasks:

- Assess flying quality parameter influences on

    - Departure susceptibility/resistance (warning)

    - Departure and recovery characteristics

    - Pilot flying technique in the stall/departure flight regime

- Measure pilot dynamic control parameters in the stall/departure flight regime

To provide meaningful data, the vehicle dynamics had to be a realistic representation of high angle-of-attack flying characteristics. However, to maintain control over, and vary only, specific key parameters as well as to avoid unnecessary complication which might confound the experiment, it was desirable to employ the simplest possible simulation mechanization. As indicated in the previous section, a nonlinear five-degrees-of-freedom analog simulation was deemed to satisfy both sets of requirements. The adequacy of this simulation was validated by two means. First, a dynamic check was made against a nonlinear six-degrees-of-freedom digital model. Secondly, the simulation was evaluated by two U. S. Air Force experimental flight test pilots who are experienced in the A-7 aircraft. One pilot flew the A-7 between sessions in the simulator to specifically assess and compare the simulated and actual vehicle characteristics. Following a few minor adjustments both pilots pronounced the simulation to be a good replica of the A-7 characteristics. Once validated, the appropriate flying quality parameters were then varied and a series of experiments performed which will be covered in later sections.

A. GENERAL LAYOUT AND OPERATION

The functional layout of the simulation facility is shown in Fig. 22. A fixed base fighter cockpit was employed which contained a full complement

of flight instrument displays including an **all-attitude ball**. An **out-the-window** display was provided in front of the windshield via a large CRT screen. This resembled, somewhat, the basic H.U.D. of the A-7. **Control system feel** was adjusted to match the A-7 breakout and force gradients as closely as possible. A pedal shaker was activated as the aircraft neared **stall**. **Air-frame dynamics** and display geometry were modeled on two EAI 231R **computers** with associated nonlinear racks. The equation **flow diagram for the aircraft** and display systems is presented in Fig. 23. The left side of this **figure** reflects mechanization of the airframe equations. The **lower right side** reflects mechanization of the target aircraft and the **differential motion** between target and the controlled aircraft. **Lateral and normal acceleration** as sensed by cockpit instruments were also calculated. The **upper right** portion of Fig. 23 reflects the complications in mechanizing the **derivatives** which varied as functions of initial, perturbation and total α and β.

B. AIRCRAFT MODEL

The five-degrees-of-freedom airframe model was obtained by removing the X equation from the matrix of Fig. 2 and varying six key derivatives in the lateral equations as a function of α and β. These equations also reflect the analog mechanization limitations which required assuming $\tan \beta \doteq \sin \beta$. The adequacy of these approximations were verified by the comparison of the nonlinear 5 DOF analog and 6 DOF digital simulations as already reviewed in Section II (e.g., Figs. 6, 9, and 10). Since the aircraft stalls at approximately 29 deg α and it was desired to start the simulation runs somewhat below stall, straight-line fits were made to the derivatives only for the α range 17 to 23 deg, and these were then extrapolated to 30 deg α. Similarly, the derivative variation with sideslip was fitted over the β range 0 to ± 8 deg and then extrapolated to larger β. The two derivatives which varied con-tinuously with α and β are shown in Fig. 24. $\mathcal{L}'_\beta$ varied linearly with α until well past the stall and linearly with β to 4 deg where it became constant for further increases in β. $\mathcal{L}'_\alpha$ varied linearly with β for all α but not with α until approximately 21 deg. Above 21 deg it rapidly decreased with further α increase and changed sign at approximately 23 deg α. This was modeled as a constant slope with β to 21 deg α and then a decreasing slope with further α increase.

CONTROLS

DISPLAYS

COMPUTER INTERCONNECT

COMPUTERS

DYNAMIC VARIABLES

INTERFACE AND RECORDERS
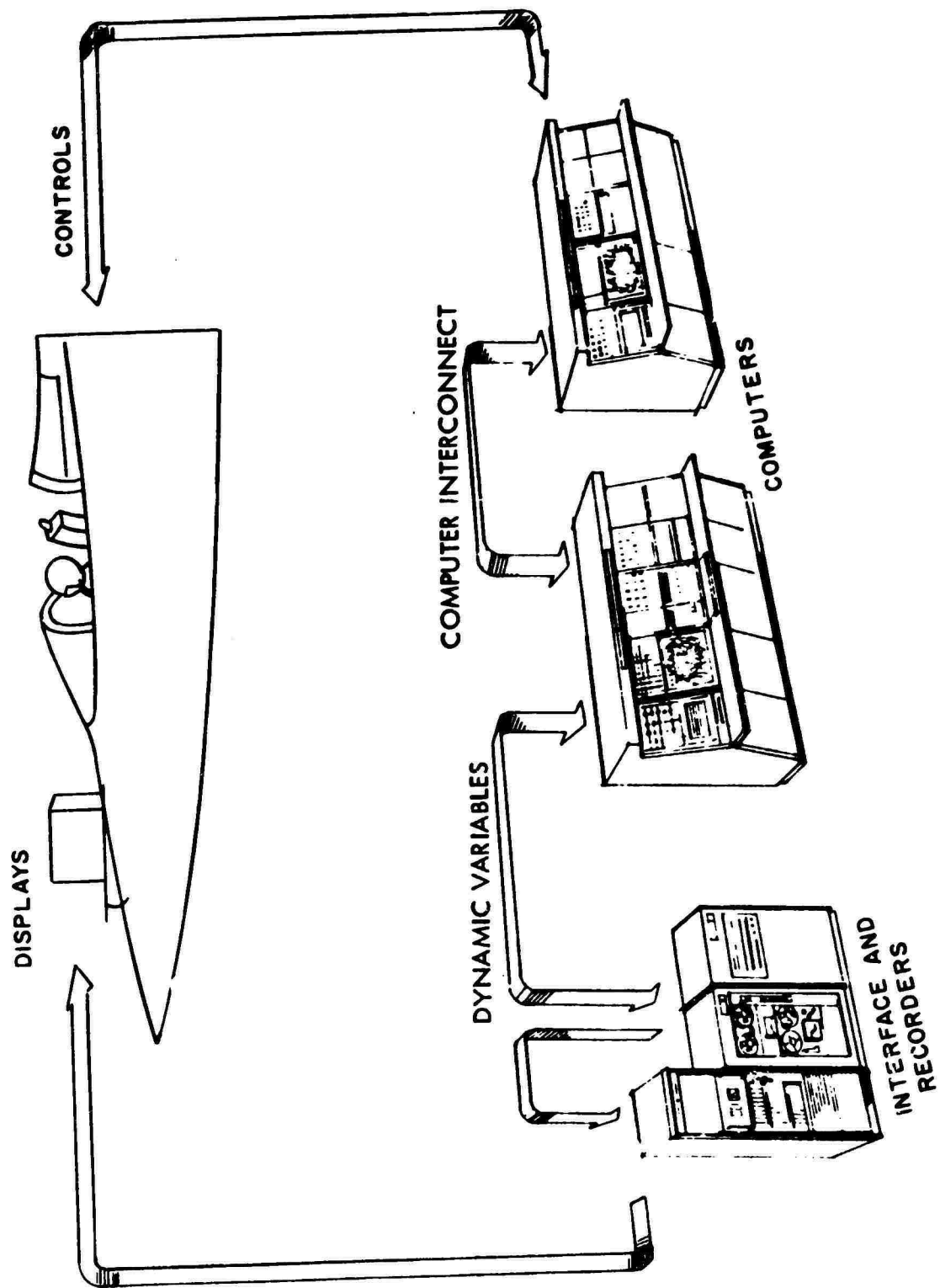
Figure 22. Simulation Block Diagram

54
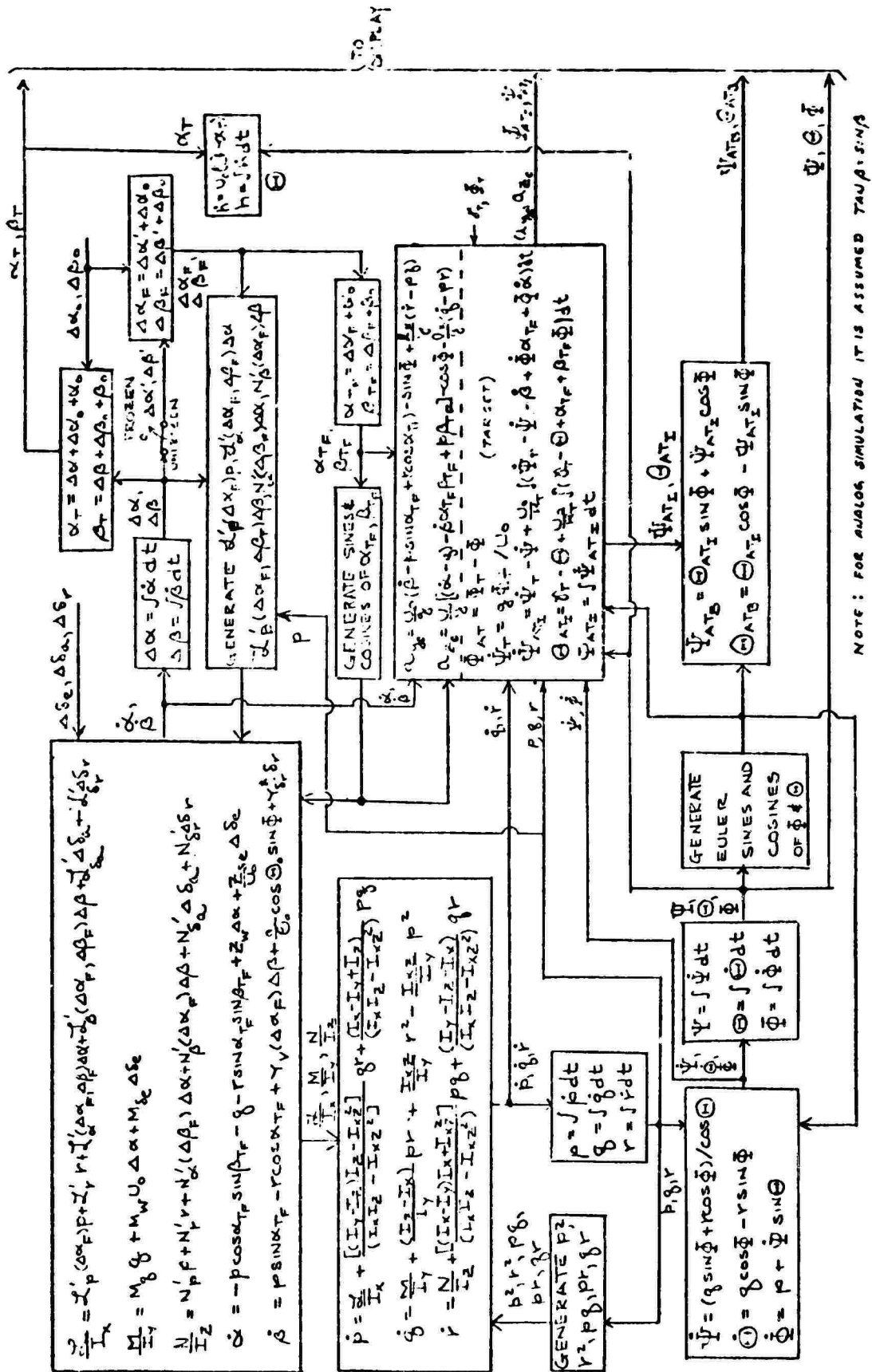
Figure 23. Aircraft and Display Simulation System Equation Flow Diagram
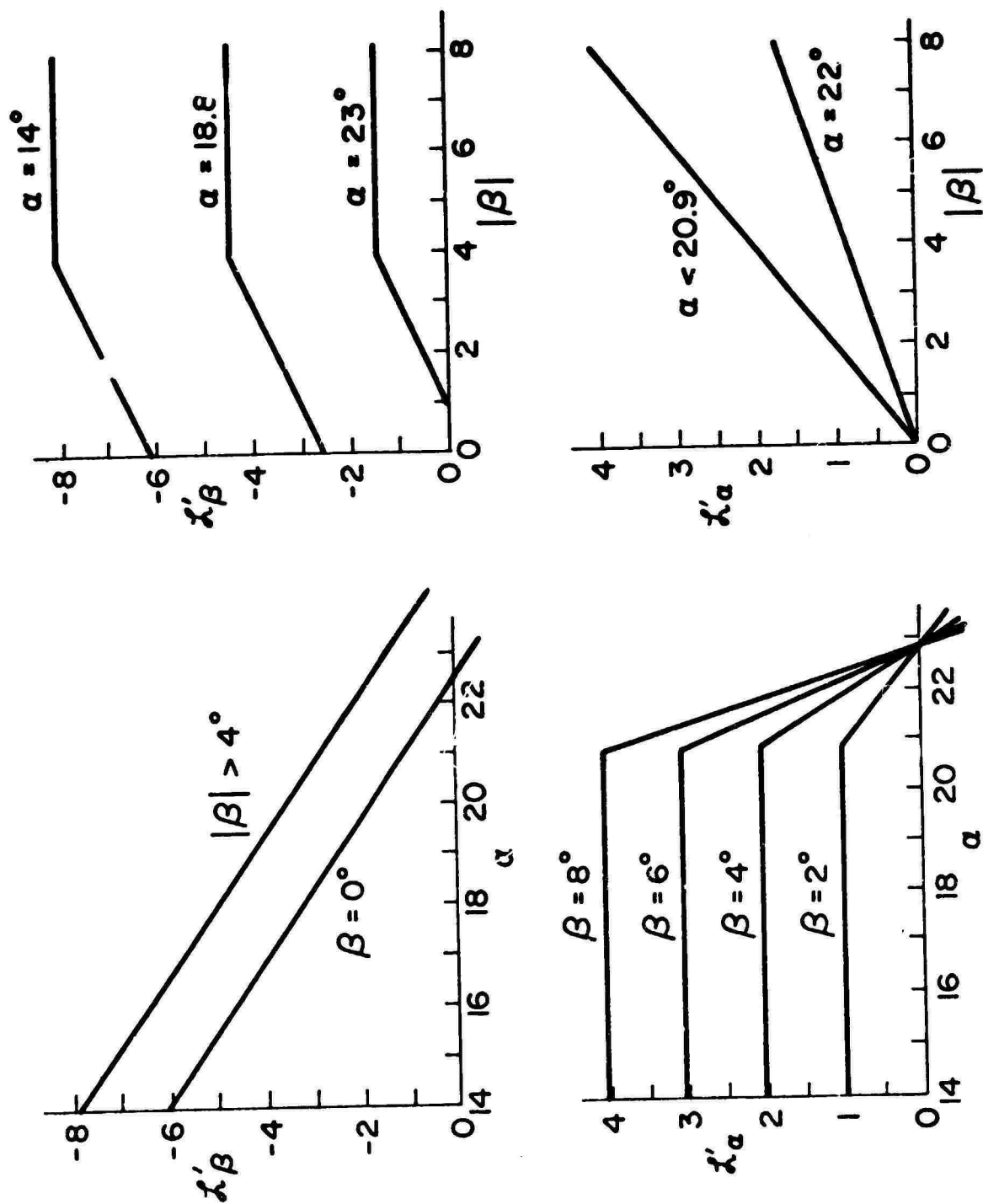
Figure 24. Derivative Variation with α and β

Three derivatives were varied linearly as a function of α only (Fig. 25).
These are $\mathcal{L}_p'$, Y_v, and N_β'. The latter changes sign at approximately 19 deg α.
N_α' was varied linearly as a function of β only. The remaining thirteen
stability derivatives were maintained fixed throughout the simulations runs
although different initial values of some were employed to achieve desired
changes in pertinent flying quality parameters. Numerical values are given
in Appendix D of Volume II.

The derivative mechanization described above provided a relatively
uncomplicated airframe model yet afforded the time trace matches reflected
in Figs. 9 and 10.

The contributions of the pitch and roll rate command augmentation and
yaw stability augmentation systems were not modeled. In the actual aircraft
the roll rate CAS is automatically faded out in this α range because it
produces pro-departure surface deflections. Therefore, it need not be
simulated. Analysis of the other two fixed gain systems indicated their
contributions to be insignificant at the low dynamic pressure of the con-
ditions being simulated.

C. DEPARTURE/RECOVERY DISPLAY AND TASK

A task approximating an air-to-air tracking tail-chase was presented on
the head-up display. A view which shows the head-down and head-up display
is shown in Fig. 26. A symbol representative of own-aircraft centerline was
fixed at the center of the CRT face. The target and horizon then moved with
respect to the own-aircraft centerline symbol. The head-up field of view
was ± 24 deg in azimuth and ± 18 deg in elevation. The subject aircraft could
be maneuvered in bank, pitch and heading relative to the target $(\Phi_{AT}, \Psi_{AT_B},$
Θ_{AT_B} in Fig. 23). Sustained attitude deviations would result in lateral or
vertical displacement with respect to the target. Only range to target
remained fixed at 2000 ft. The subject aircraft pitch and roll attitude
could be discerned with respect to the horizon (Φ, Θ), while the target
aircraft in view provided a reference for judging heading or turn rate from
the head-up display. Without the target aircraft, the pilot could not
detect nose slice or onset of departure until a rapid roll, discernible
from motion of the horizon, would develop. (A similar A-7 simulation reported
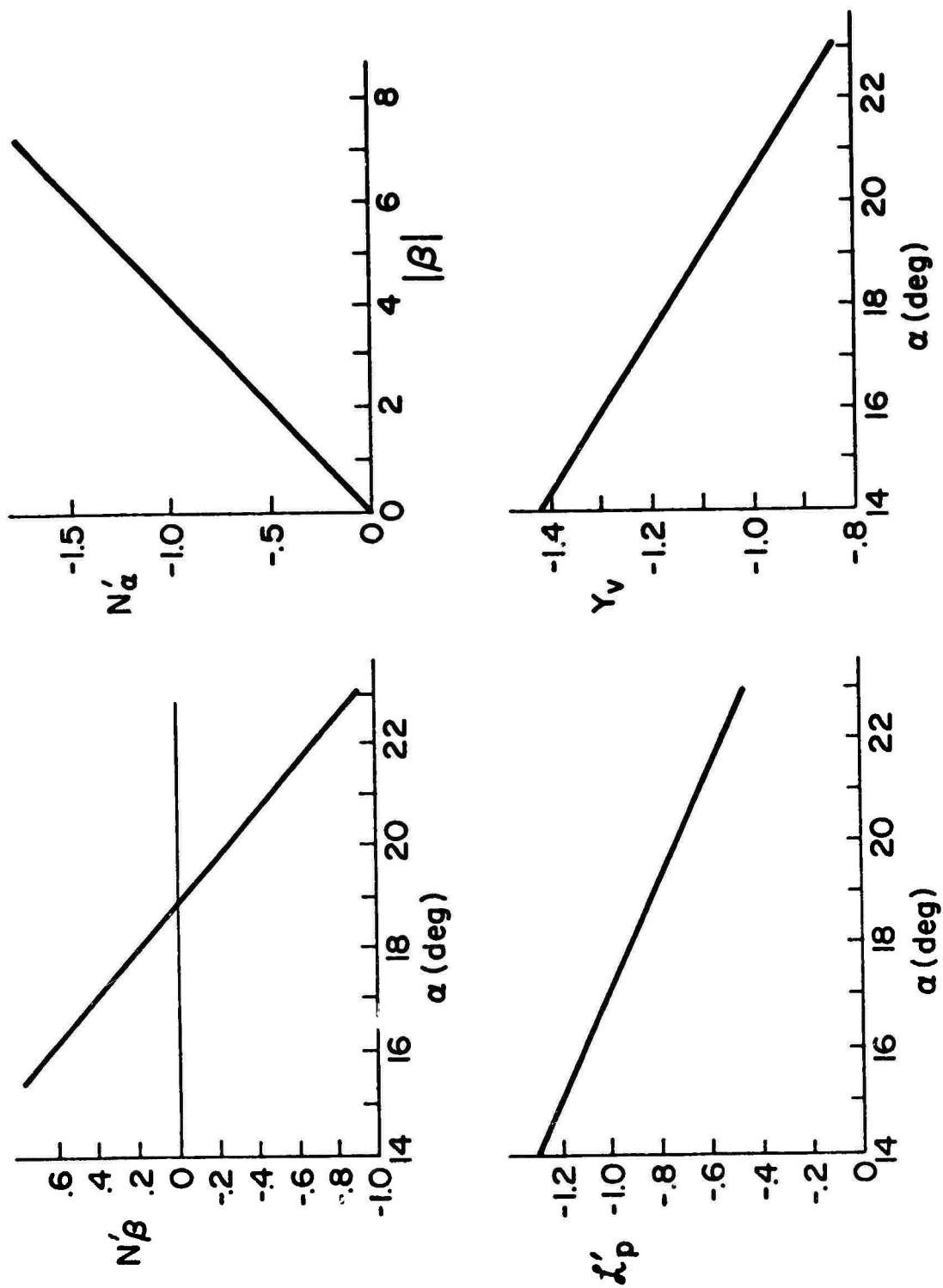
Figure 25. Derivatives Varied with α or β

Figure 26. Outside and Inside Display

in Ref. 25 had only a head-down display and the basic departure was described as a roll departure.) In actual flight the pilot has two cues. One is the lateral motion of the nose of the aircraft with respect to cloud texture or a target aircraft. The second is a rather significant side force as sideslip and lateral acceleration develop. To partly compensate for the lack of lateral acceleration cue, a replica of the ball of the turn and slip indicator was also displayed on the CRT screen. This proved helpful to the pilot in detecting that something was happening or about to happen, because he could detect motion of the peripheral vision. However, once the ball was pegged at either side of its displacement it was of little value as a cue except when the aircraft was nearly under control following a departure; the pilot could then actually look at the ball and determine the rudder input required to achieve final coordination and recovery. During recovery with the target or horizon line not within view, the pilot could revert attention inside the cockpit to the attitude ball which displayed Φ, Θ, Ψ.

Pilot comments on the display were that it was quite similar to flying tail chase using the actual A-7 head-up display. As indicated previously, the target was required to be in view for the pilot to obtain a nose slice cue at high angles of attack. A continuous digital readout of angle-of-attack and sideslip was displayed above the head-up display to help the experimenter and pilot analyze departures, control functions and recoveries. These were most helpful to the experimenter while observing pilot control activity and apparent detection of departure. These digital displays were also of benefit to the pilot in analyzing the departure characteristics and the effects of his control inputs by placing the computer in hold and then observing all of the motion quantities displayed.

D. PILOT PARAMETER MEASUREMENTS

Measurement of pilot dynamic parameters was accomplished through use of a Describing Function Analyzer (DFA) as described in detail in Refs. 26 and 27. Briefly, the DFA is a device for making on-line dynamic response measurements of manual control systems. It generates a sum-of sinusoids input forcing function that is used to excite the dynamic system under consideration; and computes, on-line, the finite Fourier transform of a

given system signal at each of the forcing function frequencies. A sketch of the interconnection is shown below. In this instance the dynamic system to be analyzed is the combined pilot and airframe with the airframe dynamics known and the pilot dynamics to be determined.

$$i(t) = \sum_{i=1}^{5} A_k \cos(\omega_k t + \phi_k)$$
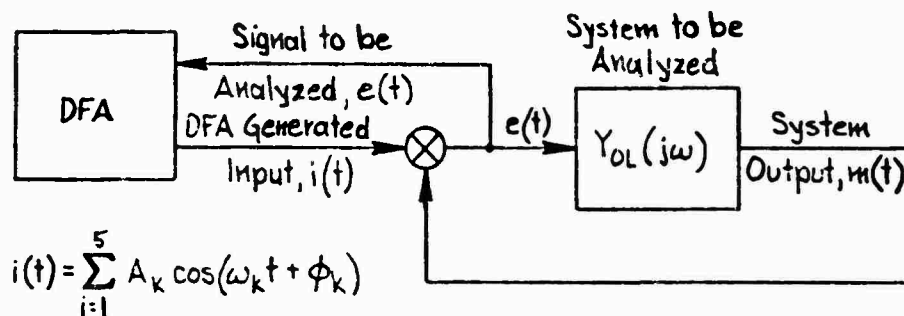
The real and imaginary components of the Fourier transform are integrated during a run and available immediately at the end of the measurement period. The finite Fourier transform of error signal at input frequencies ω_k is

$$E(j\omega_k) = \text{Re}[E(j\omega_k)] + j\text{Im}[E(j\omega_k)]$$

where

$$\text{Re}E(j\omega_k) = \frac{2}{t_R} \int_0^{t_R} e(t) \cos(\omega_k t) \, dt$$

$$\text{Im}E(j\omega_k) = \frac{2}{t_R} \int_0^{t_R} e(t) \sin(\omega_k t) \, dt$$

Off-line calculations are then required to obtain the error-to-input describing function

$$Y_{ie}(j\omega_k) = \frac{E(j\omega_k)}{I(j\omega_k)} = \frac{\text{Re}[E(j\omega_k)] + j\text{Im}[E(j\omega_k)]}{A_k}$$

and the desired open-loop (system output-to-error) describing function

$$Y_{OL}(j\omega_k) = \frac{1}{Y_{ie}(j\omega_k)} - 1$$

To obtain pilot describing functions in multiaxis tracking situations, past laboratory procedures have involved simultaneous introduction of separate, uncorrelated, forcing functions in each axis. This permits direct determination

61

of describing functions for each axis as well as for cross-talk or noise between axes. Unfortunately this does not provide a realistic forcing function for simulation of air-to-air tracking where between-axis target motion is correlated. That is, there are certain basic relationships between target bank, pitch and heading for any useful aircraft maneuver. It is not likely, for example, that a target will bank into a turn and then pitch away from the turn (i.e., negative g turn). Such apparent target motions are rejected by a pilot as sight noise due to buffet, pipper wander, etc. Thus, to provide a realistic input which experienced fighter pilots would track, it was necessary to introduce the forcing function input to one axis at a time (Fig. 27) and depend upon stationary run-to-run performance. The amplitude and frequency of the five sinusoids employed in the forcing functions are shown in Fig. 28.

The measurement of pilot describing functions with the DFA requires a linear, stationary control process. Therefore the airframe dynamics were "frozen" for the data runs. This was accomplished by fixing all airframe stability derivatives at the value appropriate for the given trim condition and aircraft configuration.

a) Roll Tracking Task

Input	Measure
ϕ_T	ϕ/ϕ_e

b) Pitch Tracking Task

Input	Measure
θ_T	θ/θ_e
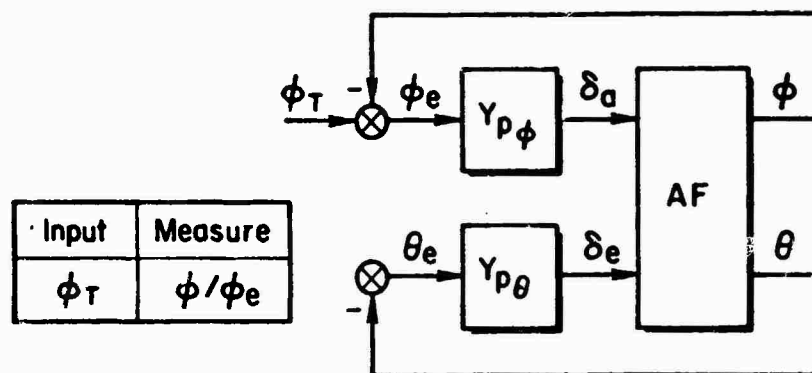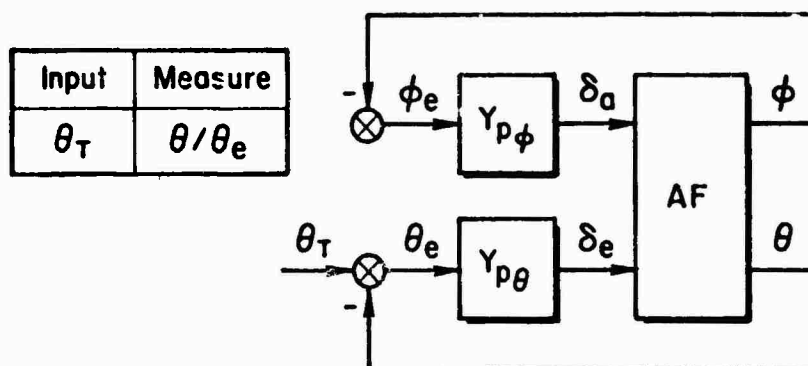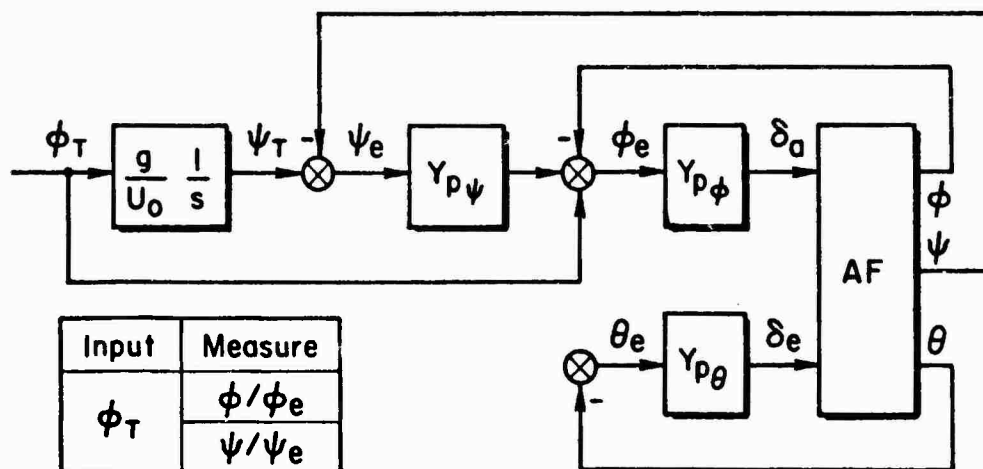
c) Heading Tracking Task

Input	Measure
ϕ_T	ϕ/ϕ_e
	ψ/ψ_e

Figure 27.   Tracking Task Loop Structures

63
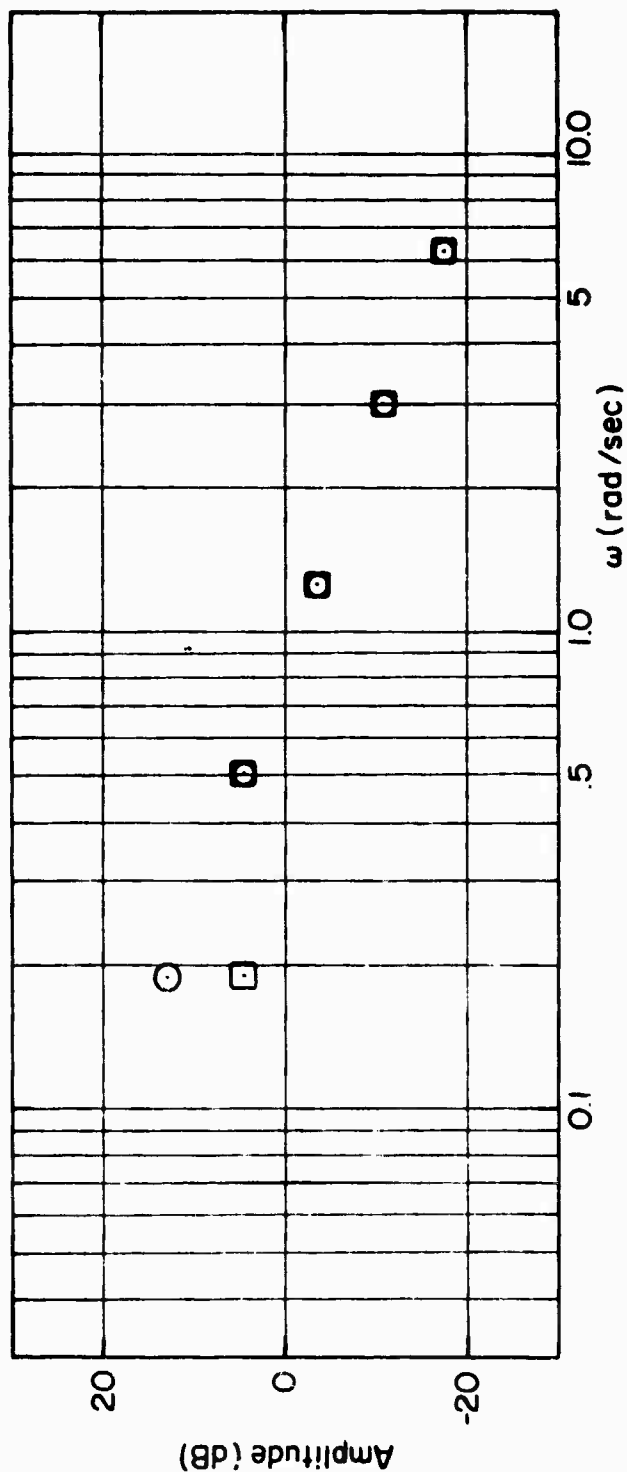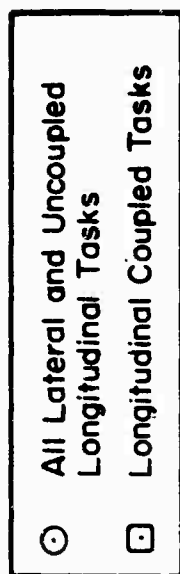
Figure 28. Forcing Function Spectrum

SECTION IV

FLYING QUALITY PARAMETER ASSESSMENT

This section presents an analysis of quantitative and qualitative results obtained in the five degree-of-freedom piloted simulation of varied departure/ recovery flying quality parameters. Attention was concentrated on nose slice departures and the effect of key derivatives on departure and recovery characteristics. Emphasis is placed on physical understanding of the departure and recovery dynamic characteristics, i.e., a correlation of open- and closed-loop modes, pilot commentary, and strip chart recordings.

It is shown that previously suggested lateral-directional stability and departure parameters do not correlate with the departure characteristics and pilot ratings obtained here. The only parameter which appears consistent is the coupling zero of the $\theta \rightarrow \delta_e$ numerator. The results obtained are confounded by a significant difference in piloting technique between the two test subjects.

A. PILOTING TASK

The basic task was to track a target which led the pilot into a stall and/or departure. The initial condition placed the aircraft wings-level in-trail to the target. A ramp target flight path input of 1 deg/sec was commanded to obtain a consistent rate of stall approach. The pilot then followed the target aircraft flight path until departure motion was detected and/or he felt he could no longer follow the target aircraft and still achieve a successful recovery. The task thus represents a straight-ahead, paced, stall approach. Since pilots normally evaluate stall characteristics of new aircraft configurations by performing wings-level 1-g stalls, this type of display and tracking task assisted the pilots in correlating the simulator displayed motions with previous flight experience; and in assigning Cooper-Harper ratings to the various configurations and maneuvers. A wind-up turn target following maneuver was also simulated. This, however, resulted in an identical tracking task to the straight-ahead wings level

task except that the target and own-aircraft were banked with respect to the horizon. The pilots could detect no basic difference in the tasks or in the motions and therefore the wind-up turn was discontinued.

The departure cue was onset of uncommanded nose yaw with respect to the target aircraft or the realization by the pilot that the controls were ineffectual in returning his aircraft to the desired flight path. Two control strategies were employed following detection of departure. The first was to apply sustained resistive control, that is, attempt to maintain existing pitch attitude at departure detection and then to apply lateral-directional controls as necessary to resist the departure. The second was to relax longitudinal control to the zero-force stick trim position or to apply forward stick force. Five separate recovery techniques were investigated with this relaxed longitudinal stick control:

   A. Aileron and rudder neutral

   B. Aileron only to regain control

   C. Rudder only to regain control

   D. Aileron and rudder to regain control

   E. Same as D except $\mathcal{X}'_{\delta_r}$ reduced by a factor of four

In addition to strip chart recordings of the various aircraft motions, pilot commentary was recorded continuously. This commentary included a description of the departure warning and its adequacy, control technique employed, recoverability of the aircraft, and the Cooper-Harper rating of the recovery task. The edited pilot commentary is presented in Volume II.

The plan was to start each run with the aircraft at an initial condition of 18.8 deg α and 6 deg β. This resulted in such a rapid departure onset that the pilots could not react in time to delay the departure or accomplish recovery. The sideslip initial condition was then reduced to 3 deg. This proved satisfactory from a control standpoint; however, it soon became apparent that the pilot would get in a "groove" because the nose slice was always in the same direction. Thus, the pilot would anticipate the nose slice motion and apply corrective controls in an essentially precognitive manner. For the final data runs the aircraft initial condition was set to 18.8 deg α and 0 deg β. With these trim conditions the aircraft would depart in either direction and this depended, in part, on the random buildup of sideslip due

66

to control activity in tracking the target. This initial condition also afforded several seconds of relatively "precise" tracking and allowed the pilot to obtain a feel for the aircraft as it approached the stall and departure.

The analysis to follow is based on a representative 3 deg β since this generally reflects the initial departure situation (i.e., warning and detection).

E. PARAMETER VARIATIONS AND RESULTS

Nine aircraft dynamic configurations were employed in the simulation. Configuration 1 represented the nominal A-7 dynamics. Key stability derivatives were changed (in the simplified manner described in Section III-B) to selectively control the initial condition values of the open- and closed-loop handling quality parameters $1/T_{\theta_3}$, ω_{SR}, ω_φ, ω_φ/ω_d, $N_{\beta_{dyn}}$, and ζ_d, which then varied as a function of α and/or β as the aircraft approached stall. The strategy was to first worsen the coupling divergence parameter ($1/T_{\theta_3}$) and selectively improve the lateral handling parameters as indicated for Configurations 1 through 3 in Table 6. Secondly, the divergence parameter was improved and, again, the individual lateral parameters were varied as indicated for Configurations 4 through 9 in Table 6. Representative values of the parameters (and derivatives) at $\alpha_o = 18.8$ deg and $\beta_o = 3$ deg for all nine configurations are tabulated in Table 7.

1. Configuration 1

Figure 29 shows a typical migration of airframe open-loop poles and zeros with fixed α and varying β. The arrows indicate movement of poles or zeros as β is increased. The important points are:

- There is relatively slight movement of all poles for $0 < \beta < 6$ deg; dutch roll damping decreases.

- The two $N_{\delta_e}^\theta$ real zeros move toward the right half plane and there is large increase in ω_{d_θ}, with large increase in mid-frequency amplitude.

- The mid-frequency zero ω_φ moves with ω_d so that ω_φ/ω_d remains relatively constant; the roll transfer function is K/s^2-like and requires pilot compensation for significant closed-loop control.

TABLE 6. CONFIGURATION CHANGES

CONFIGURATION	CHARACTERISTIC OR REASON
1	Nominal A-7
2	Increase divergence rate of nose slice associated with RHP zero $1/T_{\theta_3}$ Eliminate adverse aileron yaw and subsequent excitation of Dutch roll mode Retain coupled spiral/roll subsidence or lateral phugoid mode
3	Increase divergence rate of nose slice Eliminate lateral phugoid Moderate decrease in aileron excitation of Dutch roll mode
4	Eliminate nose slice associated with RHP zero $1/T_{\theta_3}$ Eliminate adverse aileron yaw and excitation of Dutch roll mode Retain lateral phugoid
5	Eliminate nose slice associated with RHP zero $1/T_{\theta_3}$ Retain large aileron excitation of Dutch roll and near roll-reversal characteristic for aileron control of bank Retain lateral phugoid Increase $N_{\delta dyn}$
6	Eliminate nose slice associated with $1/T_{\theta_3}$ Retain near nominal ω_p/ω_d Eliminate lateral phugoid Decrease $N_{\beta dyn}$
7	Same as 6 above Decrease $\mathcal{L}_\delta$ to determine effect on roll rate obtained in departure and/or recovery
8	Provide RHP zeros in both longitudinal and lateral attitude control tasks Provide initial RHP poles (lateral phugoid) Both of above accomplished by making $N_{\beta dyn} = 0$
9	Provide nominal nose slice associated with $1/T_{\theta_3}$ Provide "good" roll-subsidence and spiral characteristics Degrade Dutch roll damping

TABLE 7

MATRIX OF HANDLING PARAMETER VALUES AT $\alpha_o = 18.8$ deg, $\epsilon_o = 3$ deg

CONFIG-URATION	$1/T_{\theta_3}$	ω_{SR} $(1/T_s)$	ζ_{SR} $(1/T_R)$	ω_d	ζ_d	ω_ϕ $(1/T_{\theta_1})$	ζ_ϕ $(1/T_{\theta_2})$	ω_ϕ/ω_d	$N_{\beta dyn}$	$N'_p - \frac{g}{U_o}$	L'_α	L'_β	N'_α	N'_β	N_{δ_a}	N'_p	L'_p
1	-.105	.238	.974	1.103	.2965	.572	.249	.518	1.28	.17 →	1.55 →	-4.0 →	-.712	0	.051	.02 →	-.85 →
2	-.259	.244	.957	.997	.302	.997	.184	1.0	1.28				-1.6	0	.1		
3	-.216	(.064)	(.461)	1.14	.238	.808	.176	.71	1.58				-1.6	.3	.051		
4	.015	.235	.982	1.05	.294	.992	.186	.944	1.28			-4.0	-.3 →	0	.1		
5	.015	.231	.978	1.25	.25	.668	.213	.534	1.77		1.55	-5.55		0	.051 →		
6	.015	(.222)	(.309)	.6245	.44	.392	.363	.628	.56		.75	-1.75		0			
7	.015	(.222)	(.309)	.628	.44	.392	.363	.628	.56		1.55	-1.75		0			
8	-.033	.304	-.583	.818	.878	(.781)	(-.496)	—	0	.17	1.55	-1.75	-.3	-.5	.031	.02	-.85
9	-.071	(.03)	(.53)	1.29	.034	.87	.14	.675	1.68	-.064	1.55	-4.0	-.712	+.4	.031	-.06	-.4
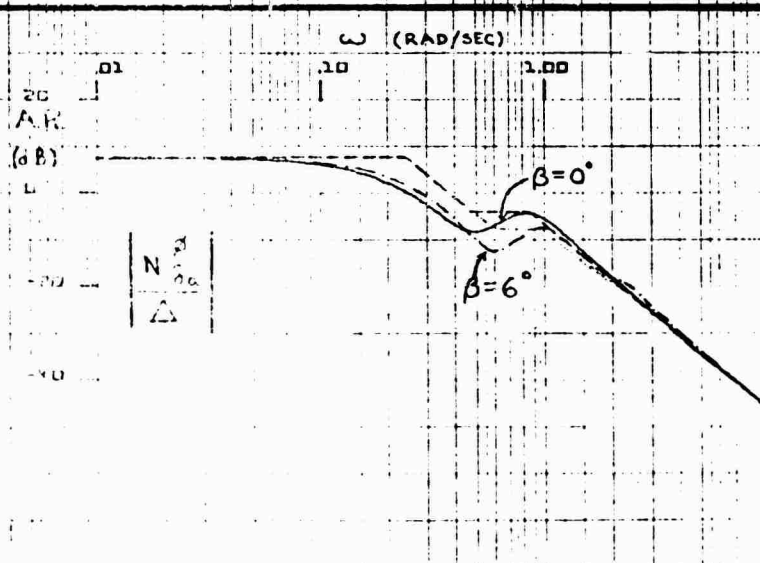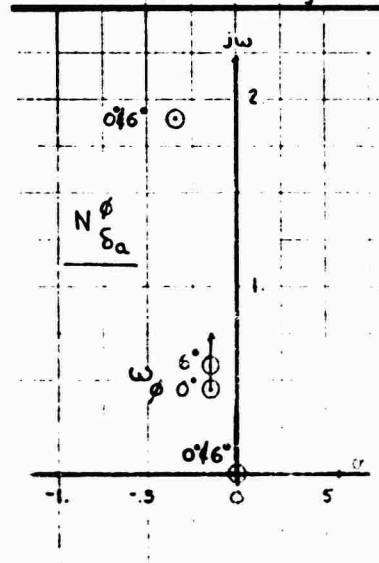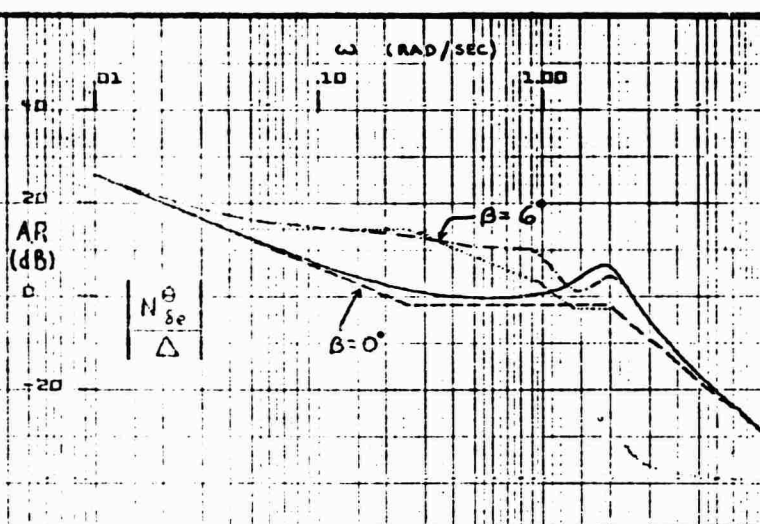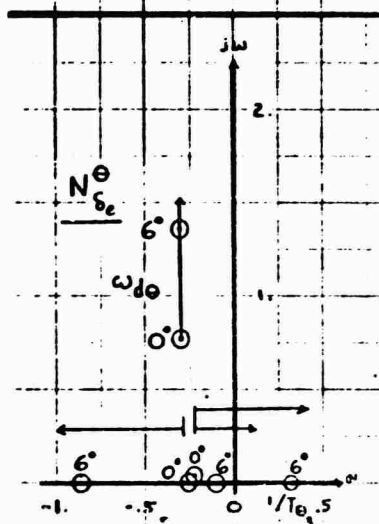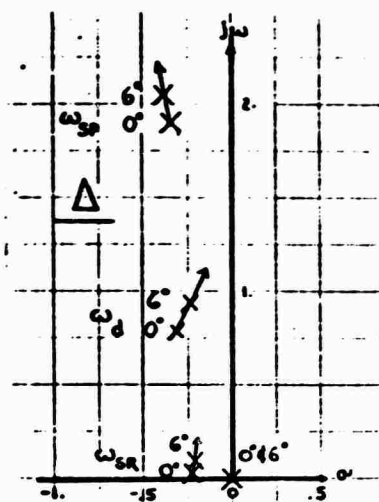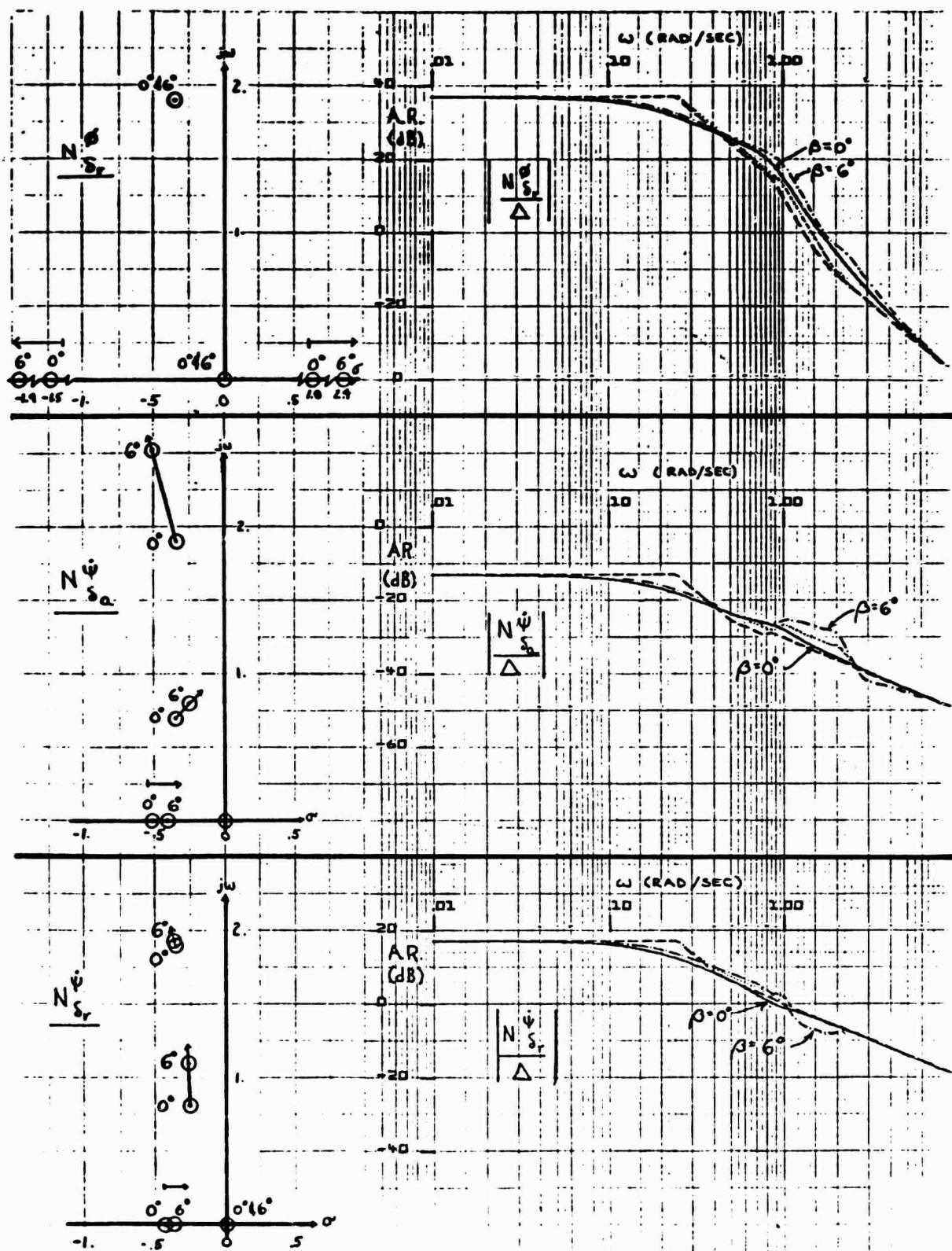
- The total absence of mid-frequency zeros and the presence of a right half plane zero in $N_{\delta_r}^{\eta}$ result in large low- and mid-frequency phase lag and make this control technique impractical.

- The migration of the high-frequency zeros of $N_{\delta_a}^{\dot{\psi}}$ increases separation from the short period poles and thereby indicates increasing excitation of the longitudinal mode if the pilot attempts to control $\dot{\psi}$ with aileron.

- The movement of the mid-frequency zeros of $N_{\delta_r}^{\dot{\psi}}$ to stay close to the dutch roll poles indicates little effectiveness of the rudder in damping dutch roll; however, the transfer function remains K/s-like and provides relatively good low-frequency control of yaw without pilot compensation.

Figure 30 presents open-loop pole-zero locations for fixed β_0 = 3 deg and trim α_0 of 19, 20, and 21 deg.[*] The lateral phugoid, ω_{SR}, steadily decreases in damping as α is increased and moves into the right half plane at approximately 21 deg α. The dutch roll frequency steadily decreases and damping increases. The short period is unaffected by change in α because M_α does not vary in this specific α range and Z_α was not varied with α in this simulation. The migration of poles in Fig. 30 is generally representative of all nine test configurations.

The mid-frequency zeros of θ/δ_e are seen to consist of a complex pair which are associated with, and "track," the dutch roll poles as α is increased. This again is typical of all configurations and will not be discussed further. The other zeros of the pitch numerator include a first order at about 0.5 rad/sec which is relatively unaffected by changes in α, and two first-orders, one in the right half plane ($1/T_{\theta_3}$), which drive together, become complex, and move into the right half plane at approximately 20 deg α.

The roll numerator initially has two pairs of complex zeros. One is associated with the longitudinal short-period mode and essentially cancels that pole. The other is the conventional ω_φ. As angle of attack is increased this complex zero rapidly moves to the real axis where it splits into two real zeros, one of which moves into the right half plane at approximately 20 deg α. It should be recalled that ω_φ is the parameter sometimes referred to as the aileron control divergence parameter and is considered to indicate a tendency to lateral divergence when it becomes negative (i.e., one root in the right half plane).

_____

[*] The clean aircraft stalls at α = 21 deg and β = 0 deg.
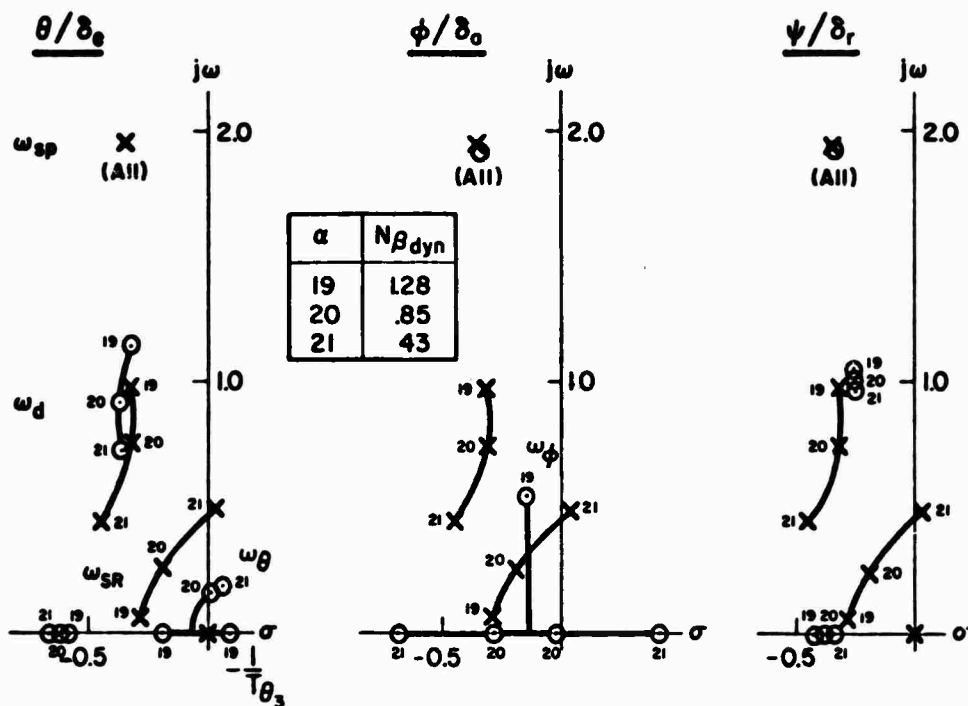
Figure 30. Configuration 1 Open-Loop Pole-Zero
Migration with α; $\beta_o = 3$ deg

The zeros of the yaw numerator consist of one real and two complex pairs. Again, one complex pair derives from the coupled longitudinal short period and essentially cancels the pole of this mode. The other complex pair is the conventional ω_r which lies near the dutch roll pole at 19 deg angle of attack and is relatively unaffected by the 2 deg change in α shown here. The real zero is the conventional $1/T_r$ which normally is of approximately the same value as the roll subsidence mode, $1/T_R$.

The box in the center of the figure presents the values of $N_{\beta_{dyn}}$ over this α range and shows that this parameter remains positive until even higher α is reached. A three-dimensional plot of $N_{\beta_{dyn}}$ versus α and β is shown in Fig. 31. This shows that if $\beta = 0$ then $N_{\beta_{dyn}}$ changes sign at approximately 21 deg α. However, the presence of a few degrees of sideslip will keep $N_{\beta_{dyn}}$ positive until well past stall α.

At this point the piloting technique generally employed should be discussed. First, in attempting to track and stay with the target as it ramped up, pitch attitude was the primary loop closure. As nose slice developed, the pilots

73
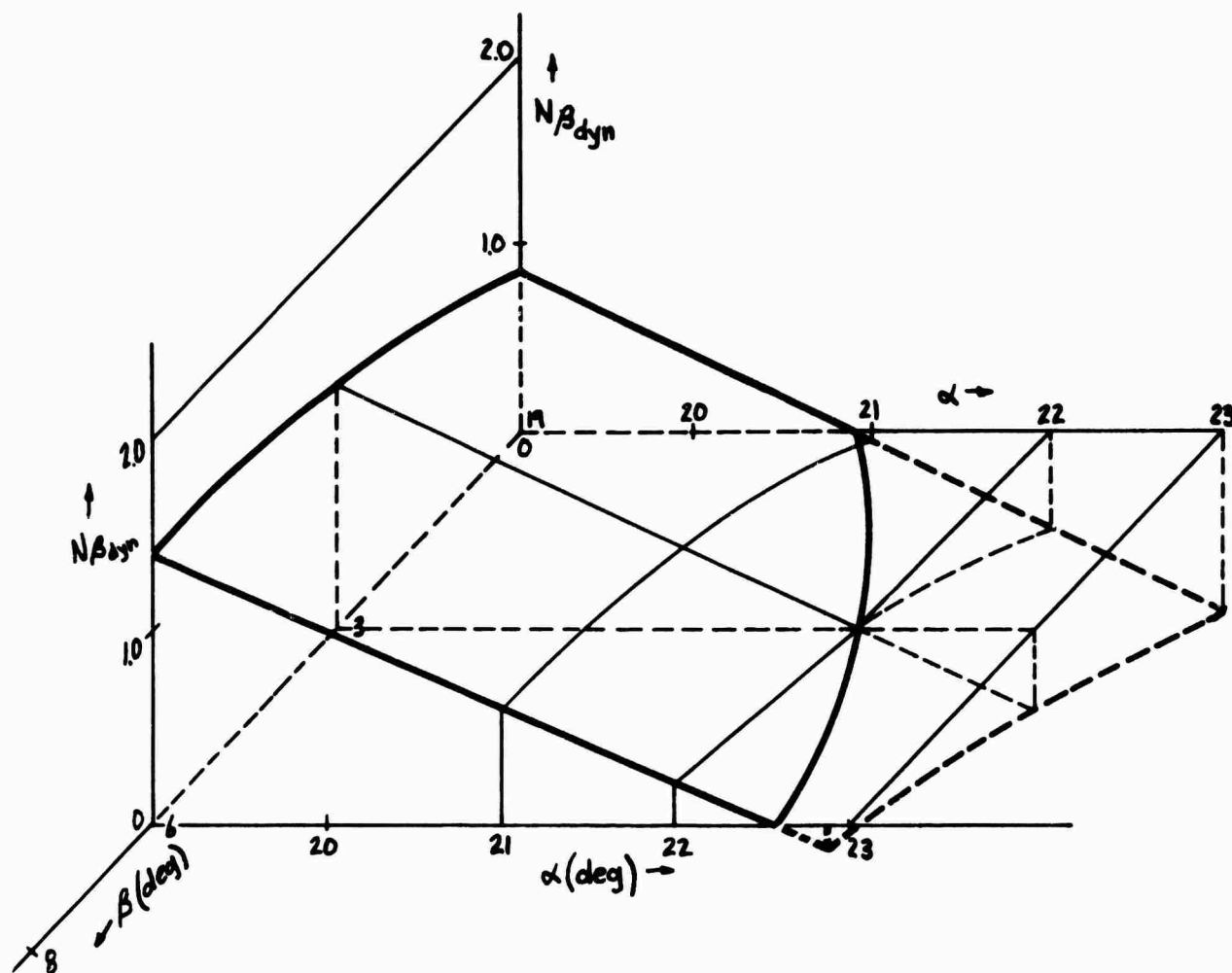
Figure 31.   Three-Dimensional Plot — $N_{\beta dyn}$ vs. α, β
(Configuration 1)

would either release all controls or tend to hold aileron, rudder, or both
for several seconds at a time against the motion of the initial slice. Thus,
the lateral controls were used more as gross moment producers to oppose air-
craft motion and did not reflect closed-loop activity in the usual sense.
When aileron or rudder was used in an attempt to speed recovery, pilot com-
mentary indicated a general problem in phasing either control to improve
recovery. Generally, the use of these controls increased sideslip and
degraded recovery. For example, Fig. 32 shows a "docile" recovery with a
complete lack of aileron or rudder activity in both departure and recovery.
Figure 33a indicates how use of rudder and aileron can aggravate recovery
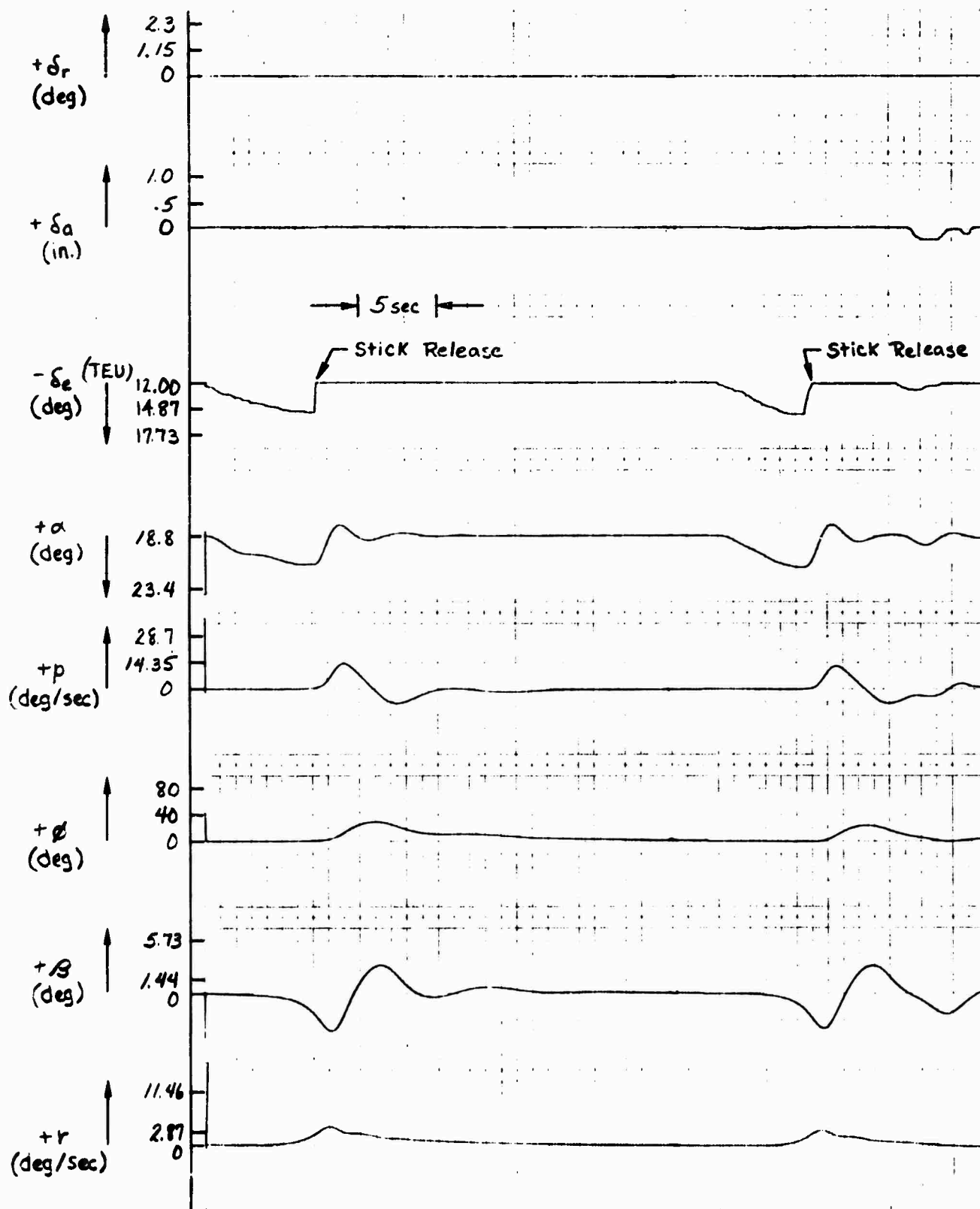
Figure 32. Configuration 1 Departure/Recovery with All Controls Released
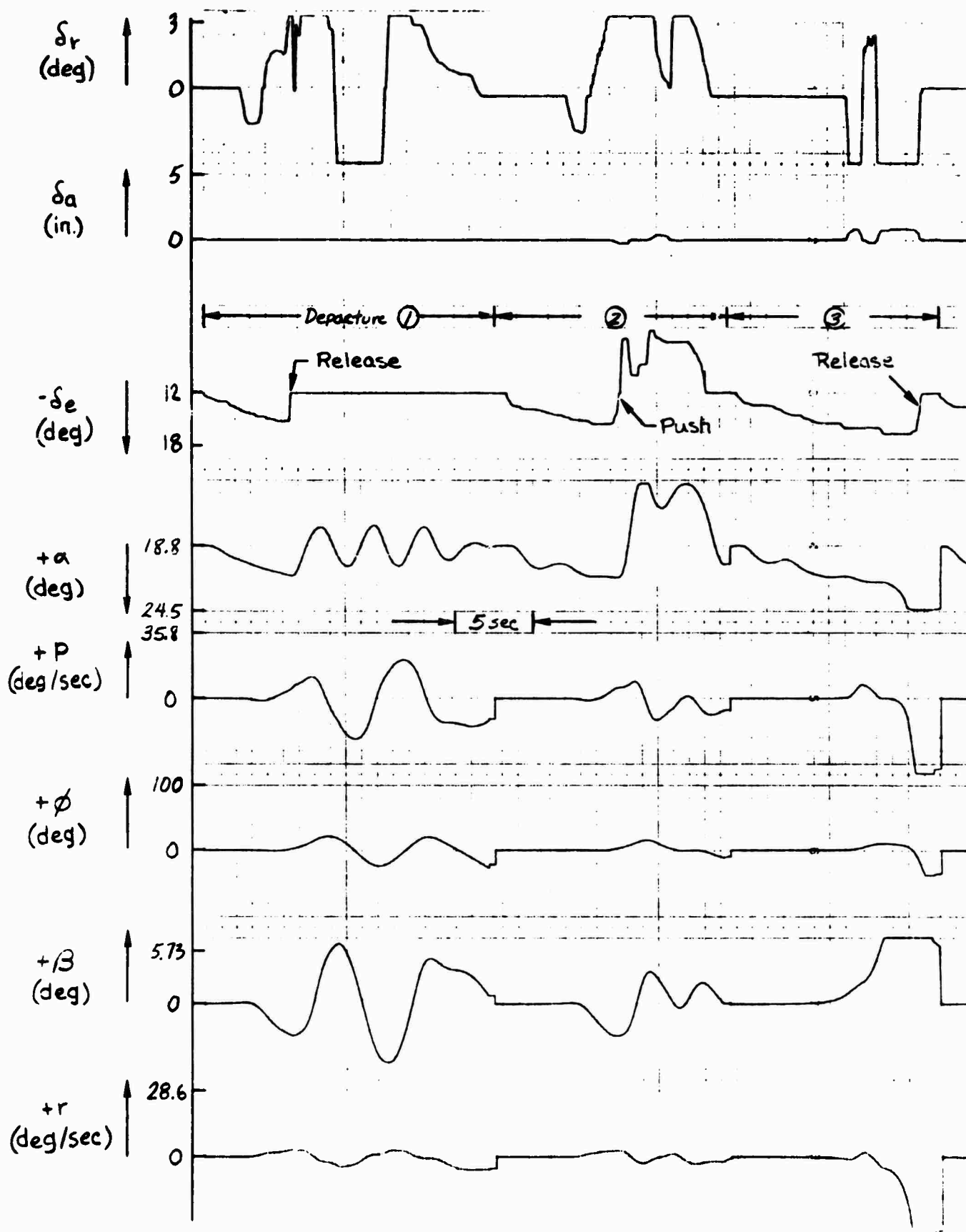
Figure 77a. Configuration 1 Departure/Recovery with Aileron and Rudder
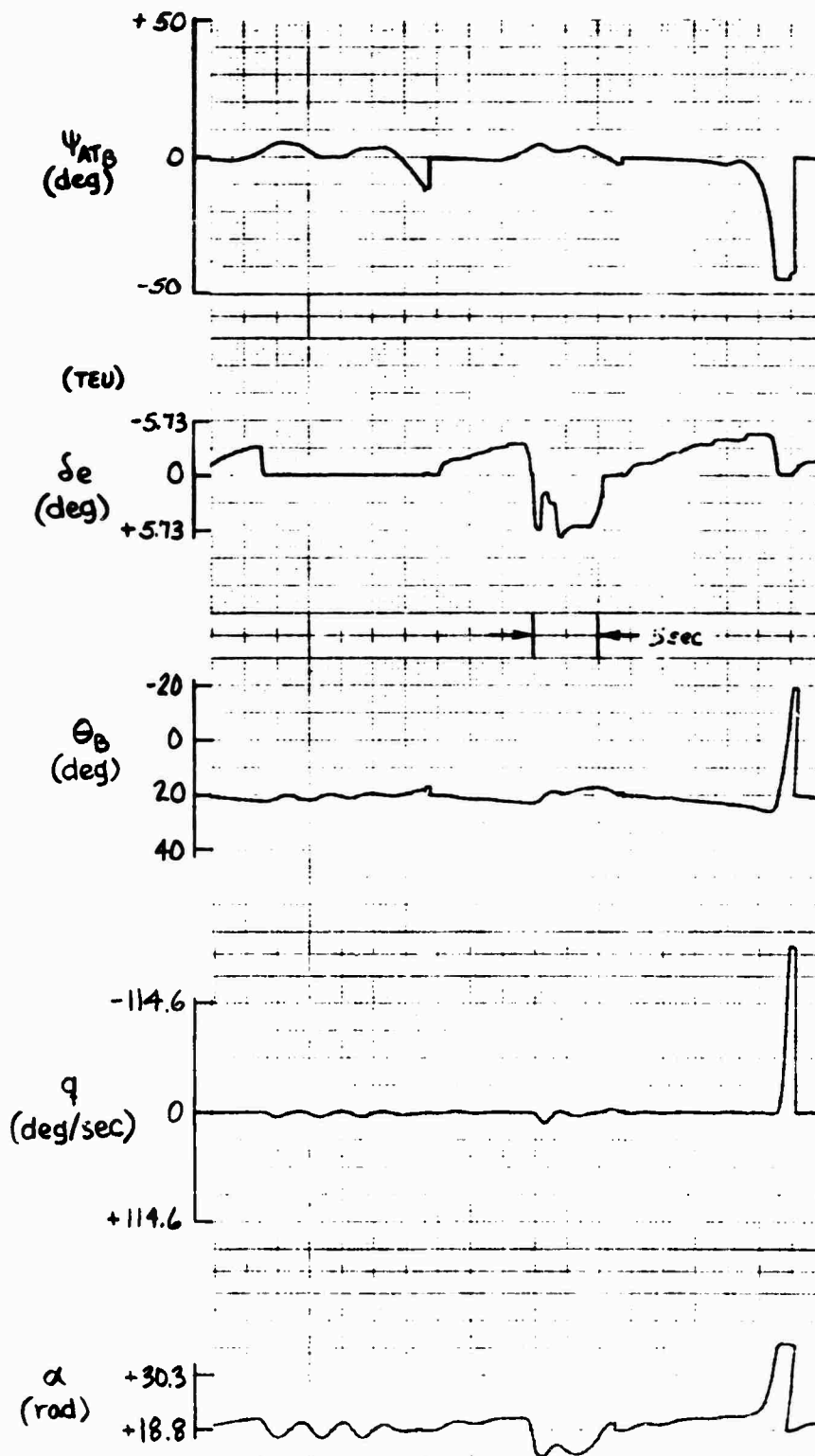
Figure 77b

and also the extended time periods full control deflection is used. Three departure and two recoveries are shown in these traces. Departure ③ was not recoverable. In Departure ① attempted control by rudder greatly excited sideslip (note β and r scale changes between Figs. 32 and 33) but did not change the maximum α that could be achieved before recovery had to be initiated. In Departure ② the rudder was rapidly bottomed and held. Recovery was achieved with stick push (to $\alpha \doteq 13$ deg) and full rudder. In Departure ③ the pilot attempted to track to higher α and possibly was a little late in applying corrective rudder. A small amount of aileron was also applied. At the time controls were released the sideslip exceeded 15 deg, yaw rate was greater than 60 rad/sec, and a pitch up (inertia coupling) was underway. Figure 33b presents pitch attitude and heading traces for these same three departures. These indicate that the successful recoveries had peak heading excursions of approximately 5 deg. The unsuccessful recovery was initiated when heading had changed about 20 deg. One second later the yaw was 50 deg.

Recovery with all controls released was rated a 4 (Cooper-Harper) by Pilot JS and 5 by Pilot ML. Use of aileron or rudder increased the average rating to 7 for JS and 9 for ML.

Pilot commentary and the strip charts indicate a "moderate" nose slice starts at $\alpha \leq 21$ deg and β between 1 and 5 deg. From Fig. 30 there are two possible parameters associated with the nose slice. One is the longitudinal complex zero, ω_θ. The other is the roll complex zero, ω_φ. Both result in right half plane zeros at approximately 20 deg α. On the basis of likely loop closures it would appear that the pitch zero, ω_θ, is the controlling parameter. With the pitch-to-elevator loop closed sufficiently tight to control the short-period attitude the lateral-phugoid complex pole is driven into the complex zero which moves into the right half plane at $\alpha \doteq 20$ deg. Thus, the departure should be expected to start at that angle of attack.

As a further aid in understanding the mechanics of the nose slice, closed-loop modal response vectors for the three dynamic modes (lateral-phugoid, ω'_{SR}; dutch roll, ω'_d; and short period, ω'_{sp}) are shown in Fig. 34 for unity gain pitch attitude closure and 21 deg α. This shows that the divergent ω'_{SR} mode (the closed-loop pole that is driven into the right half plane complex zero, ω'_θ)
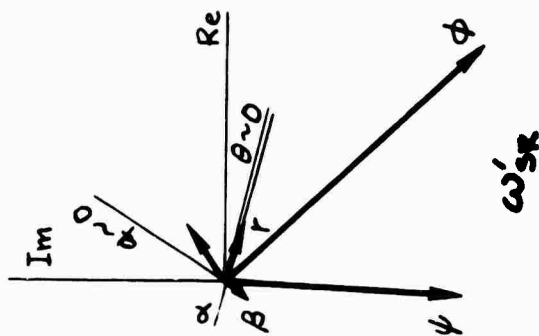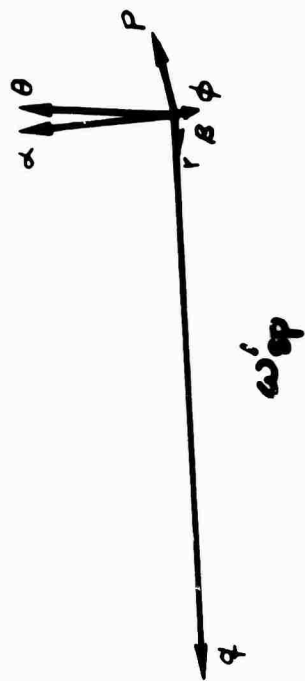
$$\left|\frac{\phi}{\psi}\right| = 6.35; \left|\frac{\phi}{\beta}\right| = 4.8$$

$$\left|\frac{\phi}{\psi}\right| = 23.25$$

$$\left|\frac{\phi}{\psi}\right| = 1.45; \left|\frac{\phi}{\beta}\right| = 23.25$$
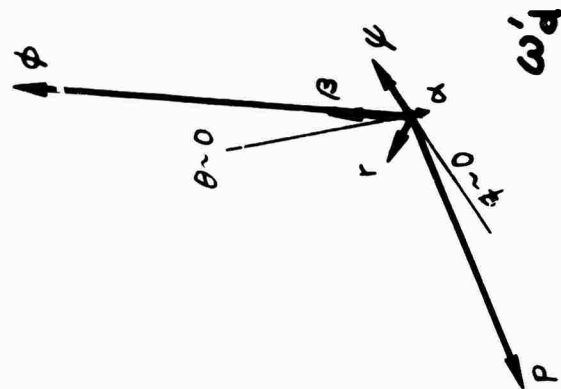
Figure 34. Closed Loop Modal Response Vectors for $\theta \longrightarrow \delta_e$ at $\alpha_0 = 21$ deg, $\delta_0 = 3$ deg

is primarily a roll-yaw motion (φ/ψ = 1.45) in which yaw leads roll by approximately 30 deg (positive rotation is counterclockwise). Although the response ratio indicates roll is greater than yaw, in the simulation heading displacement should be more apparent to the pilot than bank angle because a change in heading of, say, 5 deg is approximately equal to a semi-span of the target aircraft. With roll lagging yaw, a bank angle deviation of 5 deg would not be as apparent because of the lack of a direct reference. Thus, the closed-loop modal response coefficients further support ω_θ as the parameter dominant in setting nose slice characteristics.

Since the preferred recovery is completely open-loop, modal response vectors for the 19 deg α trim condition are presented in Fig. 35. If recovery is initiated (controls released) before large angular rates develop, inertia coupling will be small and the aircraft will return to this trim condition with small sideslip. The plots show that the lateral-phugoid, ω_{SR}, is again mainly roll and yaw ($|\varphi/\psi|$ = 5.44, $|\varphi/\beta|$ = 22.3) in which the roll lags yaw by approximately 140 deg. Thus, open loop, this mode has considerably greater rolling motion than closed loop; and the lag between ψ and φ might create the control phasing problem referred to by the pilots. With these two motions 140 deg out of phase the motion would be characterized by, say, left yaw and right bank. This certainly would lead to difficulty in arresting both φ and ψ with control deflections which do not further excite sideslip (i.e., without cross-control).

The open-loop dutch roll mode, ω_d, is mainly roll and sideslip with $|\varphi/\beta|$ = 3.37 but, interestingly, $|q/\beta|$ = 0.236 is greater than $|r/\beta|$ = 0.083. Thus, there is more pitch rate than yaw rate in the dutch roll mode. The longitudinal short period, ω_{sp}, on the other hand, is primarily a pitch and roll motion with φ/β = 0.88 which is approximately equal to the θ/α ratio. Also, p/α = 1.71. Thus, the greatest longitudinal-lateral coupling is in the open-loop short-period mode.

In summary, the α at which Configuration 1 nose slice occurs is consistent with movement of the pitch numerator zero, ω_θ, into the right half plane. The closed-loop modal response ratio evaluated at this zero indicates the motion to be primarily roll-yaw in which the yaw would be more apparent in a target tracking task. The parameter $N_{\beta_{dyn}}$ could also be associated with nose slice

Figure 22. Open Loop Modal Response Vectors at α_0 = 19 deg, δ_0 = 3 deg

ω_{sp}

$\left|\dfrac{\phi}{\theta}\right| = .88 \doteq \dfrac{\theta}{\alpha}$

$\left|\dfrac{P}{\alpha}\right| = 1.71$

ω_d

$\left|\dfrac{\phi}{\beta}\right| = 3.37$

ω_{SR}

$\left|\dfrac{\phi}{\psi}\right| = 5.44$

$\left|\dfrac{\phi}{\beta}\right| = 23.3$
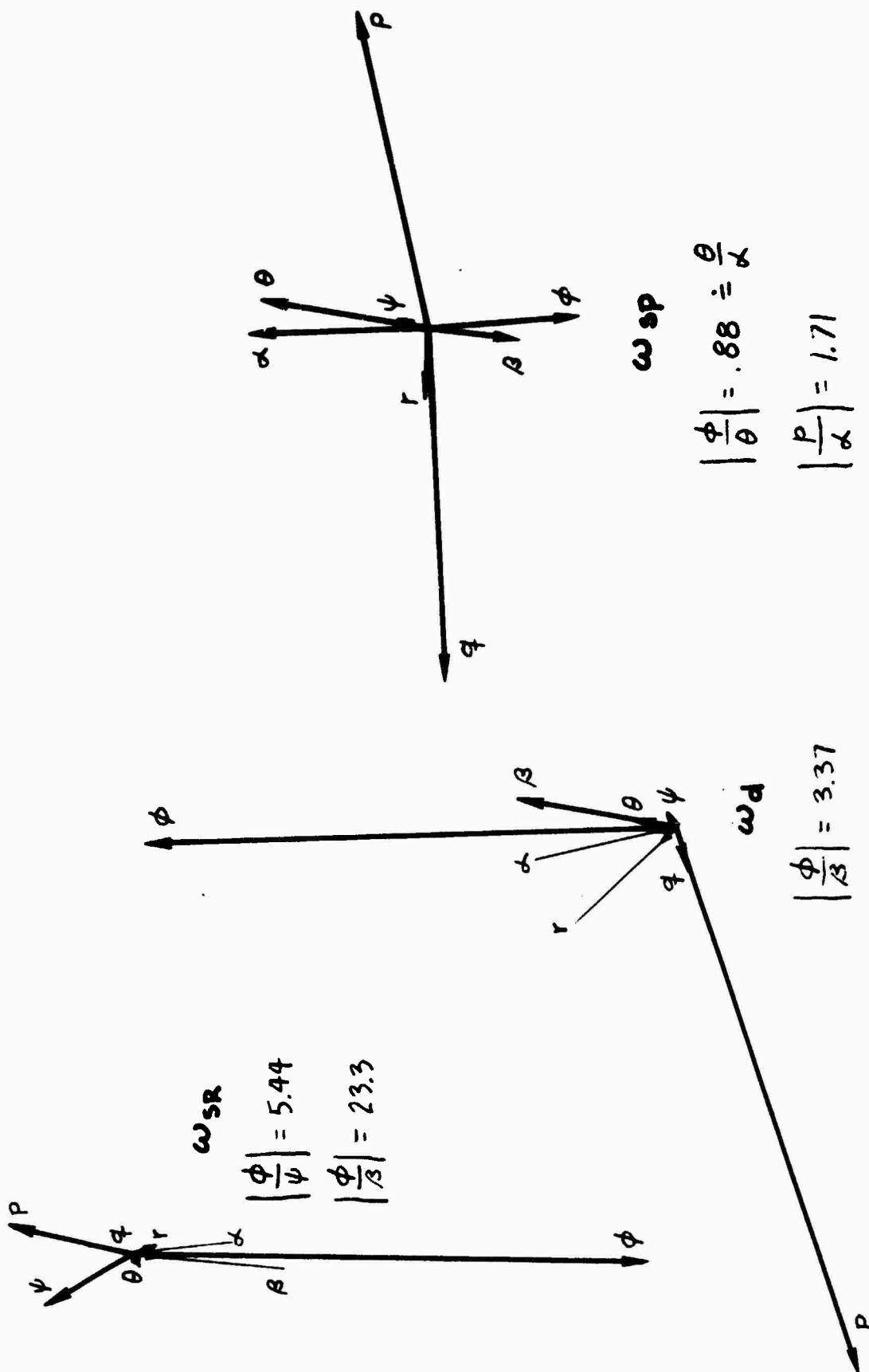
initiated at or slightly greater than 20 deg α providing the sideslip remained very near zero. However, $N_{\beta_{dyn}}$ is not consistent with instability when $\beta > 3$ deg and $\alpha < 22$ deg as was encountered in this simulation. The preferred recovery was achieved by release of all controls up to $\alpha = 21.3$ deg and $\beta = 3$ deg, providing angular rates were not so high at release as to induce inertia coupling into pitch. The open-loop modal response ratio of the lateral-phugoid is consistent with and would tend to predict the phasing problems encountered in the use of the aileron and rudder during recovery. If the pilot attempted to maintain the pitch attitude at that angle at which nose slice started, lateral-directional control could not be maintained and severe departure resulted.

2. Configuration 2

Figure 36 presents the open-loop pole-zero survey for Configuration 2. In this configuration $1/T_{\theta_3}$ is, initially, deeper into the right half plane and ω_φ/ω_d is unity. $N_{\beta_{dyn}}$ has the same range of values as in Configuration 1. The values of ω_φ remain positive and in the left half plane throughout an angle of attack range exceeding 21 deg. Movement of the lateral-phugoid is relatively slight between 19 and 20 deg α but rapidly moves into the right half plane by 21 deg α. The two lower-frequency zeros of the θ/δ_e numerator
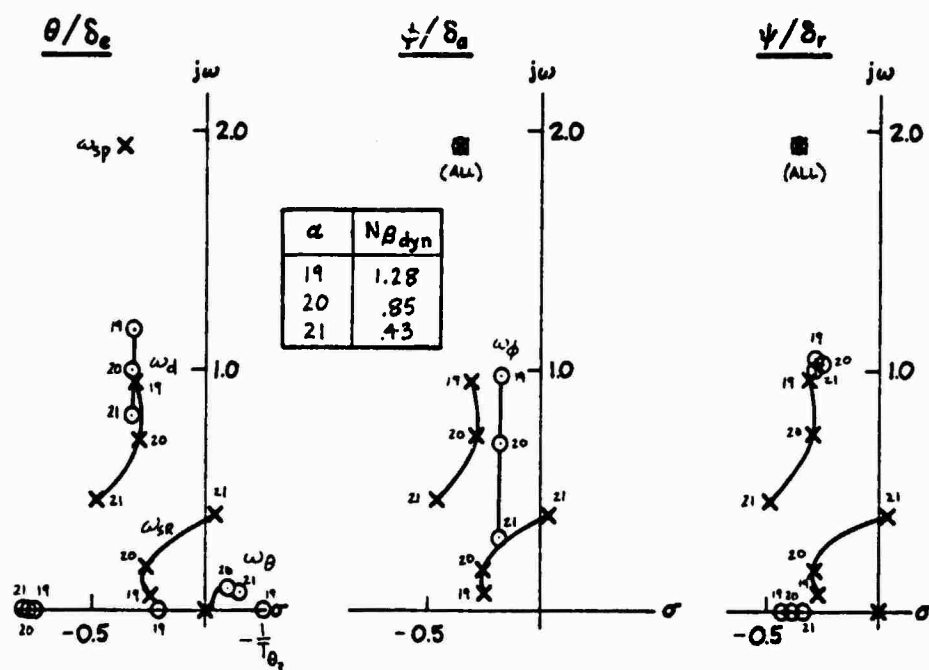
Figure 36. Configuration 2 Open-Loop Pole-Zero Migration; $\beta_o = 3$ deg

come together in the right half plane and the resulting complex zeros remain in the right half plane at all times.

The pilot commented that this configuration departs quickly starting at $\alpha \leq 21$ deg and the slice speeds as β builds. This configuration also would recover if the controls were released prior to $\alpha = 21.3$ deg and β 2 to 3 deg. It did not recover if the sideslip was allowed to build to the order of 5 deg. Problems were again encountered in coordinating use of aileron or rudder and, in general, they aggravated recovery. Recovery with release of all controls yielded a rating of 4 by JS and 7 by ML.

It may be noted from Fig. 36 that both ω_φ and $N_{\beta_{dyn}}$ remain positive at the α and β values where departure was obtained. Again, only the pitch parameter, ω_θ, correlates with the departure conditions.

3. Configuration 3

For this configuration the lateral-phugoid was changed into the more conventional spiral and roll subsidence modes with $1/T_R = 0.46$; $N_{\beta_{dyn}}$ was increased to 1.58; $1/T_{\theta_3}$ remained at approximately the same value as in Configuration 2; and ω_φ/ω_d was returned to the base (Configuration 1) A-7 value.

The open-loop pole-zero migrations with α are shown in Fig. 37. The major difference between this and the previous case is that the lateral-phugoid, which results from a rejoining of the spiral and roll subsidence at about 20 deg α, remains well in the left half plane at 21 deg α.

Pilot commentary indicated this configuration exhibited a "mild" slice characteristic which could be controlled to approximately 20 deg α but departed for $\alpha > 20$ deg. Recovery could be achieved by releasing all controls up to 22 deg α and 5 deg β and, with stick push forward of neutral, to 20 deg α and 13 deg β. Use of lateral control would rapidly build sideslip; and this configuration generally exhibited larger sideslips than the previous case. Both pilots rated the departure/recovery a 3 for release of all controls. Stick push recovery after development of large sideslip was rated a 7.

Again for Configuration 3 both lateral parameters ω_φ and $N_{\beta_{dyn}}$ remained positive (with comfortable margin) and the open-loop lateral-phugoid remained
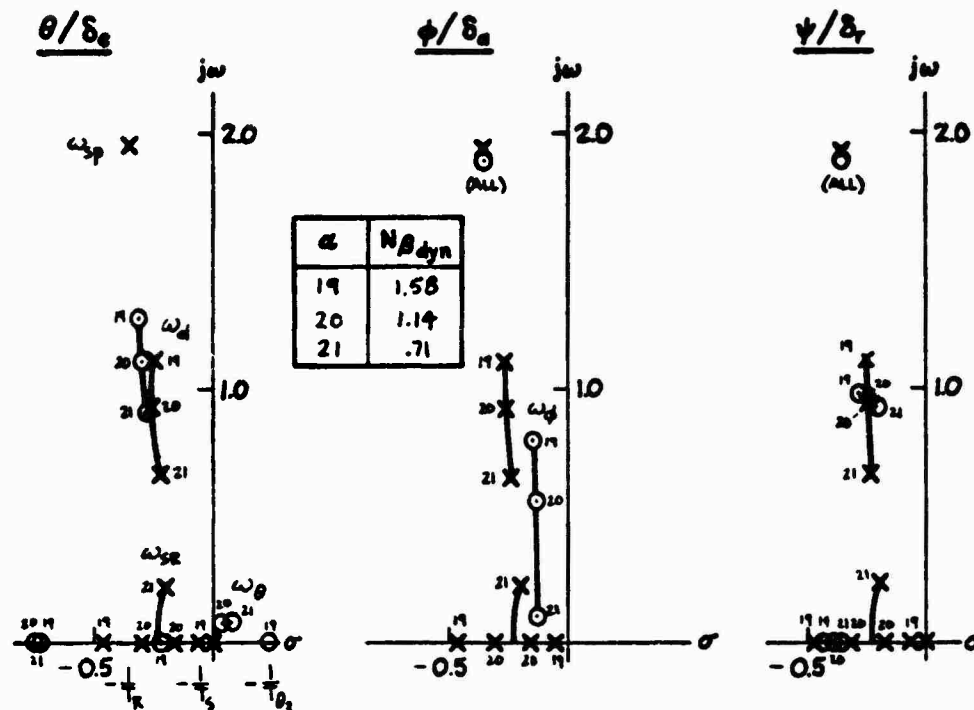
Figure 37. Configuration 3 Open-Loop Pole-Zero
Migration; $\beta_O = 3$ deg

stable at the angle of attack at which nose slice was exhibited. Only ω_θ
lies in the right half plane and provides a good indication of closed-loop
divergence tendencies.

4. **Configuration 4**

This configuration was intended to provide docile handling at high angle
of attack. To accomplish this the open-loop parameter $1/T_{\theta_3}$ was moved to the
left half plane and ω_p/ω_d was set to unity. The survey plots are presented
in Fig. 38. As with the basic (Configuration 1) A-7, the lateral-phugoid
steadily moves toward and into the right half plane at approximately 21 deg α.
The two low-frequency, real zeros of the pitch numerator couple at between
19-20 deg α and again move into the right half plane at between 20-21 deg α.
The aileron zero, ω_φ, remains in the left half plane and $N_{\beta_{dyn}}$ remains posi-
tive throughout this α range.

Pilot commentary indicated a "slow" rate of nose slice was obtained at
about 21 deg α but in this instance the pilot could hold up to 23 deg α for

84
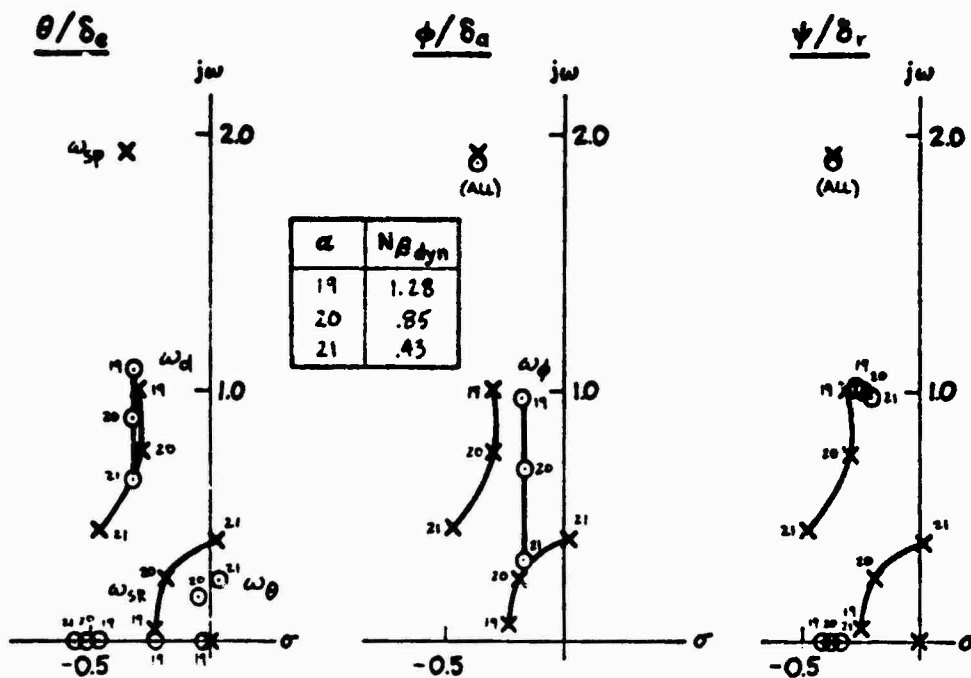
Figure 38. Configuration 4 Open-Loop Pole-Zero
Migration; $\beta_0 = 3$ deg

several seconds while using lateral control to contain the divergent nose wander within acceptable bounds (see Fig. 39). This often could be accomplished without exciting "large" sideslip and recovery could be achieved by merely releasing all control. This configuration was considered very docile (as planned) unless the pilot induced large sideslip while attempting to maintain control at the high angle of attack. Again, both pilots rated this a Cooper-Harper of 3 for recovery involving only release of controls. If lateral control were employed following longitudinal stick release, problems were again encountered in phasing the lateral control to improve recovery and ratings suffered (average of 7 to 8).

The nose slice again correlates with ω_θ moving into the right half plane. It is particularly interesting though that this configuration could be flown for several seconds at angles of attack at or above 22 deg α since this should result in a closed-loop instability as in the previous cases, especially since $N_{\beta dyn}$ and ω_D also approach negative values. An explanation for this relatively
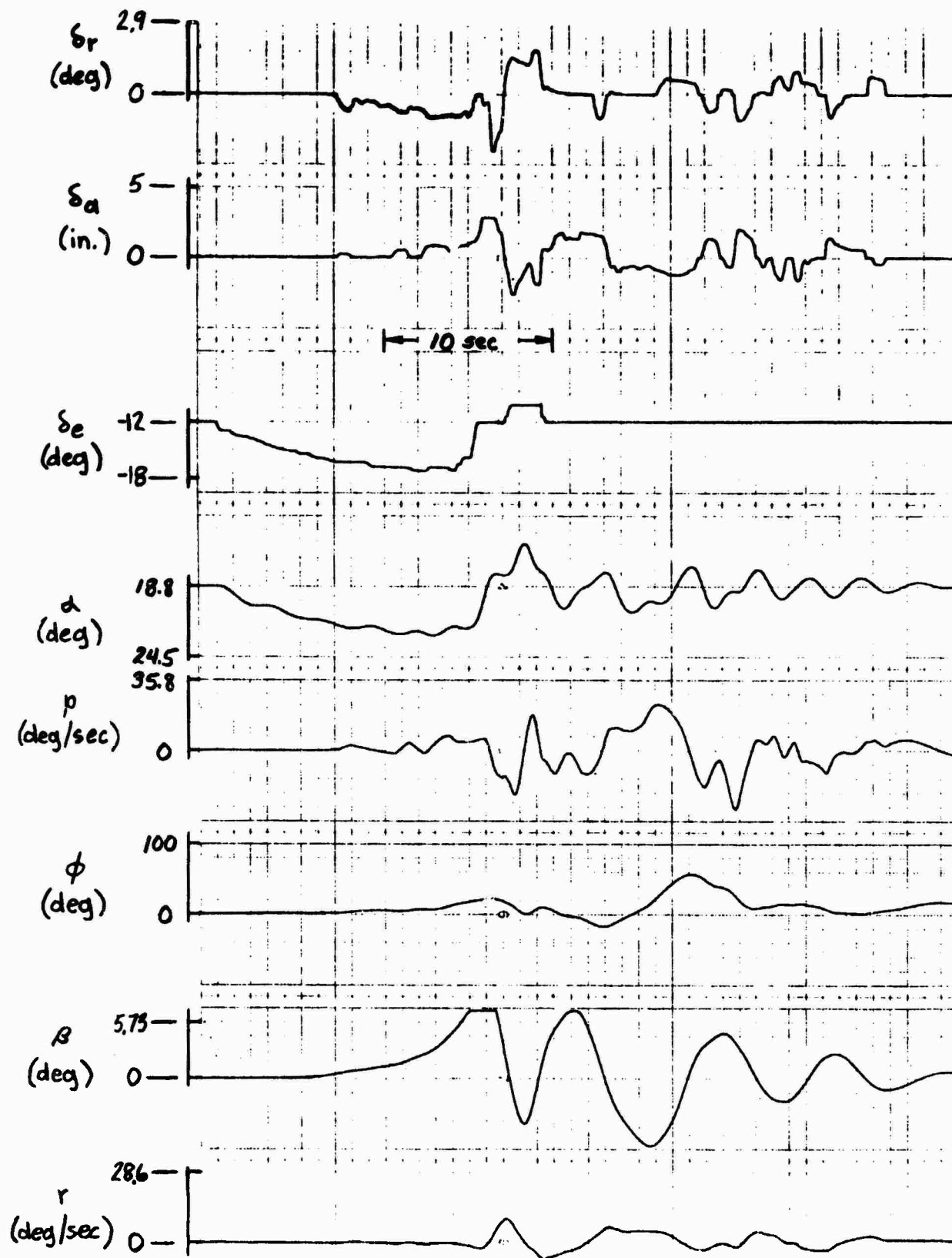
Figure 39. Configuration 4 Departure and Rating

docile, semi-controllable behavior at higher angles of attack is that the initial magnitude and slope (with β) of N_C are reduced by a factor of 5 (from -1.6 to -0.3 at $\beta = 3$ deg) in order to move $1/T_{\theta_3}$ into the left half plane. Thus, there is a significant reduction in longitudinal to directional coupling. This then requires less lateral control activity and hence produces less sideslip excitation. Departure is delayed but not prevented.

5. Configuration 5

The survey plot for Configuration 5 is presented in Fig. 40. Again, $1/T_{\theta_3}$ is in the right half plane. The principal change from Configuration 4 is an increase in $\mathcal{L}'_\beta$ which, among other effects, increases $N_{\beta_{dyn}}$. Aileron yaw, N_{δ_a}', was also returned to the nominal (Configuration 1) A-7 value; and these two changes resulted in $\omega_\phi/\omega_d = 0.534$, which should provide roll reversal tendencies. The increase in $\mathcal{L}'_\beta$ results in considerably less migration of all poles and zeros (except ω_ϕ) for the 2 deg α change shown here. The combination of positive $1/T_{\theta_3}$ and increased $\mathcal{L}'_\beta$ resulted in the most stable configuration of those investigated (no poles or zeros in the right half plane at stall) and

α	$N_{\beta_{dyn}}$
19	1.77
20	1.4
21	.98
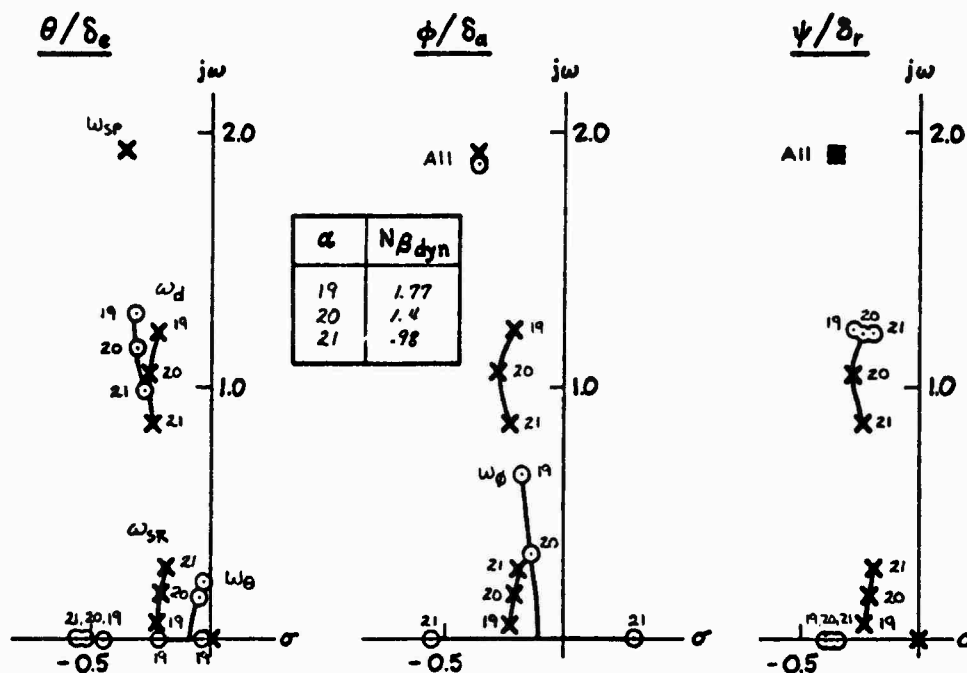
Figure 40. Configuration 5 Open-Loop Pole-Zero Migration

87

also provided the least change in vehicle dynamics as stall is approached. Both ω_{SR} and ω_θ reflect a stable lateral-phugoid at stall (α = 21 deg). Although transfer function roots were not calculated for α's greater than stall, the α at which ω_θ reaches the right half plane may be estimated by comparing the root movements for Configurations 4, 5, and 6. The only significant difference in these configurations is a change in $\mathcal{L}_\beta$.

Configuration 6: $\mathcal{L}'_\beta$ = -1.75 , α_{ω_θ} = 19.5-20 deg (Fig. 42)

Configuration 4: $\mathcal{L}'_\beta$ = -4 , α_{ω_θ} = 20.5-21 deg (Fig. 38)

Configuration 5: $\mathcal{L}'_\beta$ = -5.55

By comparison, it would be expected α_{ω_θ} (the α at which ω_θ crosses into right half plane) for Configuration 5 to be about 21.5 to 22 deg.

Pilot commentary indicates this configuration is still under control at 21 deg α and slow nose slice is not encountered until approximately 22.5 to 23 deg α. It could be taken to 23 deg α and 6 deg β or more and still recovered with only release of controls. One pilot rated this a 4; the other pilot rated it a 3. There were completely different opinions regarding the effectiveness and usefulness of aileron and rudder. One pilot thought the rudder effective while aileron was not; the other had the reverse opinion. However, both could maintain control quite well while at the elevated angles of attack. One pilot commented that he had so much confidence at the higher α's that he would get into trouble by attempting to track too far into the stall region (see Fig. 41). He also considered the departure warning to be inadequate. It was difficult for either pilot to decide when to "give up" and attempt recovery because lateral-directional control remained quite effective. However, sideslip would often continue to build up until finally a severe departure would result (e.g., the second stall in Fig. 41). Because there was a tendency to go too far, both pilots downgraded the departure/recovery rating.

In summary, this configuration proved to be the most stable and difficult to depart, as planned, but proved surprising in that the warning was considered inadequate. The important aspect remains, however, that the presence (or lack
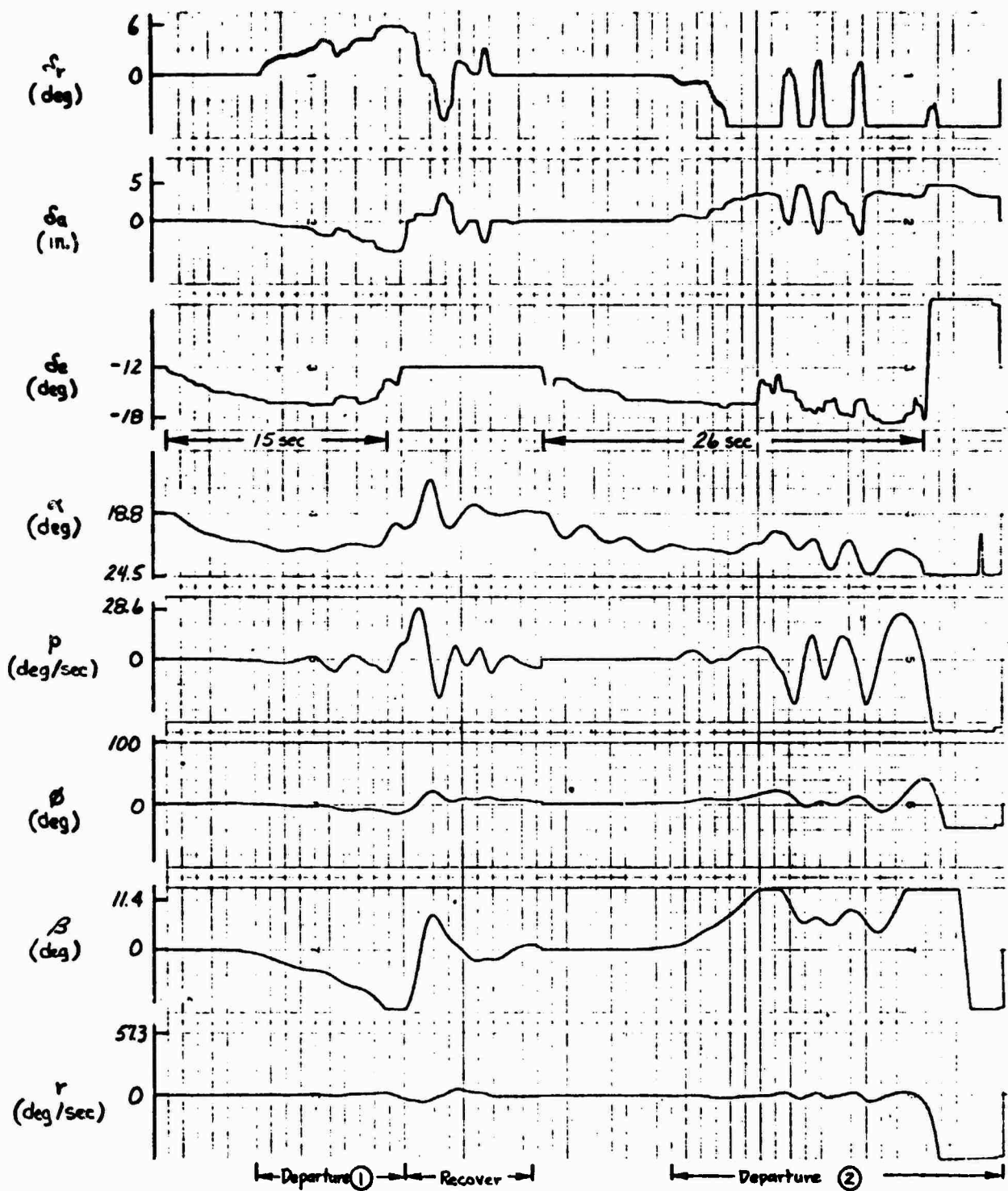
Figure 41. Configuration 5 Departure Characteristics

of) nose slice at a given α is consistent with the location of the complex zero ω_θ and that this configuration which was selected to provide the best high α characteristics did indeed prove the most difficult to obtain departure.

6. Configuration 6 and 7

The survey plots representing both Configurations 6 and 7 are presented in Fig. 42. The change from Configuration 5 to Configuration 6 is accomplished by changing one derivative, $\mathcal{L}'_\beta$, from −5.55 to −1.75. Configuration 7 differs from Configuration 6 in that the coupling derivative, $\mathcal{L}'_\alpha$, is reduced from 1.55 to 0.75 for Configuration 7 to determine whether this influences the roll characteristics of the departure. It did not produce a significant difference in departure/recovery characteristics or the pole-zero locations shown in Fig. 42. These initially correspond to a stable $1/T_{\theta_3}$, $\omega_\varphi/\omega_d = 0.63$, low-frequency lateral characteristics separated into a spiral and roll
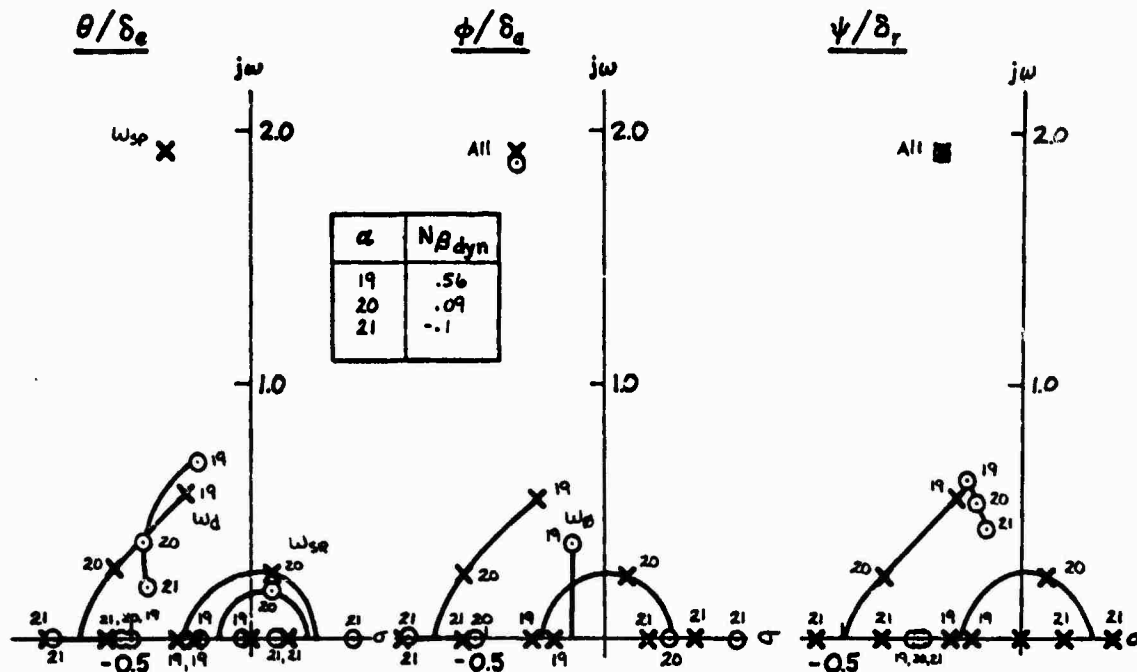
Figure 42. Configurations 6 and 7 Open-Loop Pole-Zero Migration

subsidence, and an initial $N_{\beta dyn} = 0.56$ which becomes negative at approximately 20.5 deg α. Increasing angle of attack results in relatively large pole-zero migrations from these initial values. The roll subsidence/spiral rapidly couple, pass into the right half plane at 20 deg α, and produce two first-order divergence modes (RHP) by 21 deg α. The dutch roll mode damping increases, becomes critically damped at approximately 21 deg α, and separates into two first-order stable poles. The low-frequency zeros of $N^{\theta}_{\delta_e}$ track almost precisely with the roll subsidence/spiral poles and thus produce a complex right half plane pair by 20 deg α. In the roll numerator, ω_φ moves to the real axis and produces a first-order right half plane zero at approximately 19.5 deg α and this zero moves further into the right half plane as α increases. Only the yaw zeros remain in the left half plane.

This configuration produced a very flat-appearing yaw departure at α greater than 20 deg, accompanied by a very large and rapid buildup of sideslip. One recovery was obtained from 21.3 deg α and 4.7 deg β; however, recovery was, in general, not achieved unless back stick was released upon first detection of nose slice. Following release of back stick, one pilot thought aileron improved recovery. Use of rudder in recovery was considered difficult. One pilot rated control-free recovery a 4 while the other rated it between a 7 and 9. The major difference appeared to lie in how rapidly the pilot initiated recovery once the nose slice started.

The more positive and rapid departure obtained with this configuration was apparently related to the almost simultaneous achievement of negative values with the three parameters ω_θ, ω_φ, and $N_{\beta dyn}$.

7. Configuration 8

The survey plots for Configuration 8 are shown in Fig. 43. In this case an initial condition of $N_{\beta dyn} = 0$ was achieved by retaining the low $\mathcal{L}'_\beta$ (Configurations 6 and 7) and setting $N'_\beta = -0.5$. This results in an initial trimmed condition where the lateral-phugoid mode is unstable. Further increase in α results in two first-order divergences, one of which is very rapid. Both the pitch and roll numerators also start with zeros in the right half plane; thus, neither loop closure will stabilize the divergence. As would be expected, this configuration produced immediate divergence which

91
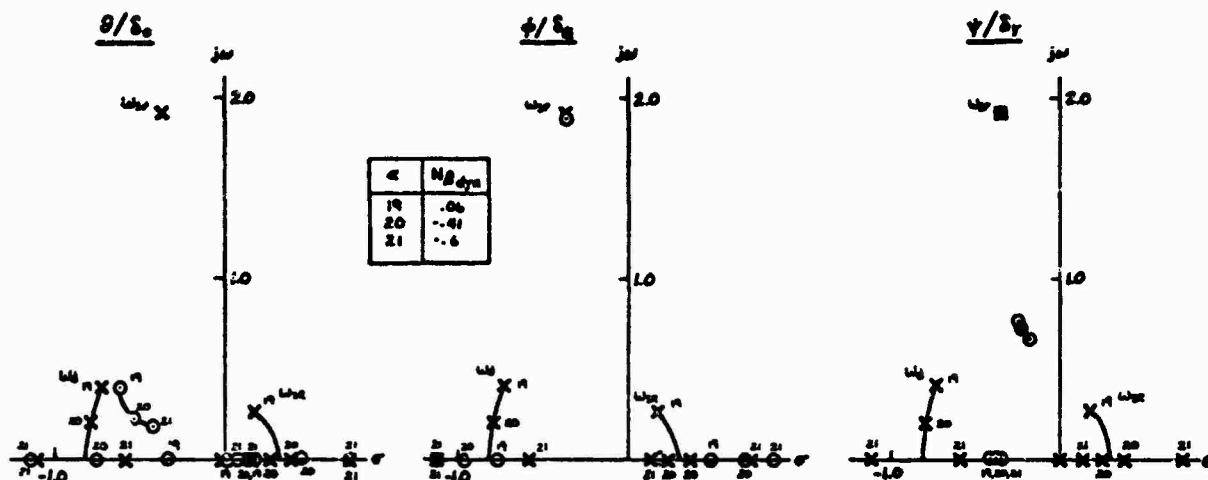
Figure 43. Configuration 8 Open-Loop Pole-Zero Migration

could not be arrested by use of control unless longitudinal stick was pushed
and held forward of neutral until recovery. This reduced the angle of attack
below 19 deg and returned the lateral-phugoid mode to left-half-plane sta-
bility. Very little could be done with this configuration, and recovery had
to be initiated upon the first indication of the nose slice. The use of
lateral-directional control made this configuration essentially unrecoverable.
While it could be recovered maintaining forward longitudinal stick, this did
require more effort and concentration on the part of the pilot and therefore
degraded the recovery rating to a 6 or 7 for both pilots.

8. Configuration 9

The final configuration, shown in Fig. 44, offered improved initial low-
frequency lateral dynamics ($1/T_{R_O} = 0.53$; $1/T_{S_O} = 0.03$) but decreased dutch
roll damping ($\zeta_{d_O} = 0.034$) over that of the basic A-7. This was accomplished
by increasing N'_β and making the term ($N'_p - g/U_O$) negative (i.e., decreasing
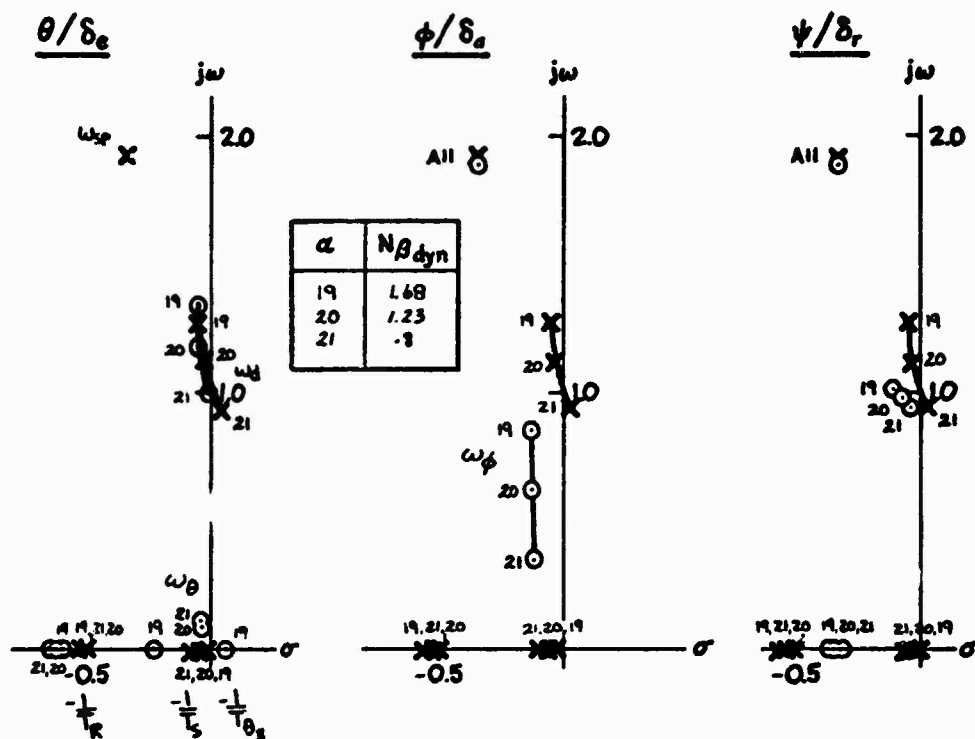
Figure 44. Configuration 3 Open-Loop Pole-Zero Migration

N'_p, the total yaw due to roll rate). N'_α is returned to its initial (Configuration 1) value; therefore, $1/T_{\theta_3}$ is negative.

The principal effect of an open-loop increase in α is to cause the dutch roll to diverge. Movement of all other poles is relatively small. The low-frequency zeros of $N^\theta_{\delta_e}$ couple into the complex ω_θ which remains in the left half plane at 21 deg α but would appear likely to move to the right half plane shortly thereafter. The complex zeros, ω_ϕ, remain in the left half plane and move toward the real axis. In pitch and yaw, the dutch roll complex pole-zero pairs essentially cancel so there is little evidence of the dutch roll in these motions. The dutch roll is therefore primarily a roll motion. If the pilot attempts to control or damp dutch roll with ailerons at the higher α's we would expect the closed-loop root migration to be as shown in the following sketch. Here the roll subsidence and spiral drive into ω_ϕ while ω_d moves to higher frequency. The closed-loop dutch roll also is further destabilized by the pilot's time delay and other high-frequency lags. Thus, this configuration might be expected to exhibit a wing rock tendency prior to nose slice.

93

$$\omega_d \qquad \omega_\phi \qquad -\frac{1}{T_R} \qquad -\frac{1}{T_s}$$
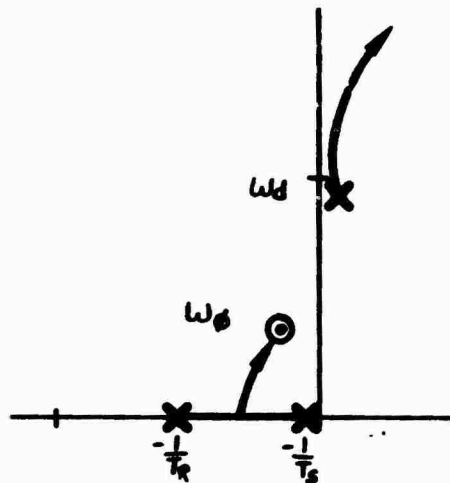
Pilot commentary and strip chart records indicate nose slice did start at about 22 deg α. One pilot described it as having a roll-off tendency before the departure angle of attack is reached. The other described it as a tendency to wing rock. Recovery was achieved by release of all controls at β up to ± 7 deg and $\alpha = 22$ deg. Use of any lateral control only aggravated the recovery. This configuration was rated a 3 for immediate release of all controls. If an attempt was made to damp the dutch roll motion during departure and recovery it was rated between 6 and 10, depending upon how aggressively the pilot opposed the roll motion.

9. Summary and Conclusions

It is concluded that the initial and final nose slice characteristics and pilot comments best relate to the parameters $1/T_{\theta_3}$ or ω_θ. The angle of attack at which departure occurs can be increased significantly by elimination of N'_α. The conventional lateral parameters, $N_{\beta_{dyn}}$ and ω_ϕ, certainly contribute to, but are not the key factors in, the A-7 nose slice. It appears that when these parameters become negative at the same time the longitudinal parameters are in the right half plane the rapidity and/or severity of nose slice departure is increased. It is also apparent that lateral-directional control is difficult to coordinate during the departure and/or recovery phases and generally aggravates rather than enhances recovery. If system dynamics and/or control characteristics do not change appreciably as α increases the masked departure onset can result in attempts to maintain control to higher α and, eventually, a more severe departure. One key to successful recovery

94

with minimal pilot workload or compensation is that the aircraft be trimmed, stick force zero, at an angle-of-attack for which the lateral-phugoid and dutch roll are stable. Therefore, the open-loop parameter $N_{\beta dyn}$ is a key factor in recovery. Finally, the results support the concept that wing rock is related to an unstable dutch roll which is further aggravated by pilot attempts at roll control.

C. EFFECT OF PILOT TECHNIQUE

The pilot ratings assigned to the different configurations, according to the Cooper-Harper handling quality rating scale of Fig. 45, varied widely with pilot technique (agressiveness, anti- versus pro-departure recovery control, stick release versus stick push recovery, etc.). In general any attempt at use of lateral-directional control to reduce departure excursions resulted in a significant increase in numerical rating. This was traced to several factors. First, there was a tendency to use less lateral-directional control in opposition to the initial departure motion if recovery was to be achieved via release of all controls. Conversely, if the task called for use of aileron or rudder during recovery, there was a strong tendency to significant use of this control in the pre-departure tracking task. Effective application of such control required significant pilot concentration (compensation) and hence degraded the rating. The application of lateral control to oppose the initial departure motion either allowed deeper stall penetration or increased sideslip — or both. This then resulted in a more violent initial nose slice and, quite often, a "secondary" departure due to roll-yaw inertia coupling into pitch.

As indicated previously, the pilots were requested to assess or evaluate two separate types of recovery. One might be called aggravated control recovery in which an attempt was made to hold the departure pitch attitude and maintain lateral-directional control of the aircraft. This was not sucessful in any of the cases and always resulted in a rating of 10. The second method was to release and/or push forward on the stick to reduce angle-of-attack. The latter technique was further categorized by specific use of lateral control following release of back stick. The pilot ratings obtained for the matrix of dynamic configurations and recovery techniques are given in Table 8: recovery A identifies release of longitudinal stick

Pilot Decisions	ADEQUACY FOR SELECTED TASK OR OPERATION	AIRCRAFT CHARACTERISTICS · DEMANDS ON THE PILOT IN SELECTED TASK OR REQUIRED OPERATION	PILOT RATING
Is it controllable? NO →	Improvement Mandatory	Major deficiencies - Control will be lost during some portion of required operation	10
YES ↓	Deficiencies require improvement	Major deficiencies - Intense pilot compensation is required to retain control	9
		Major deficiencies - Considerable pilot compensation is required for control	8
Is adequate performance attainable with a tolerable pilot workload? NO →		Major deficiencies · Adequate performance not attainable with maximum tolerable pilot compensation. Controllability not in question	7
YES ↓	Deficiencies warrant improvement	Very objectionable but tolerable deficiencies · Adequate performance requires extensive pilot compensation	6
Is it satisfactory without improvement? NO →		Moderately objectionable deficiencies · Adequate performance requires considerable pilot compensation	5
		Minor but annoying deficiencies · Desired performance requires moderate pilot compensation	4
YES ↓		Fair – Some mildly unpleasant deficiencies · Minimal pilot compensation required for desired performance	3
		Good Negligible deficiencies · Pilot compensation not a factor for desired performance	2
		Excellent Highly desirable · Pilot compensation not a factor for desired performance	1

Figure 45. The Cooper-Harper Handling Qualities Rating Scale

TABLE 8.   SUMMARY OF PILOT RATINGS FOR RECOVERY

CONFIG.	JS			ML	
	ROLL OUT	STICK PUSH	PILOT RATING	PILOT RATING	
				RELEASE	PUSH
1 A			4	6	5
B	Y		5	10	8
C			9	9	5
D			9	8	6
E	Y		4	9	9
2 A			4	7	−
B	?		6	8	7
C			9	9	8
D			10	6	5
E			8	10	7
3 A			3	3	−
B		Y	8	8	7
C	Y		6	9	7
D			10	7	6
E			3	8	5
4 A			3	3	−
B			9	5	6
C			6	9	9
D	Y		8	9	8
E			6	9	6
5 A			4	3	−
B	Y		6	10	4
C		Y	6	10	9
D	Y		6	10	9
E			6	4	6
6 A			4	8	−
B			9	5	6
C			8	9	6
D		Y	8	6	−
E		Y	8	9	−
7 A			4	9	7
B		Y	10	4	5
C		Y	8	10	8
D		Y	10	8	7
E		Y	8	10	7
8 A		Y	6	10	7
B			10	10	9
C			10	1C	7
D			10	10	8
E			10	10	9
9 A			3	10	6
B			6	9	8
C			8	9	8
D			10	8	7
E			6	6	5

Y = Successful recovery by 360 deg roll

97

only with no lateral-directional inputs following stick release, B is use of aileron only, C is rudder only, D is aileron and rudder, and E is rudder only but with $\mathcal{L}_{\delta_r}$ reduced by a factor of four. The latter resulted in very nearly pure yaw rudder for all configurations.

In addition to these scheduled variations in control technique there were several unplanned. One pilot was more aggressive in attempting to track the target to high α's before giving up and initiating recovery. (The pilot measurements reported in the following sections showed this pilot to be operating at the higher gain of the two.) This pilot also routinely used forward stick in evaluating various recovery techniques. The other pilot did not like to use forward stick and appeared to use this recovery technique only as a last resort. However, he routinely investigated application of controls with the direction of nose slice as well as control against. Control "with" sometimes proved quite successful in converting a nose slice departure into a controlled 360 deg roll maneuver.

Table 8 indicates the wide range in ratings achieved for the configurations and recovery techniques. The search for the cause of the wide rating discrepancies between the two pilots for any given configuration and recovery technique led to identification of the individual pilot techniques noted above. For example, the first column indicates by a Y the instances in which it could be identified from the time traces that Pilot JS successfully converted a nose slice into a 360 deg roll. These almost always resulted in a 3 to 5 point improvement in rating. There were other attempts at other flight conditions which were unsuccessful and are not identified in this column. Those instances when this pilot used forward stick to effect recovery are indicated in the stick push column. Those cases left blank correspond to a "normal" stick release; there was no attempt to use forward stick except as a last resort. Pilot ML routinely evaluated both a stick release recovery and a stick push recovery, therefore, pilot ratings for both techniques are given.

In essentially every instance both pilots rated recovery technique A superior to any other. There appeared to be several factors involved here. First, it is the simplest technique and requires no compensation or workload on the part of the pilot. Second, as indicated previously, there was a tendency for less use of aileron or rudder to oppose the initial departure

98

motion (or just give up sooner) and hence the post-release aircraft motion was less violent, there was less chance for significant inertia coupling gyrations, and positive damping of aircraft pitch and roll motion with respect to the horizon was more readily apparent. This approach to departure thus takes the appearance of a deliberate, straight-ahead, 1 g stall and the ratings obtained may be more applicable to such a maneuver rather than an inadvertent departure from tracking.

For other departure characteristics and recovery techniques (i.e, B, C, D, E,) the ratings are highly variable with so many interacting factors that few trends can be determined. However, the generally more aggressive application of control in the early departure sequence may make these ratings more appropriate to actual inadvertent departure and recovery. Attempts to correlate ratings with individual parameter variations proved unsuccessful. It was possible to resolve most of the large (4 to 5 point) discrepancies between the two pilots on the basis of the previously mentioned 360 deg roll and stick push recovery techniques. The Configuration 8 ratings show that an aircraft trimmed hands-off to a dynamically unstable attitude is non-recoverable unless the pilot is willing to use full forward stick. However, Configuration 5 which was basically the most stable and docile configuration also proved nearly as non-recoverable for Pilot ML, because there was no clear indication of control loss and he would continue tracking the target until one or more controls bottomed. Relaxing controls to neutral at that point gave a violent departure.

The pilot ratings obtained were inherently influenced by the combined departure warning, departure (closed-loop) characteristics, and recovery (open-loop) properties. These could not be adequately separated, and in hindsight, there is question whether the Cooper-Harper handling quality rating scale is really applicable. For example, the Cooper-Harper rating requires a first assessment as to whether the aircraft is controllable or not controllable. If controllable, the decision is whether performance is adequate or not. Departure involves an inherent, short term loss of control. It is first a matter of recognition and then a matter of aircraft response — Did the pilot think he still had control? Did he indeed have some margin of control? How much aircraft motion was involved before the pilot regained control? Did the pilot regain control? How much concentration was required to detect and take action?

All of these factors or considerations influenced each of the single pilot ratings obtained here. However, the overall gyration involves a succession of interrelated events too broad in scope to relate to a single set of descriptors. Thus separate ratings and descriptors for warning, departure, and recovery appear necessary.

It should also be noted that all configurations employed here exhibited good pitch control and response characteristics. The aircraft did not exhibit longitudinal instabilities except as a result of inertial coupling. The initial loss of control always was in the lateral-directional modes. Recovery always depended upon reducing the angle of attack. A rapid and positive pitch response to control release or stick push was central to the recoveries obtained and the pilot ratings obtained. When any attempt was made to hold pitch attitude or angle of attack constant after the initial nose slice was detected, control of lateral-directional motion could not be maintained and a violent departure resulted from which recovery was impossible. If a configuration were employed which exhibited pitch up or loss of longitudinal control effectiveness as stall was approached, the results might be considerably different from those obtained here.

D. SUMMARY AND CONCLUSIONS

Nine airframe dynamic configurations were investigated to assess various high angle of attack departure and recovery characteristics. All exhibited nose slice type departure and Configuration 9 also had a wing rock tendency. In all cases the α at which nose slice initiated or became apparent to the pilot correlated most closely with the pitch attitude numerator complex zero, ω_θ, moving into the right half plane. Once the departure was triggered, safe recovery was achieved if the aircraft was trimmed hands off for an α at which $N_{\beta_{dyn}}$ was greater than zero, and all controls were released before:

    a. Large anti-departure aileron and/or rudder deflection had been applied

    b. Achieving approximately ± 5 deg β or ψ

    c. Achieving approximately ± 10 deg/sec r

Some configurations were recoverable from larger excursions of β or ψ, however, recovery could not always be obtained. The use of aileron or rudder to oppose nose slice almost always aggravated the departure, and the use of these controls during recovery often decreased the chance of recovery.

Departure onset did <u>not</u> appear correlated with ω_φ or $N_{\beta_{dyn}}$* but these parameters did influence departure severity and recovery characteristics. If all parameters $(1/T_{\theta_3}, \omega_\theta, \omega_\varphi, \omega_{SR}, N_{\beta_{dyn}})$ were in the right half plane or negative, rapid departure was obtained at low α and with little warning and hence little time for the pilot to react. If the lateral-directional parameters $(\omega_\varphi, \omega_{SR}, N_{\beta_{dyn}})$ remained stable (left half plane or positive), recovery was more positive and the aircraft could penetrate further into stall/departure and be recovered, however, departure warning was less pronounced.

The pilots apparently used the change in aircraft dynamics with increasing α and β as departure warning. The configuration having the best lateral-directional characteristics but also the least changes in dynamics with α was downgraded severely because of inadequate warning. In this respect a steady degradation in handling and a slow but firm nose slice provided the best warning and time to react.

Data and pilot ratings obtained for the stick release only recoveries probably relate mostly to 1 g, straight-ahead stall maneuvers. With few exceptions these involved minimum penetration into stall/departure, were readily recoverable control free, and received Cooper-Harper ratings of 3 to 6 from one pilot and 3 to 7 for the other (using stick push). Data and ratings obtained for all other types of recoveries (e.g., B, C, D) probably relate better to actual tracking and maneuvering situations in which inadvertent departure — or delay of departure — is encountered. These cases consistently resulted in Cooper-Harper ratings of 6 to 10. The very significant difference between these two sets of ratings may reflect actual flight situations in which stall and/or spin characteristics obtained from intentional entries (including application of pro-spin controls) tend to be considerably milder than those obtained from inadvertent entries.

The resulting pilot ratings could not be correlated with any single flying quality parameter. The departure characteristics were most dependent upon <u>closed loop</u> (i.e., pitch numerator) parameters with some influence from open

---

*Ref. 18 also cites lack of correlation of nose slice and $N_{\beta_{dyn}}$ or ω_φ parameter values.

loop parameters. Where recovery was possible it was most dependent upon airframe open-loop parameters (including trim) but the possibility of successful recovery was highly dependent upon pilot technique, aggressiveness, sensitivity to cues, etc.

All configurations investigated here exhibited good pitch control and response characteristics. If a configuration was employed which exhibited pitch-up, loss of longitudinal control effectiveness, or any other impairment of longitudinal control, the results might be considerably different from those obtained here.

Finally, it should be noted that the conventional closed-loop pilot model does not appear appropriate for analysis of departure and recovery. Immediately prior to departure the lateral-directional control (if employed at all) tended toward steady or trim type application against the motion of the nose slice. Following departure the preferred method of recovery was to release all controls. Thus the pilot provided no inputs and the recovery was achieved through open-loop, airframe-alone stability and damping. Again, if control was applied during the recovery, the preferred technique was to hold constant forward stick to assure decrease in α and to prevent pitch-up due to inertia coupling. As the aircraft motion subsided the stick was returned to neutral. Thus a closed loop pilot model, per se, does not appear appropriate for departure/recovery application.

SECTION V

PILOT DESCRIBING FUNCTION MEASURES AT HIGH α

Multiloop, multi-input, multi-output, pilot-vehicle describing function measurements were made using three different airframe dynamic configurations representative of high-angle-of-attack, pre-stall flight and a control task closely approximating air-to-air tracking. One configuration assumed symmetric flight ($\beta = 0$) and hence had uncoupled lateral-longitudinal dynamics. Two reflected coupled lateral-longitudinal dynamics discussed in the previous section (Configurations 1 and 3). Three control loop structures were employed as previously shown in Fig. 27. Two were two loop pitch-roll tracking tasks with the heading degree of freedom eliminated to prevent inadvertent yaw error from biasing the pilot's control of roll attitude. As indicated in Section III, the command forcing function was introduced one axis at a time as the primary tracking task. The secondary task was then related to the inter-axis coupling of the airframe. Since the principal coupling was from the longitudinal into lateral motion, the pitch tracking task provided the highest workload for Configurations 1 and 3. The third loop structure was the most realistic of the three. In this instance the forcing function commanded bank of the target aircraft which was also free to change heading (and pitch). The pilot was instructed to track heading and pitch (i.e., to fly in-trail). In order to test the concept that pilots use target bank angle as a primary cue, several heading tracking runs were made with target wings and tail removed from the display. It was determined that this path was of little consequence on the describing function measures; therefore, the pilot was apparently making little use of target bank angle cue in this particular set of tracking tasks.

Describing function measurements were made on both pilots. Each pilot was allowed two training sessions of roughly one-half day each to learn to track the target for 100 sec without inducing a departure. During all training sessions the complete nonlinear $[f(\alpha,\beta)]$ airframe model was utilized and departures could be obtained. For the final data runs the airframe dynamics were frozen at the initial α and β values to provide the necessary stationary control process. The detailed describing function and performance measures

are contained in Ref. 31. In the following we will first describe results of the roll tracking task, then pitch, and finally heading.

A. ROLL PILOT MEASURES AND MODEL

The open-loop roll attitude dynamics for the three configurations are shown in Fig. 46. The root locus and Bode for the uncoupled $\alpha_o = 17.3^o/\beta_o = 0^o$ case is shown at the top of Fig. 46 and that for Configuration 1, $\alpha_o = 18.8^o/\beta_o = 3^o$, is shown in the middle. These two represent the nominal A-7 aircraft dynamics at these flight conditions. The bottom Bode and root locus represents the Configuration 3, $\alpha_o = 18.8^o/\beta_o = 3^o$, case for which the stability derivative N'_α is increased from -0.7 to -1.6 and N'_β is changed from 0 to $+0.3$. The latter results in lateral dynamic parameters which closely approximate those of the uncoupled $\alpha_o = 17.3^o$ case but with the lateral-longitudinal coupling due to sideslip. The change in N'_α primarily affects the longitudinal dynamics as will be shown later.

In the following we shall look at the uncoupled case first and then examine the effects of coupling.

1. $\alpha_o = 17.3^o/\beta_o = 0^o$

Figure 47 presents the open-loop $Y_p Y_c$ amplitude ($+$) and phase ($\square$) data points calculated from the describing function analyzer (DFA) readout at the five forcing function frequencies. The plotted points are the average of two separate runs for pilot ML. These data points have been fit with a transfer function which provides the solid-line amplitude and phase shown. Also shown is a reference 6 dB/octave slope line. It is apparent the pilot has adopted equalization so that $Y_p Y_c$ approximates the crossover model (Ref. 28). Crossover is obtained at 1.5 rad/sec and 35 deg phase margin.

The pilot describing function, Eq. 6, is obtained by subtracting the known airframe amplitude and phase from the DFA data points of Fig. 47 and curve fitting the resulting points (Fig. 48):
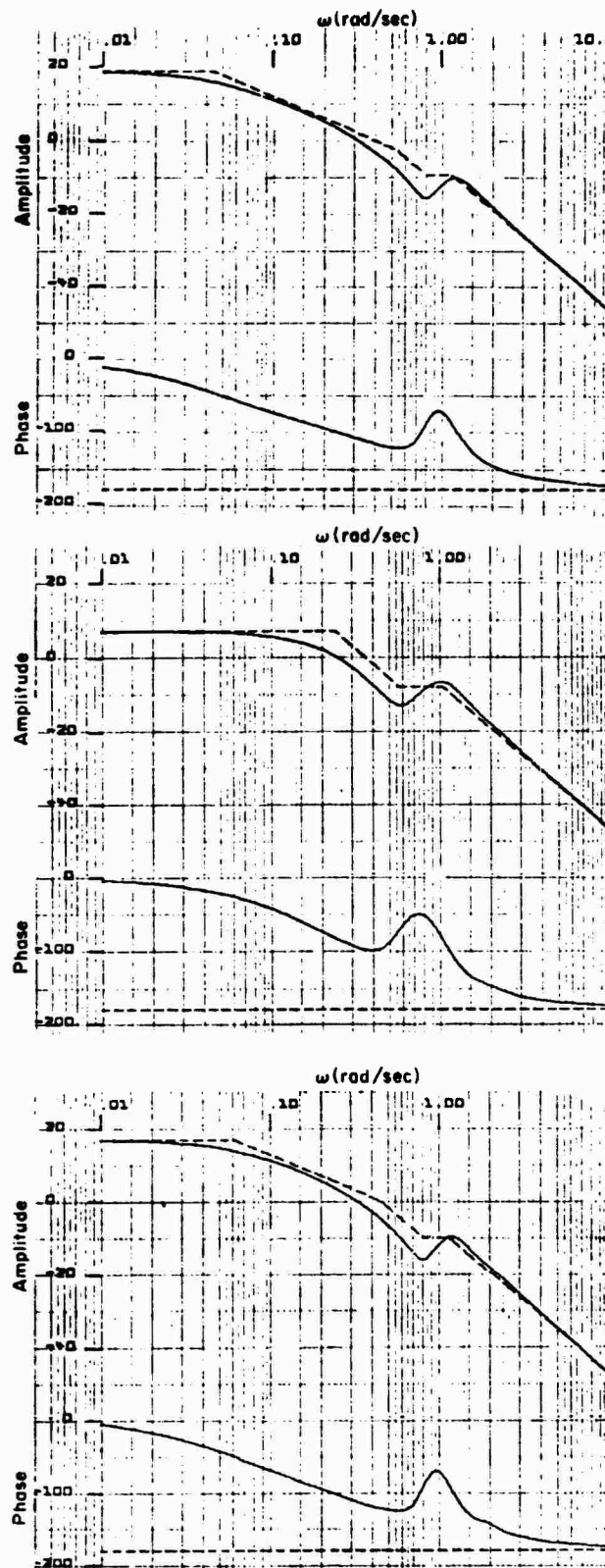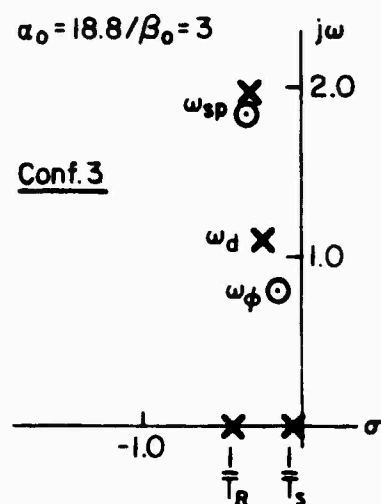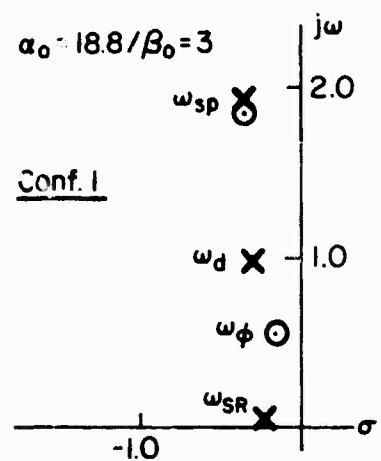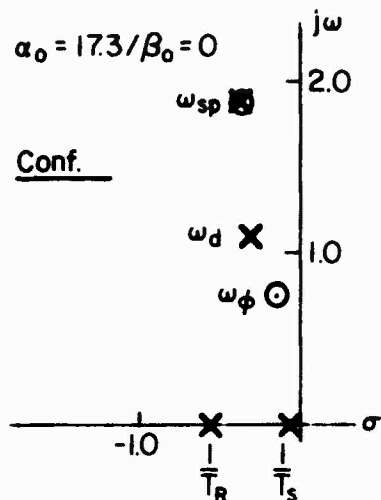
Figure 46. Open Loop Roll-to-Aileron Bode and Root Plots
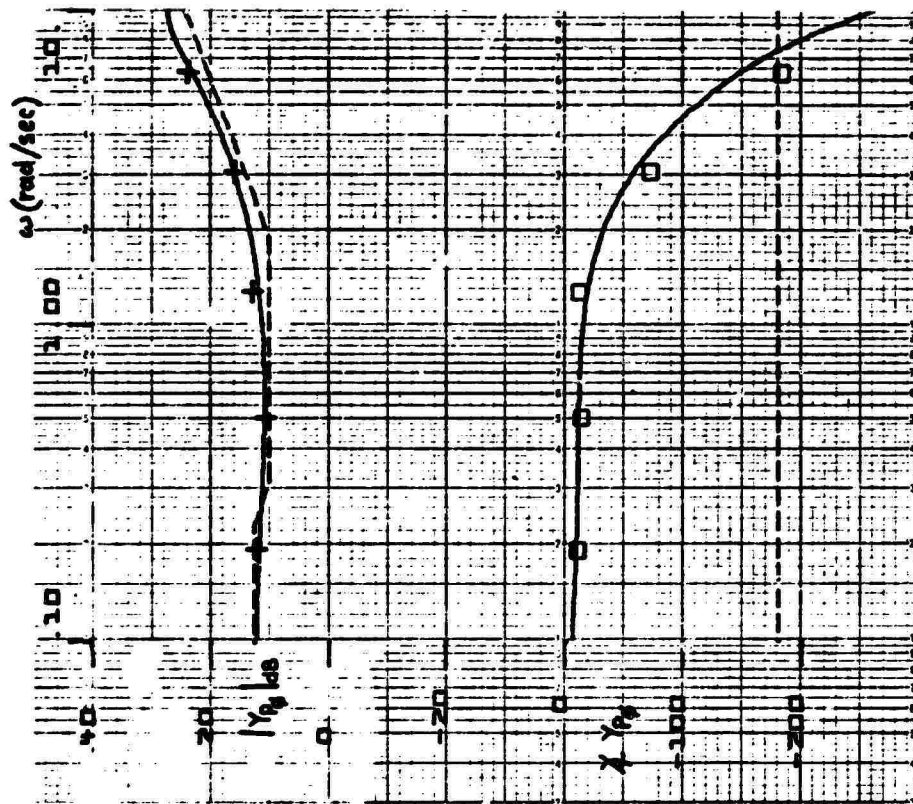
Figure 48. $Y_{p\varphi}$ Data Fit, $\alpha_o = 17.3°/\beta_o = 0°$, Pilot ML

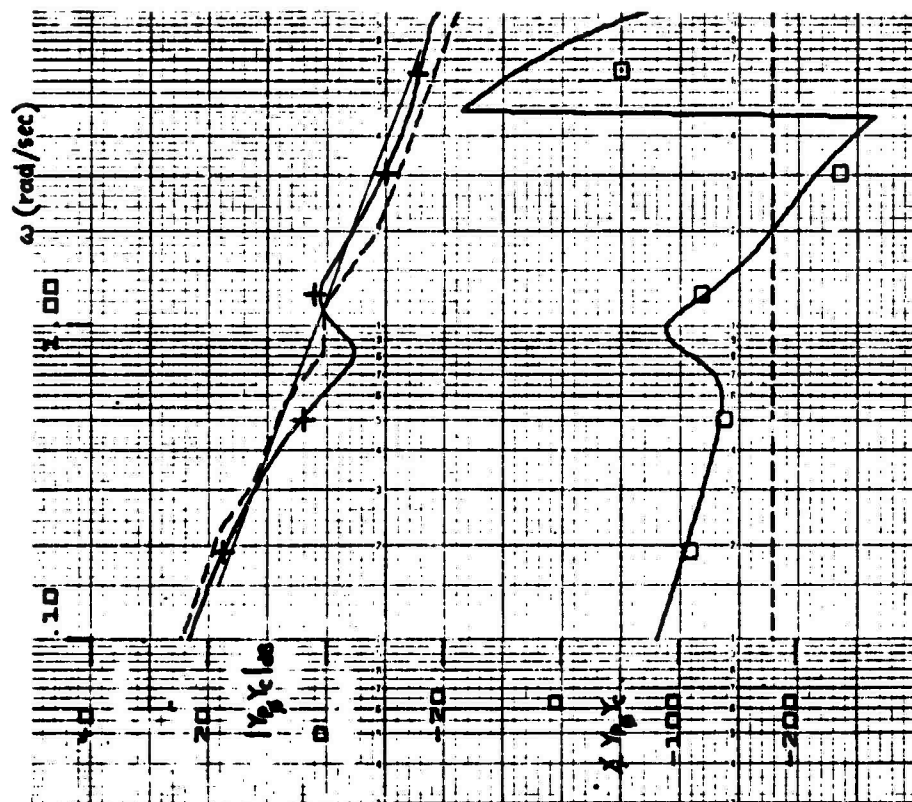Figure 47. Open-Loop $Y_{p\varphi}Y_c$; $\alpha_o = 17.3°/\beta_o = 0°$, Pilot ML

$$Y_{p_\varphi} = 2500 \times \frac{(.316)}{(.23)} \times \frac{(1.88)}{1} \times \frac{1}{[.3\,,\,10](15)} \times e^{-.56s} \qquad (6)$$

$$\underbrace{}_{\text{Gain}} \quad \underbrace{\phantom{\frac{(.316)}{(.23)}}}_{\substack{\text{Low} \\ \text{Frequency} \\ \text{Lag-Lead}}} \quad \underbrace{\phantom{\frac{(1.88)}{1}}}_{\substack{\text{Series} \\ \text{Equali-} \\ \text{zation}}} \quad \underbrace{\phantom{\frac{1}{[.3\,,\,10](15)}}}_{\substack{\text{Neuromuscular} \\ \text{System Lag}}} \quad \underbrace{\phantom{e^{-.56s}}}_{\substack{\text{Time} \\ \text{Delay}}}$$

The results provide an excellent curve fit and also validate the precision pilot model (Ref. 29). However, for all practical purposes the low-frequency lag-lead can be neglected and the equalization simplified to a first-order lead at 1.88 rad/sec.

The pilot has placed the lead essentially at the desired crossover instead of at the roll subsidence lag (0.55 rad/sec) as in the more usual case. In this instance ω_φ/ω_d is considerably less than unity and provides lead between $1/T_R$ and the desired crossover. This reduces the need for lower frequency pilot-generated lead. It may be observed from Fig. 46 that the pilot has placed the series lead at the point where the airframe phase lag is approximately 135 deg (i.e., at the "effective" $1/T_R$).

2. $\alpha_0 = 18.8°/\beta_0 = 3°$, Configuration 1

The measured $Y_p Y_c$ data points and the subsequent curve fit for this case is shown in Fig. 49. It may be noted by comparing Figs. 47 and 49 that the $Y_p Y_c$ for this case is essentially the same for the uncoupled case. Subtracting the controlled element amplitude and phase from the DFA measures and curve fitting these data points results in the pilot dynamics shown in Fig. 50. The transfer function for this data fit is presented as Eq. 7:

$$Y_{p_\varphi} = \frac{3852(.66)(.76)}{(-.03)[.3\,,\,10](15)}\, e^{-.525s} \qquad (7)$$

The right half plane pole at −0.03 is an artifact of the simplified curve-fitting routine for the increasing amplitude but decreasing phase at the lower frequencies. A more accurate phase fit would be obtained at low frequency by a model containing $e^{+\alpha/s}$; however, this also results in an
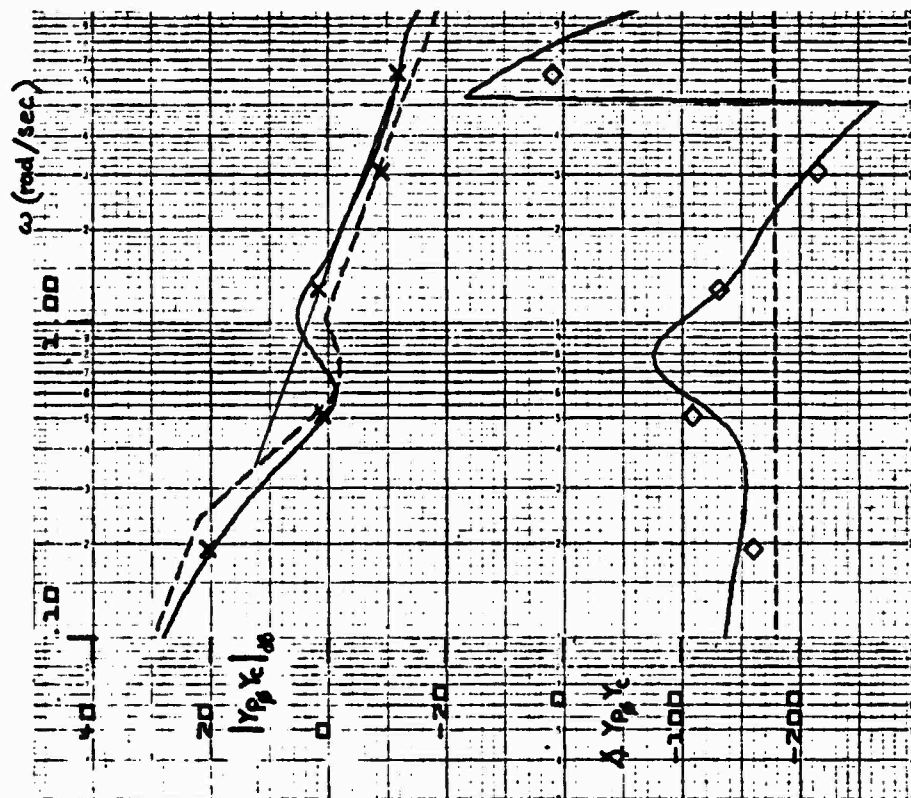
Figure 50. $Y_{p\varphi}$ Data Fit, $\alpha_o = 18.8^o/\beta_o = 3^o$, Configuration 1, Pilot ML
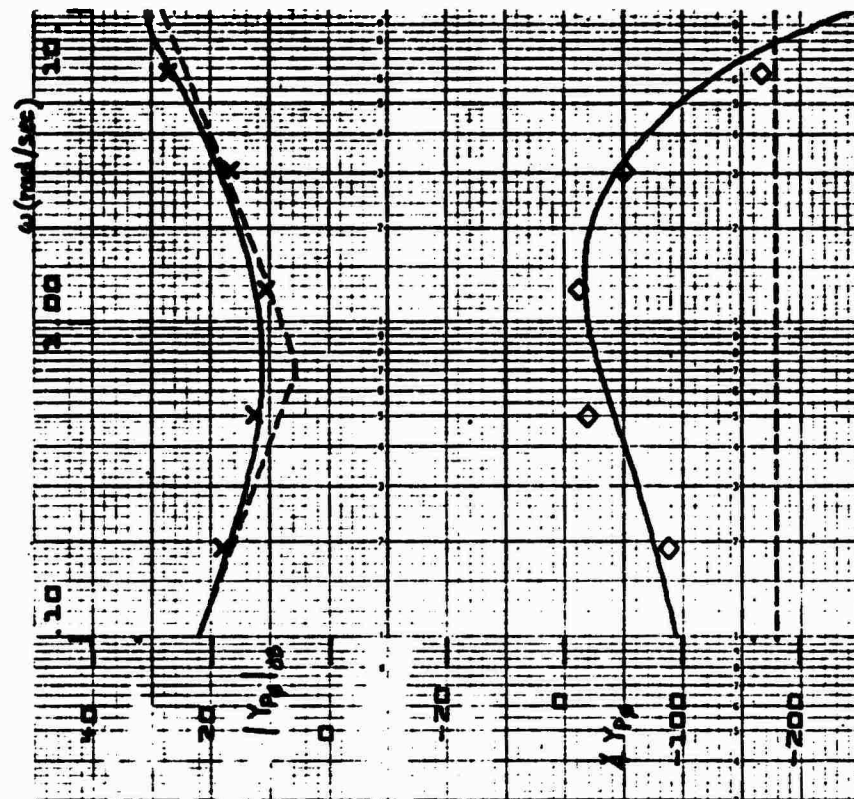
Figure 49. Open Loop $Y_{p\varphi}Y_c$, $\alpha_o = 18.8^o$, $\beta_o = 3^o$, Configuration 1, Pilot ML

appreciable cost increase for the data fit. Referring back to Fig. 46, it may be noted that the airframe has considerably less low-frequency gain for this configuration than for either of the other two configurations; therefore, the pilot adopts a low-frequency lag to increase the $Y_p Y_c$ gain at the lower frequencies. A double lead is then required in the vicinity of $1/T_R$ to obtain adequate phase margin (25 deg) at the crossover of 1.6 rad/sec (Fig. 49).

3. $\alpha_o = 18.8^\circ/\beta_o = 3^\circ$, Configuration 3

The describing function data points and the curve fit for this configuration are shown in Fig. 51. Again, the pilot accomplishes the crossover at 1.4 rad/sec but in this case with approximately 40 deg phase margin. As with the two previous cases, the pilot adopts equalization to achieve a $Y_p Y_c$ such that the crossover model applies. Subtracting the known Y_c and curve fitting the resulting amplitude and the phase data points provides a pilot model given by Eq. 8 and shown in Fig. 52.

$$Y_{p_\varphi} = \frac{2907(.48)(1.34)}{(.208)[.3 , 10](15)} e^{-.5s} \tag{8}$$

In this instance zero weight was assigned to the lowest-frequency phase data point (for curve-fitting routine). Thus, in fitting the low-frequency amplitude data point but not the phase, it obtained a left half plane pole at 0.21 rad/sec. As might be expected on the basis of similarity of airframe dynamics between this case and the uncoupled case, the pilot models of Eqs. 6 and 8 are essentially the same.

4. Summary

Figure 53 presents a direct comparison of the $Y_p Y_c$ data points obtained for the three configurations and Fig. 54 presents the Y_p data points. It may be observed that the data exhibit less scatter than often is obtained for multiple runs of a single configuration. The only significant difference between the configurations is in the low-frequency region where it appears the coupled lateral-longitudinal airframe dynamics cause the pilot to use higher gain and have considerably greater phase lag. In the region above
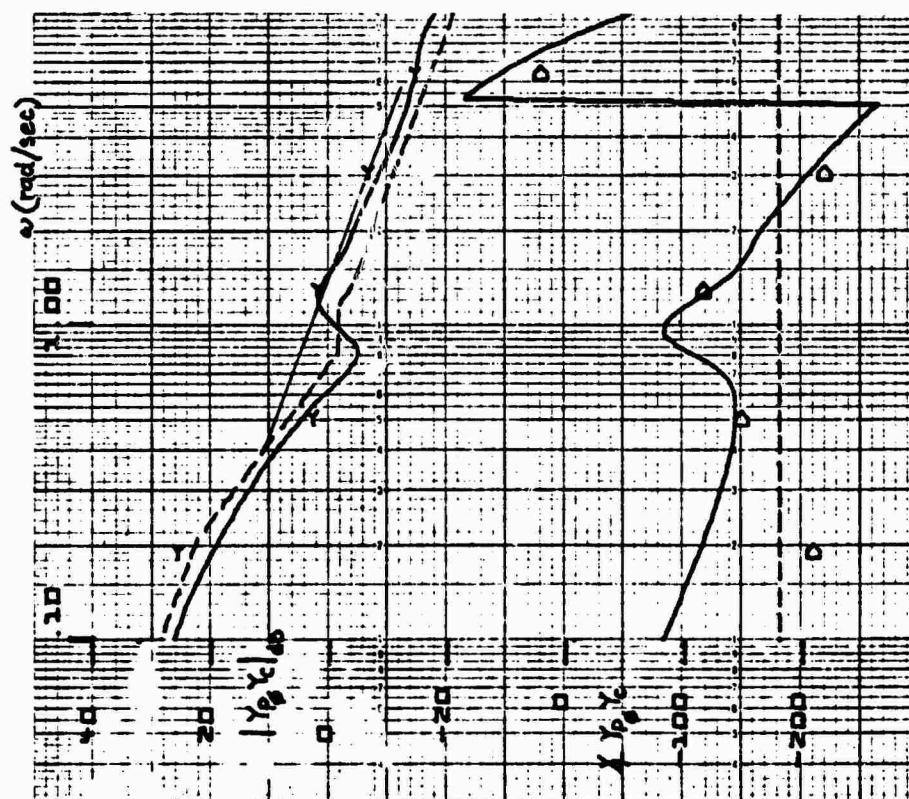
Figure 51. Open Loop $Y_{p\varphi}Y_c$, $\alpha_O = 18.8°/\beta_O = 3°$, Configuration 3, Pilot ML

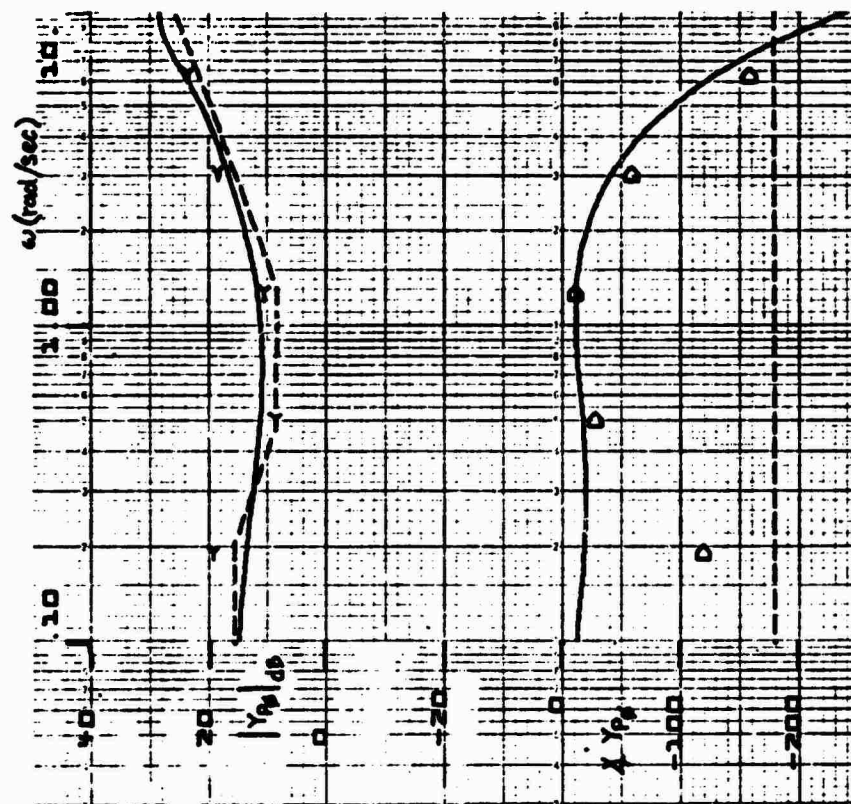Figure 52. $Y_{p\varphi}$ Data Fit, $\alpha_O = 18.8°/\beta_O = 3°$, Configuration 3, Pilot ML

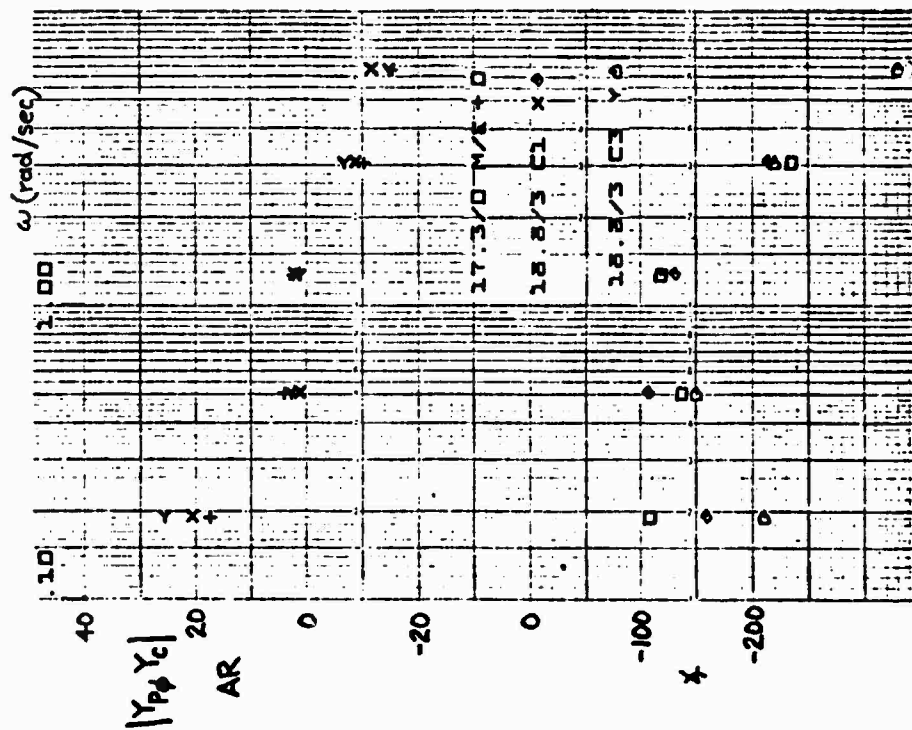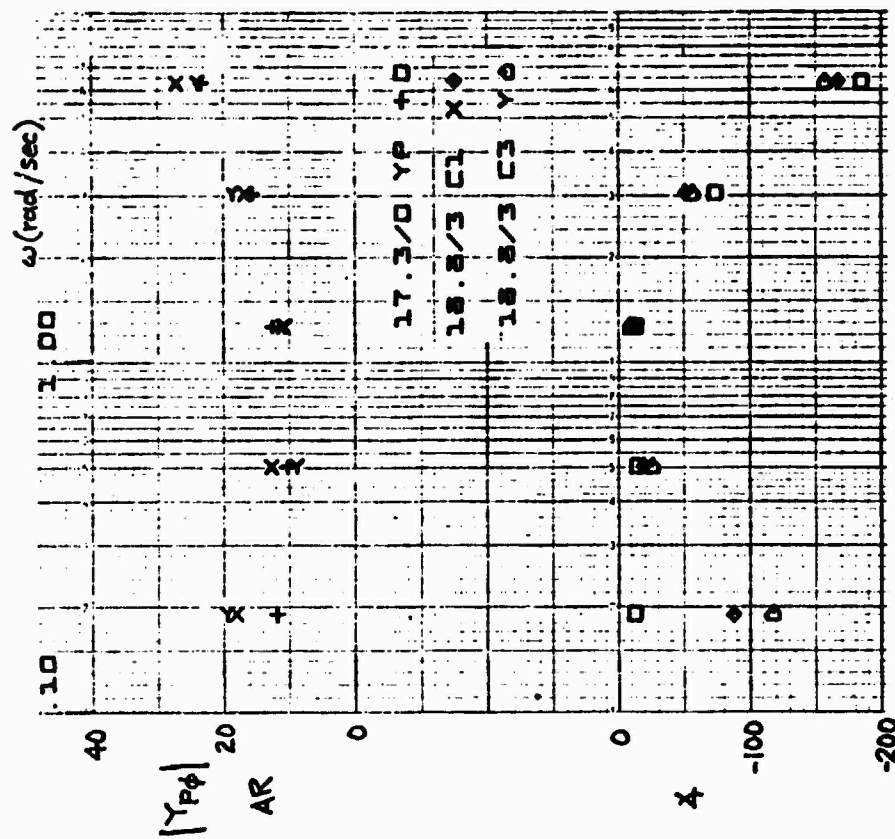Figure 54. $Y_{P\phi}$ Data Points for the Three Cases, Pilot ML

Figure 53. Open-Loop $Y_{P\phi}Y_c$ Data Points for the Three Cases, Pilot ML

0.5 rad/sec there is little or no significant difference between the airframe dynamics employed and little reason for the pilot describing function measures to differ in this frequency band. The coupling had little influence on the crossover desired or achieved. In the region of crossover a single pilot model would suffice with a first-order series lead located at the dutch roll. The major effect of the multiloop, multi-input, multi-output task (with a roll command forcing function) is to modify the pilot's low-frequency compensation.

B. PITCH PILOT MEASURES AND MODEL

The open-loop pitch dynamics for the three controlled element configurations are shown in Fig. 55. Again, the uppermost Bode and root locus plots represent the uncoupled case, the middle plots the nominal A-7 at 18.8 deg α_0 and 3 deg β_0, and the lower plots the Configuration 3 case with β_0 = 3 deg and N'_α = −1.6. It may be noted that the three configurations represent three different values of $1/T_{\theta_3}$ (from 0 to −0.2). There is also considerable difference in low-frequency amplitude ratio for the most highly coupled configuration (3).

In the following, the data obtained will be analyzed on two bases. First, we will neglect the contribution of the roll loop closure (see Fig. 27) and assume the controlled element is described by the single open-loop Y_c shown in Fig. 55. This is an approximation only for the two cases having lateral-longitudinal coupling. Second, we will analyze Configuration 1 assuming the complete multiloop structure and closing the inner roll loop using the pilot model obtained in Subsection A-2, preceding.

1. Single-Loop Models

a. $\alpha_0 = 17.3°/\beta_0 = 0°$

The $Y_p Y_c$ data were fitted for one set of measurements for Pilot ML and are presented in Fig. 56. These are identified by the $\times$ and $\square$ in Fig. 56. These points represent an average of two runs having a maximum of ±2 dB and ±10 deg phase from the data point plotted. The data spread for two runs by Pilot JS is indicated by the ϕ on Fig. 56. These data points were not fitted; they are presented here to show the consistency between the two pilots. Pilot JS

112
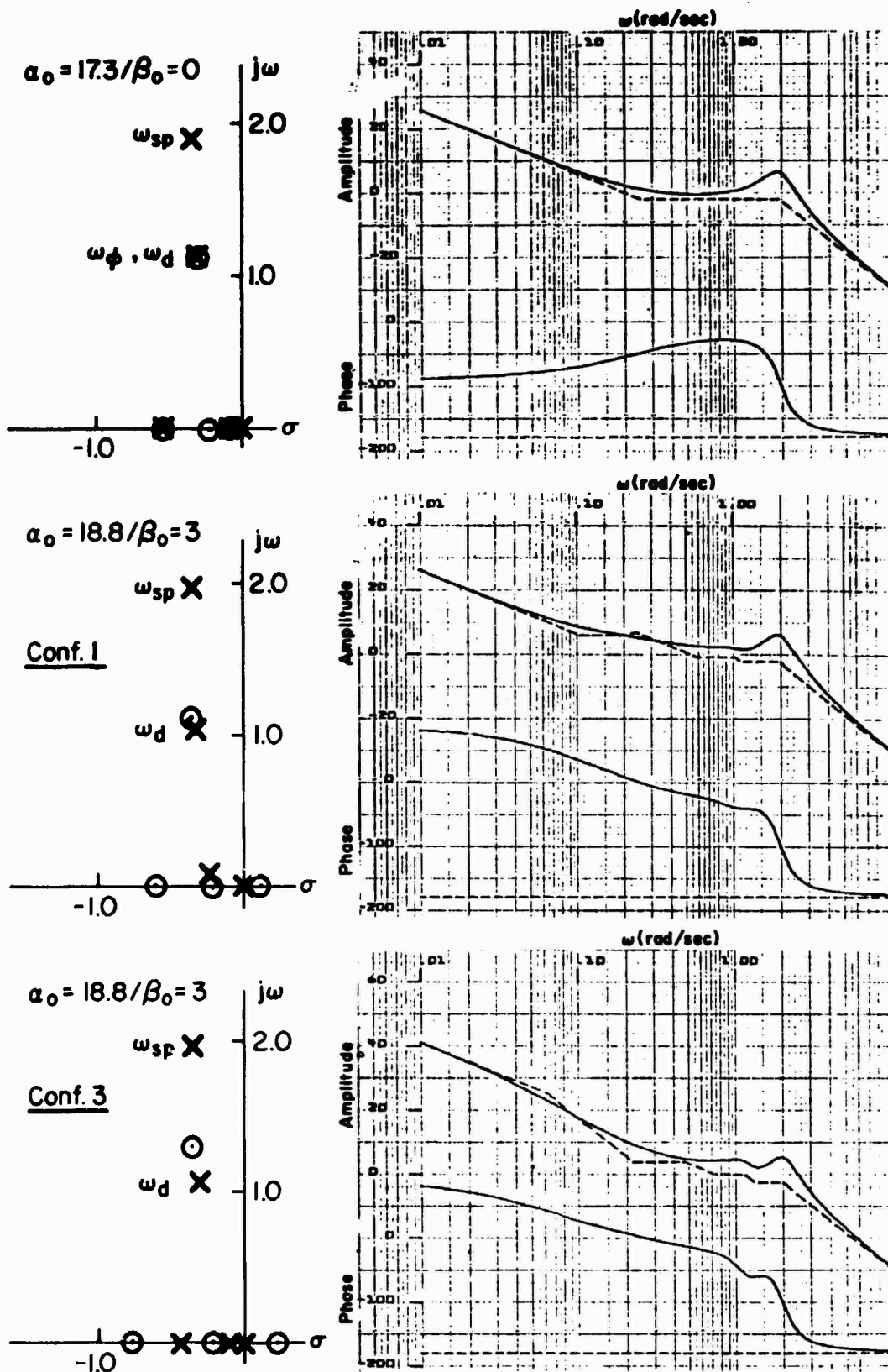
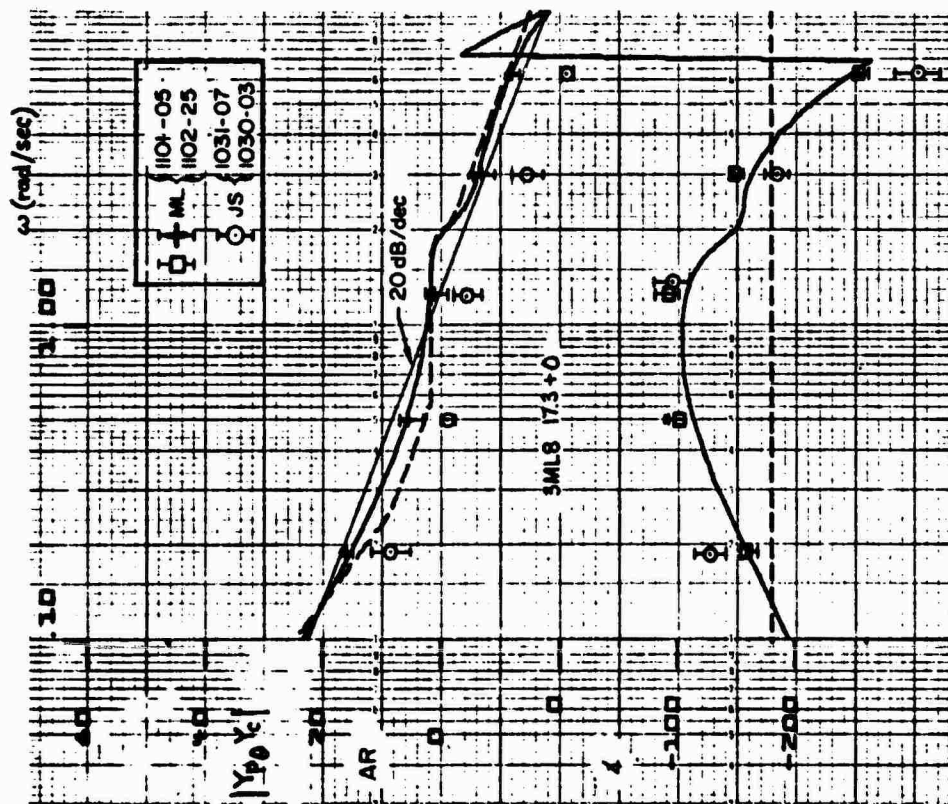Figure 55. Open Loop Pitch-to-Elevator Bode and Root Plots

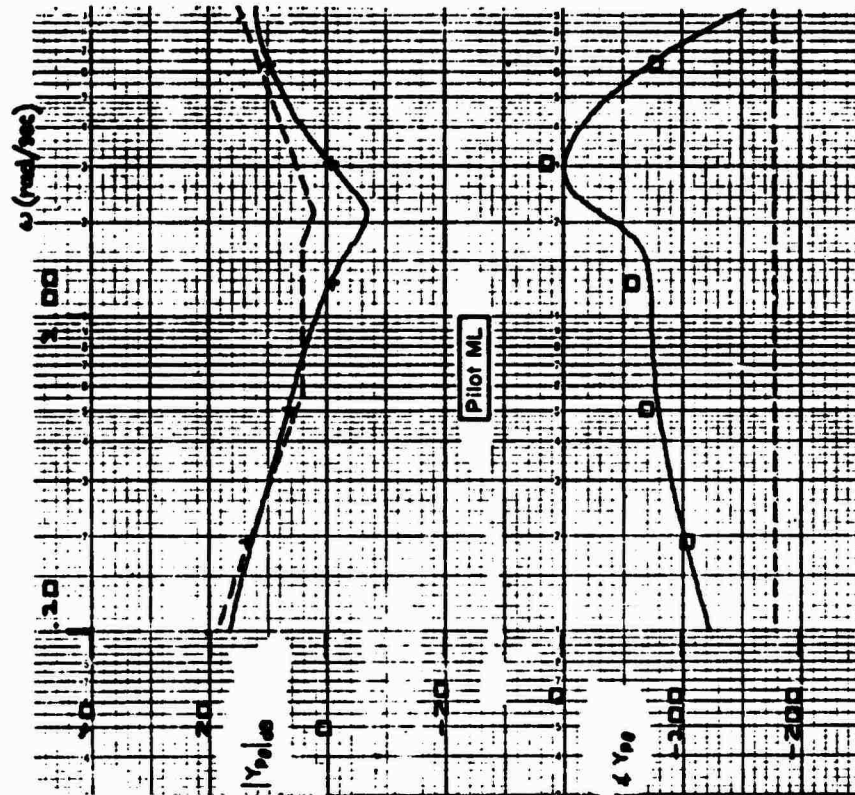Figure 57. Y_{p_θ} Data Point Fit, $\alpha_0 = 17.3^\circ/\beta_0 = 0^\circ$, Pilot ML

Figure 56. Open Loop $Y_{p_\theta}Y_c$, $\alpha_0 = 17.3^\circ/\beta_0 = 0^\circ$

obviously was closing the loop with a lower gain and therefore had a cross-over somewhat below 0.5 rad/sec, whereas Pilot ML achieved a crossover near 2 rad/sec. A 6 dB per octave reference slope line is also shown on Fig. 56. It is apparent that both pilots closely approximate the crossover model. Pilot JS would appear to be placing a first-order lag on top of $1/T_{\theta_2}$ and a lead near ω_{sp} as might be expected (see Fig. 55). However, the transfer function fit to the Pilot ML data indicate he is using somewhat more complex equalization. This may be observed by subtracting the known single-loop (this case is uncoupled) Y_c amplitude and phase from the $Y_p Y_c$ data points of Fig. 56 and fitting them as shown in Fig. 57. The Y_p transfer function is shown in Eq. 9:

$$Y_{p_\theta} = \frac{584(.565)[.226, 2.1]}{(-.08)(1.69)(10)[.5, 10]} e^{-.25s} \qquad (9)$$

Again, this compares well with the precision pilot model with the exception of the series lead: a low-frequency lag-lead is employed to increase the low frequency gain; the pilot acts as a pure gain in the crossover region; and the third-order neuromuscular system lags are at about 10 rad/sec. The main difference is the more complicated series equalization which consists of a second-order lead over a first-order lag. From the amplitude asymptotes of Fig. 57 it appears that this complex equalization might be approximated as a simple first-order lead; however, in order for the inflections of the fitted curve to closely match the actual amplitude ratio and phase data points a lowly damped second-order lead is required. It is apparent that the pilot is precisely inverting the short-period characteristics. The current precision model does not allow for such a second-order lead; however, the precision model was also obtained with Y_c's having much more ideal dynamic characteristics than those for the high α case employed here. That is, they did not have second-order dynamics in the region of the crossover and in our case the pilot is achieving crossover right at the short-period mode. Thus, the series equalization might be expected to be more complex.

There is other evidence to support the existence of second-order lead equalization. A root plot of the early Hall data (Ref. 10) is shown in Fig. 58. Two data points at roughly 1.5 rad/sec and low damping ratio are shown to lie in a region in which double lead was employed. These have
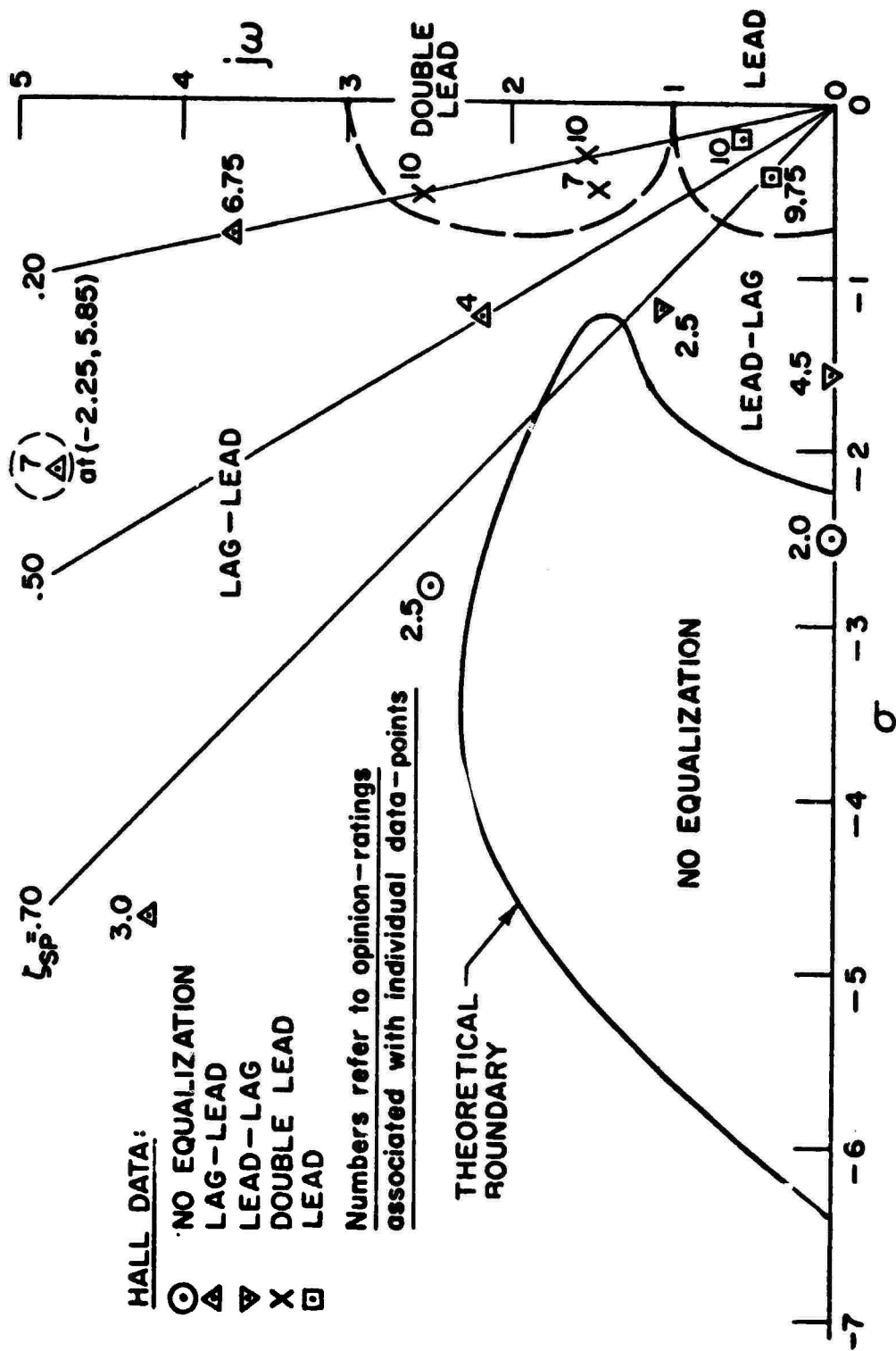
115

Figure 58. Comparison of Theoretical Non-Equalized Boundary with Hall Measured Data
(From Ref. 10)

ratings of 7 and 10. A third data point is at roughly 2.5 rad/sec and also achieved a rating of 10. It may be noted from Fig. 55 that the short-period for all three configurations investigated here would lie in approximately the center of the double lead area shown in Fig. 58. The Cooper-Harper ratings of 8-9 obtained for the three configurations in this simulation are also consistent with the Hall data.

The Shirley data (Ref. 11) also resulted in pilot models with second-order lead. The example transfer functions shown in Table 9 show the pilot is capable of nearly canceling second-order modes of the controlled element.

TABLE 9

EXAMPLE PILOT TRANSFER FUNCTIONS
FROM SHIRLEY (Ref. 11)

Y_c	Y_p
$\dfrac{5\ e^{-.1s}}{[s^2 + s + 5]}$	$\dfrac{1.16\ e^{-.25s}\ (s + .5)[s^2 + 4s + 5]}{(s + .13)(s + 2)}$
$\dfrac{10\ e^{-.1s}}{[s^2 + 2s + 10]}$	$\dfrac{11\ e^{-.3s}\ (s + .4)[s^2 + 3s + 10]}{(s + .1)(s + 2.32)}$

The precise reason for the Hall and Shirley data to result in second-order leads is not known. For the task employed in our simulation it is suspected that the pilot learned to completely suppress the short-period dynamics in order to prevent departure. That is, during the task learning period with the unfrozen aerodynamics, relatively small increases in angle of attack could result in departure. Since the short-period mode is predominantly α and θ motion, the pilot was forced to control α and θ quite tightly to suppress overshoots. Such complete suppression of the short-period mode would then require the complex equalization shown in Fig. 57. However, the use of such equalization would not be suspected from the open-loop controlled element dynamics shown in Fig. 55. There are also no known pilot rating functionals

for second-order lead equalization. Thus, it would be difficult indeed to predict both the pilot model and pilot rating for pitch attitude control at this 17.3 deg α, 0 deg β case.

b. $\underline{\alpha_0 = 18.8^\circ / \beta_0 = 3^\circ, \text{ Configuration 1}}$

The Y_pY_c amplitude and phase data points for this case are shown in Fig. 59. Again, the ✗ and ◇ represent Pilot ML while the ⌀ represent Pilot JS. Only the data points for Pilot ML have been fitted. As with the lateral data, the lowest-frequency phase point was given zero weight in the data fit for economy of computation.

For this case the crossover model seems better suited to the lower gain pilot (JS). Pilot ML adopted a slope somewhat less than 6 dB per octave. This decreased slope has been observed previously (Ref. 30) on subcritical tasks where the controlled element has a right half plane pole. Referring back to Fig. 55, it will be noted that this configuration does have a right half plane zero at 0.1 rad/sec. Closing the $\theta \rightarrow \delta_e$ loop drives the open-loop pole from the origin into this zero and therefore results in a right half plane closed-loop pole. The closed-loop right half plane pole would normally be expected to result in a pitch attitude instability that would prevent obtaining describing function data. However, if the pitch attitude loop is closed tightly, the closed-loop pole is essentially driven into the open-loop zero and there is very little pitch modal response. The small pitch modal response together with the low frequency provides a very long, slow pitch divergence wh'   would not be observable. But, the instability will show up in another mode. the situation is analogous to tight attitude regulation for precise path control with an aircraft on the backside of the power required curve. The path numerator has a right half plane zero which gives rise to an unstable closed-loop mode. With tight attitude regulation, stable path control is obtained and the instability shows up as a speed divergence. For our high α case, the right half plane zero arises due to the coupling stability derivative, N'_α. From the previous analysis we know the closed-loop instability shows up in a lateral mode (nose slice) and the pilot must close the $\varphi \rightarrow \delta_a$ loop to restabilize it. Therefore, we might expect the slope in the region of cross-over to be less than 6 dB per octave. The end result is that the pitch attitude

118

control task is simila: to the uncoupled $17.3^\circ/0^\circ$ case except the pilot is now **required** to close a $\varphi \rightarrow \delta_a$ loop to decouple the lateral-longitudinal motion and hence is working harder.

The pilot describing function is again obtained by subtracting the Y_c from the $Y_p Y_c$ data of Fig. 59 and curve fitting the resulting data points. As indicated previously we will first assume the effective Y_c is adequately described by the open loop $\theta \rightarrow \delta_e$ transfer function of Fig. 55. The resulting data points and their curve fit are presented in Fig. 60. The pilot model for the fit is given in Eq. 10:

$$Y_{p_\theta} = \frac{930.8(.22)[.3\,,\,2.3]}{(.006)(5.1)(7.6)[.5\,,\,10]}\,e^{-.306s} \tag{10}$$

Again, the pilot model has the form of the precision model with a series equalization consisting of a second-order lead over a first-order lag. From Fig. 60 it is apparent that the pilot is acting as a pure gain in the region just below crossover and is applying the second-order lead to cancel the vehicle short-period mode. In this case the effect of the second-order lead is more pronounced because of the greater separation between it and the associated lag break point.

c. $\underline{\alpha = 18.8^\circ/\beta = 3^\circ, \text{ Configuration } 3}$

The $Y_p Y_c$ data points and curve fit for Pilot ML are shown in Fig. 61. Also shown are the raw data points for Pilot JS. Again, the slope in the region of the crossover is less than that which would be obtained with the crossover model and again the pitch numerator has a right half plane zero. In this case it is at 0.25 rad/sec and provides a significant increase in the airframe low-frequency amplitude. Also, upon closure of the pitch attitude loop, the unstable root is driven further into the right half plane and thus the mode divergence is more rapid. The unstable mode should be more apparent to the pilots and hence constrain the gain and equalization necessary to achieve satisfactory performance. This is probably the reason why the describing function data points for both pilots are in closer agreement for this configuration than for the previous two.

Figure 60. $Y_{p\theta}$ Fit for $\alpha_o = 18.8°/\beta_o = 3°$ Configuration 1, Pilot ML
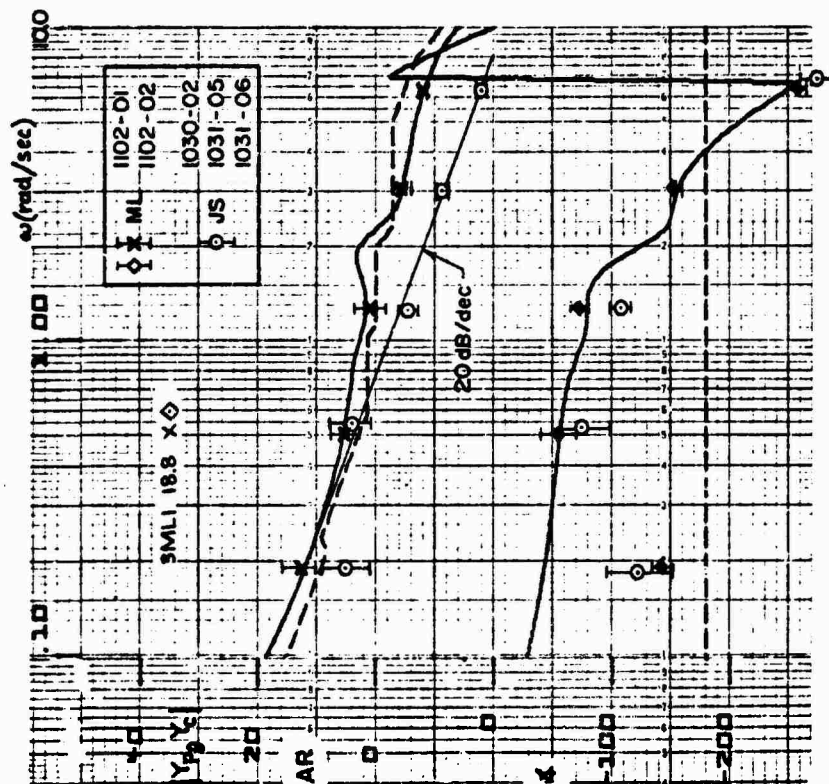
Figure 59. Plot of $Y_{p\theta}Y_c$ Fit for $\alpha_o = 18.8°/\beta_o = 3°$ Configuration 1
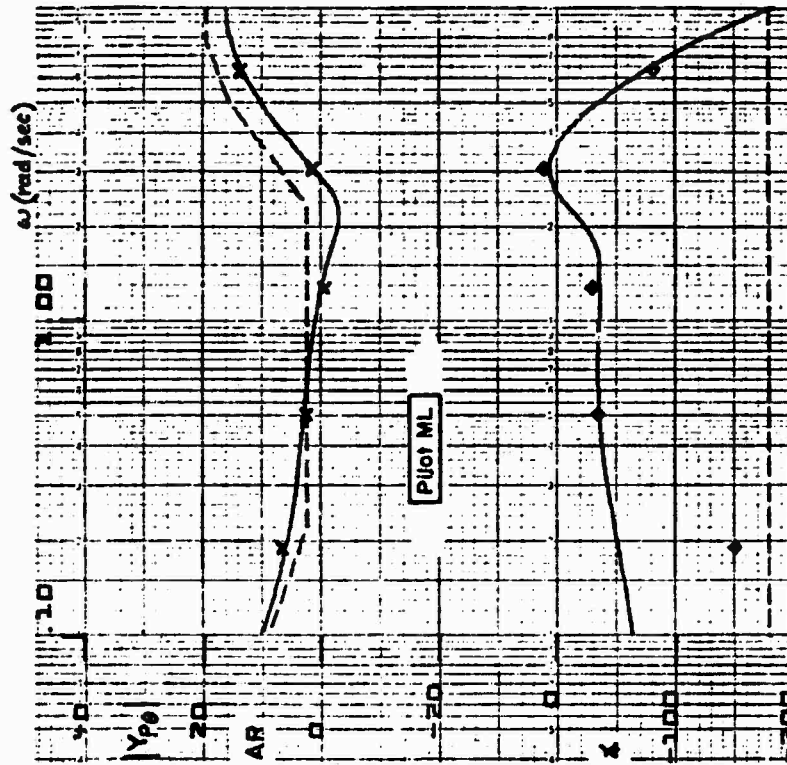
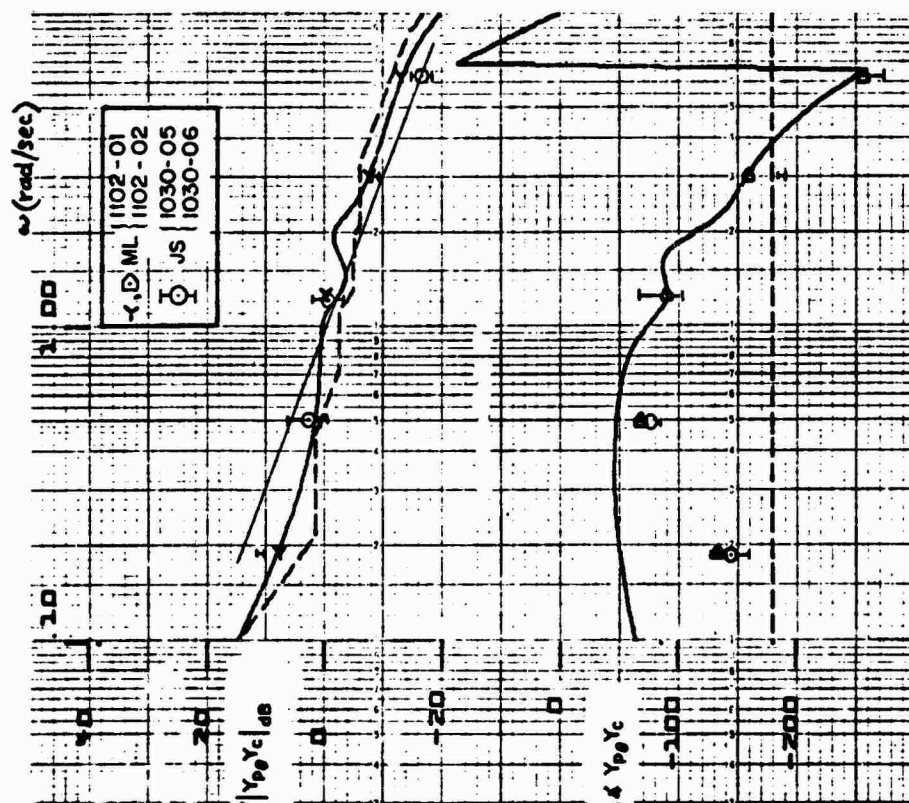Figure 61. Open-Loop $Y_{p_\theta}Y_c$, $\alpha_o = 18.8^o/\beta_o = 3^o$, Configuration 3
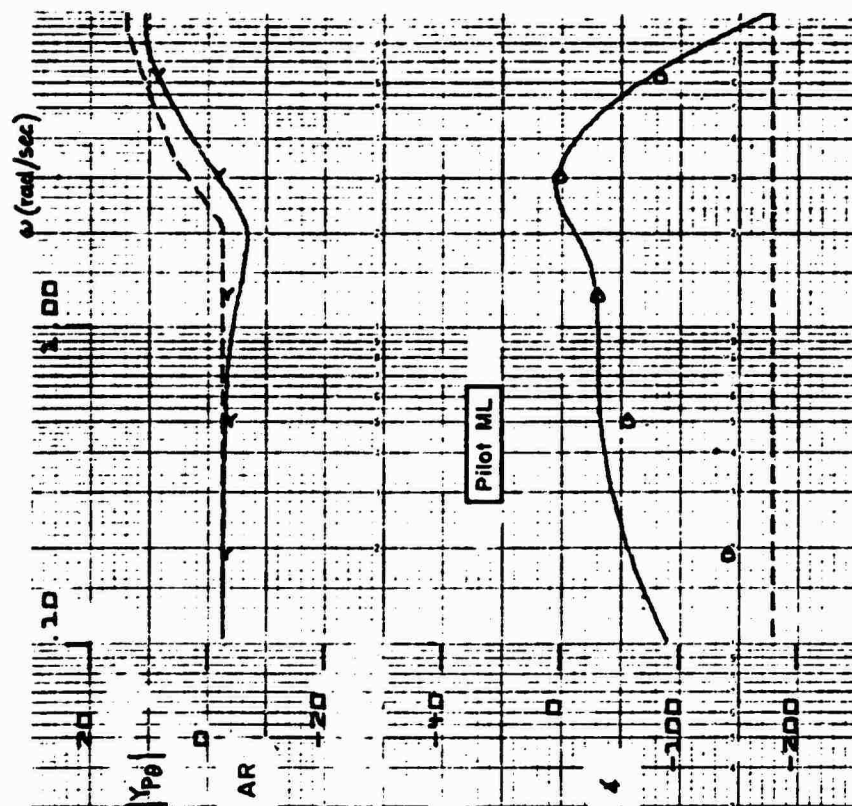
Figure 62. Y_{p_θ} Data Fit, $\alpha_o = 18.8^o/\beta_o = 3^o$, Configuration 3, Pilot ML

Again, subtracting the open-loop $\theta \rightarrow \delta_e$ airframe amplitude and phase from the $Y_p Y_c$ data points of Fig. 61 gives the data points and curve shown in Fig. 62. The pilot model transfer function is presented in Eq. 11:

$$Y_{p_\theta} = \frac{491[.37, 2.11]}{(3.4)(8.7)[.5, 10]} e^{-.286s} \tag{11}$$

Here, the low-frequency lag-lead is not required because of the higher gain of the Y_c. The pilot essentially adopts a pure gain out to the short-period frequency and then assumes a second-order lead to cancel the short-period resonance peak.

d. Summary

Figure 63 presents a direct comparison of the $Y_p Y_c$ data points from the three configurations for Pilot ML. These demonstrate the uniformity the pilot was achieving in the pitch task — coupled versus uncoupled.

Figure 64 presents a direct comparison of the Y_{p_θ} data points after removing the controlled element amplitude and phase. As with the roll closure these show remarkable similarity in the region of crossover and above and could readily be fit by a single model. Again, the major difference is in the low-frequency band with the greater coupling conditions showing the lower pilot amplitude contribution.

This is precisely the opposite of the trend shown in Fig. 54 where the lateral Y_{p_φ} for the coupled case showed increased low-frequency gain. It appears that the pilot is achieving a tradeoff between the two axes — possibly to effect a decoupling of the motions. The major coupling is from longitudinal to lateral via N_α. Therefore, as coupling increases (N_α increased), the pilot reduces his longitudinal gain and increases the lateral gain.

In all cases, whether coupled or uncoupled, the pilot is closing the pitch loop essentially at the short period and is nearly canceling the short-period peak through generation of a second-order lead. This unusual equalization has apparently been adopted through the necessity to avoid excessive angle of attack and subsequent nose slice divergence. A clue to the possible tension of the pilot in pitch control is the quite small time delay ($0.25 < \tau < 0.3$ sec)
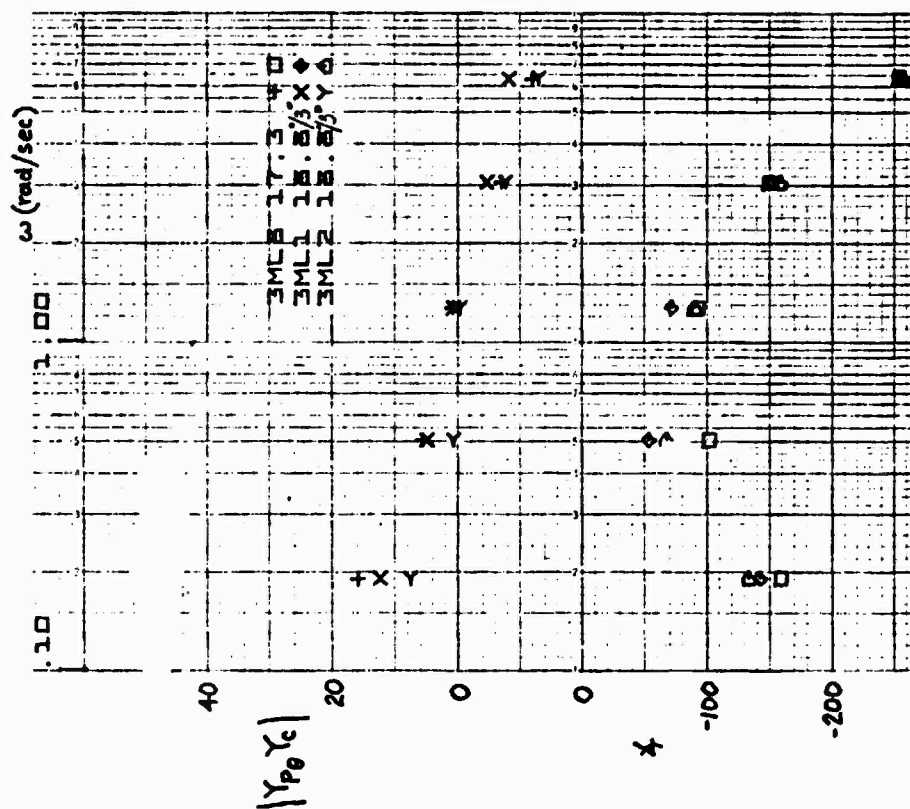
122

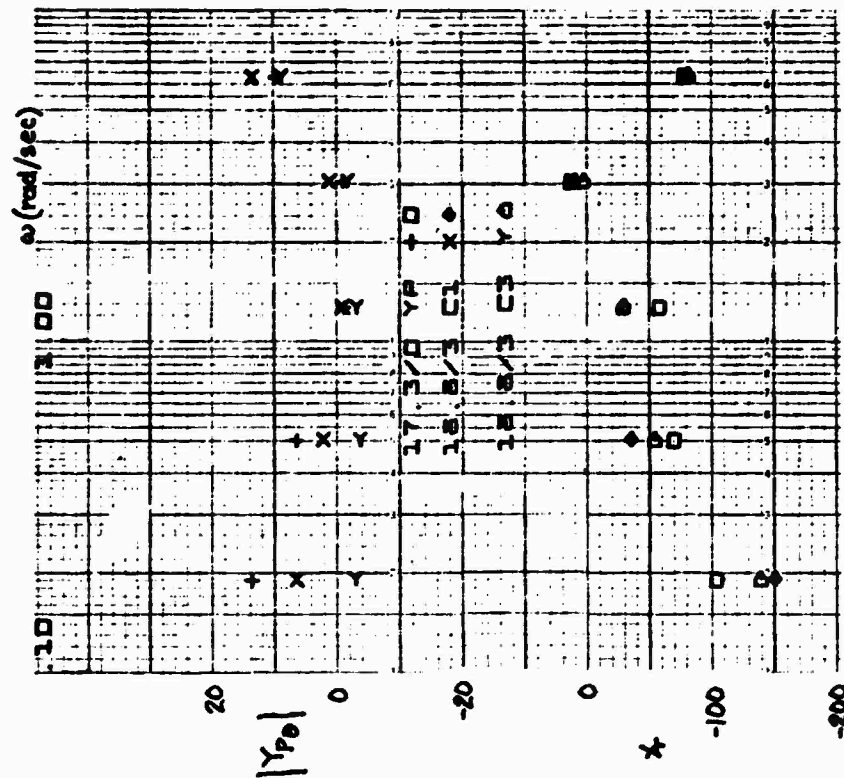Figure 63. $Y_{p_\theta}Y_c$ Data Point Comparison for the Three Cases, Pilot ML

Figure 64. Y_{p_θ} Data Point Comparisons for the Three Cases, Pilot ML

obtained in this task as compared to that ($0.5 < \tau < 0.56$ sec) obtained in roll. This might also signal that the pilot closes the pitch loop as the inner loop and roll as the outer loop.

The $Y_p Y_c$ amplitude and phase did not fit the crossover model for the two coupled cases. These exhibited considerably flatter amplitude through the crossover region and are consistent with previous data obtained with a controlled elements having unstable modes.

2. Multiloop Model

Because the coupling from longitudinal motion into lateral is significant for the asymmetric flight cases, Configuration 1 will be analyzed by multi-loop techniques. The extent of the coupling is indicated by the time traces of Fig. 65 which are taken from a pitch command data run with Pilot ML. It will be noted that the θ command evokes roughly ±0.7 in. of longitudinal stick response and a peak $\Delta\alpha$ of about ±2.9 deg. This then couples through the airframe to require twice as much lateral stick motion and a peak bank angle of over ±10 deg. On the other hand, the coupling from lateral motion into longitudinal motion is relatively insignificant. Therefore, we will assume the φ loop is the inner loop and determine its effect on the outer, θ, loop. The inner loop is assumed to be closed with the pilot model of Eq. 7. The effective airframe pitch dynamics are then obtained as shown in Eq. 12:

$$Y'_{c_\theta} = \frac{N^{\theta\,'}_{\delta e}}{\Delta'} = \frac{N^{\theta}_{\delta e} + Y_{p_\varphi} N^{\theta\varphi}_{\delta e \delta a}}{\Delta + Y_{p_\varphi} N^{\varphi}_{\delta a}} \qquad (12)$$

where

$$N^{\theta}_{\delta e} = -2.91(-.1)(.21)(.593)[.279 , 1.16]$$

$$N^{\varphi}_{\delta a} = 2.2[.25 , .57][.184 , 1.92]$$

$$N^{\theta\,\varphi}_{\delta e \delta a} = -1.29(.253)[.266 , .56]$$

$$Y_{p_\varphi} = \frac{3852(.66)(.76)(-7.67)^2}{(-.03)[.3 , 10](15)(7.67)^2}$$

$$\Delta = [.974 , .238][.296 , 1.03][.185 , 1.96]$$

$$Y'_{c_\theta} = \frac{-2.91(.24)(.604)(2.02)[.067 , .39][.12 , 1.87]}{(0)(.48)(1.96)[.18 , .45][.167 , 1.7][.134 , 2.07]}$$
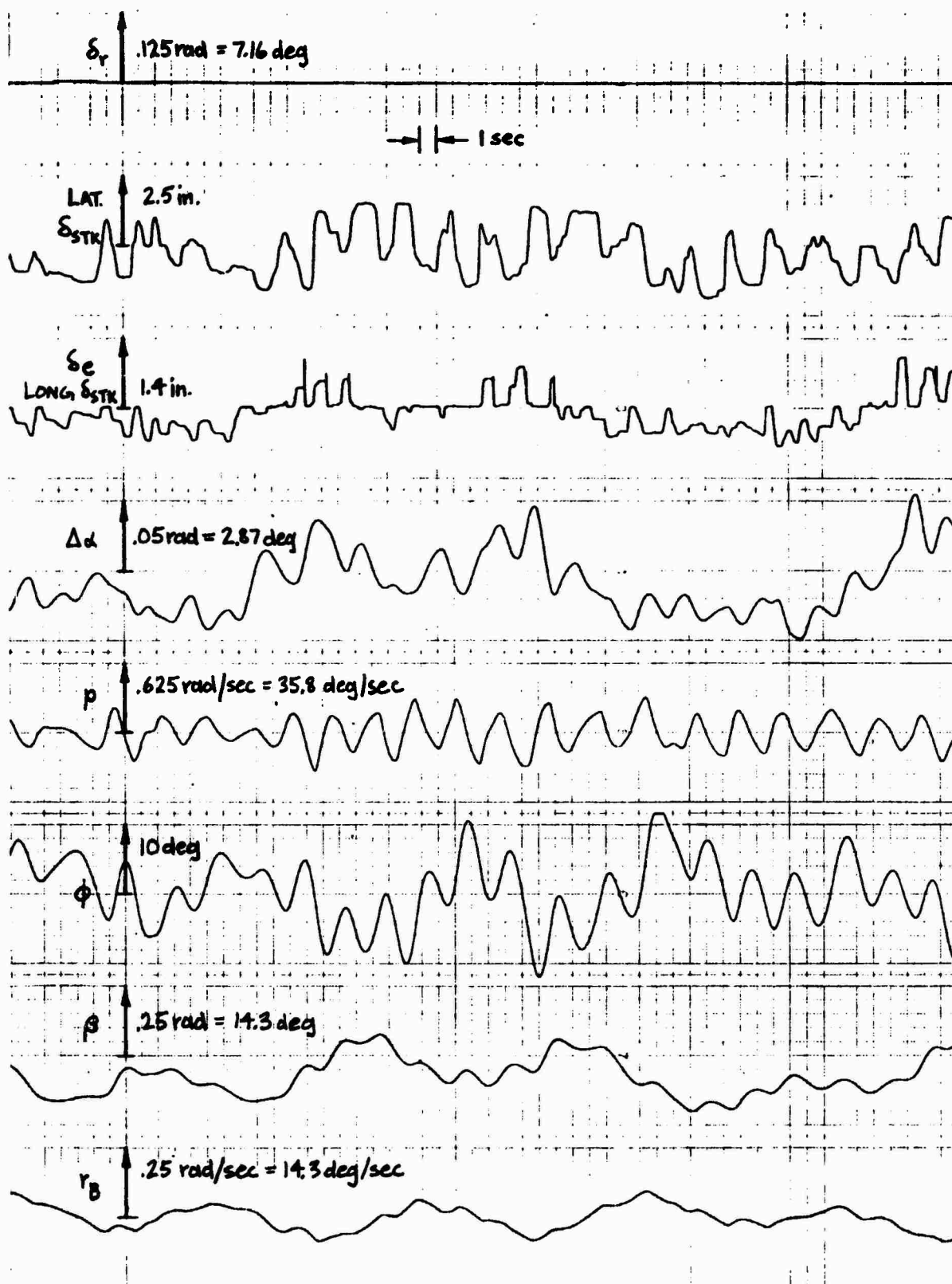
124

Figure 65. Time Traces for θ_c Tracking with Coupled Airframe

The Bode asymptote for the resulting effective pitch airframe, Y'_{c_θ}, is shown in Fig. 66. Note that the low- to mid-frequency asymptote closely resembles that for the open-loop, uncoupled, $17.3^\circ/0^\circ$ case of Fig. 55. That is, the low- and mid-frequency asymptote of Fig. 66 has lowered to resemble that of Fig. 55. If we then apply the pilot model derived from the uncoupled case (Eq. 9) and plot $Y_{p_\theta}Y'_{c_\theta}$ amplitude and phase at the forcing function frequencies, we obtain the points identified by **X** in Fig. 67. If the pilot model
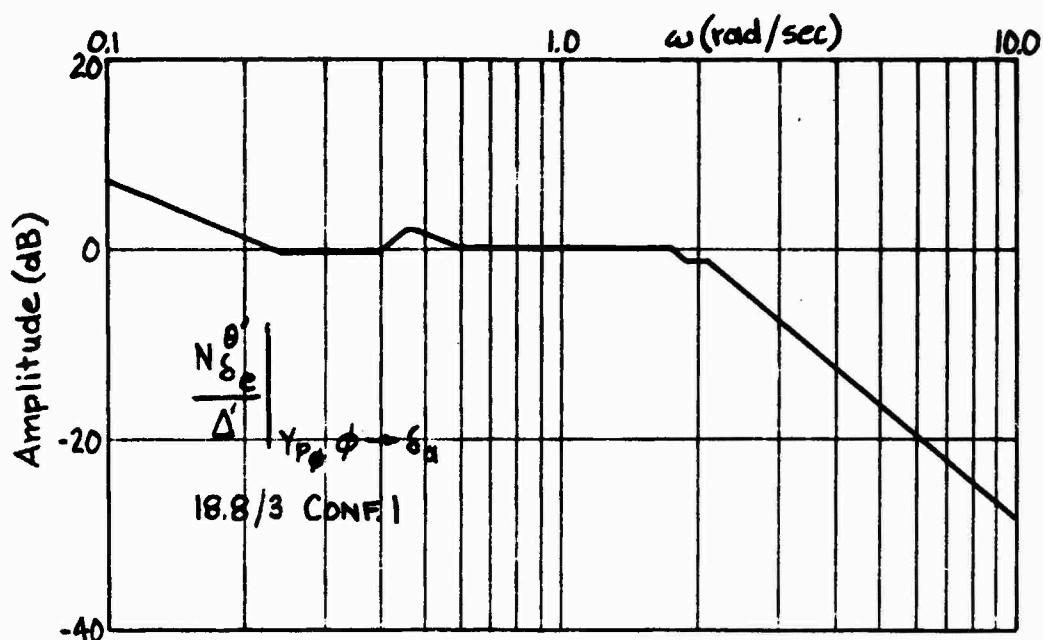
Figure 66. Bode Asymptote for Pitch Attitude with
Inner Roll Loop Closed

derived from the coupled, Configuration 1, case (Eq. 10) is applied, we obtain the points identified by $\odot$ in Fig. 67. The actual measured DFA data points for the multiloop $Y_p Y'_c$ are shown by $\Box$ in Fig. 67. Note that while all points are in close proximity the points obtained with the coupled pilot model match the measured data best at high frequencies while the points obtained with the uncoupled pilot model match best at low frequencies. It thus appears that pilot closure of the $\varphi \rightarrow \delta_a$ loop effectively decouples the lateral-longiutdinal dynamics to the point that a pilot model derived from an uncoupled case provides a somewhat better overall fit to the measured multiloop data. However, it is also apparent from Fig. 67 that the differences are minimal and therefore the
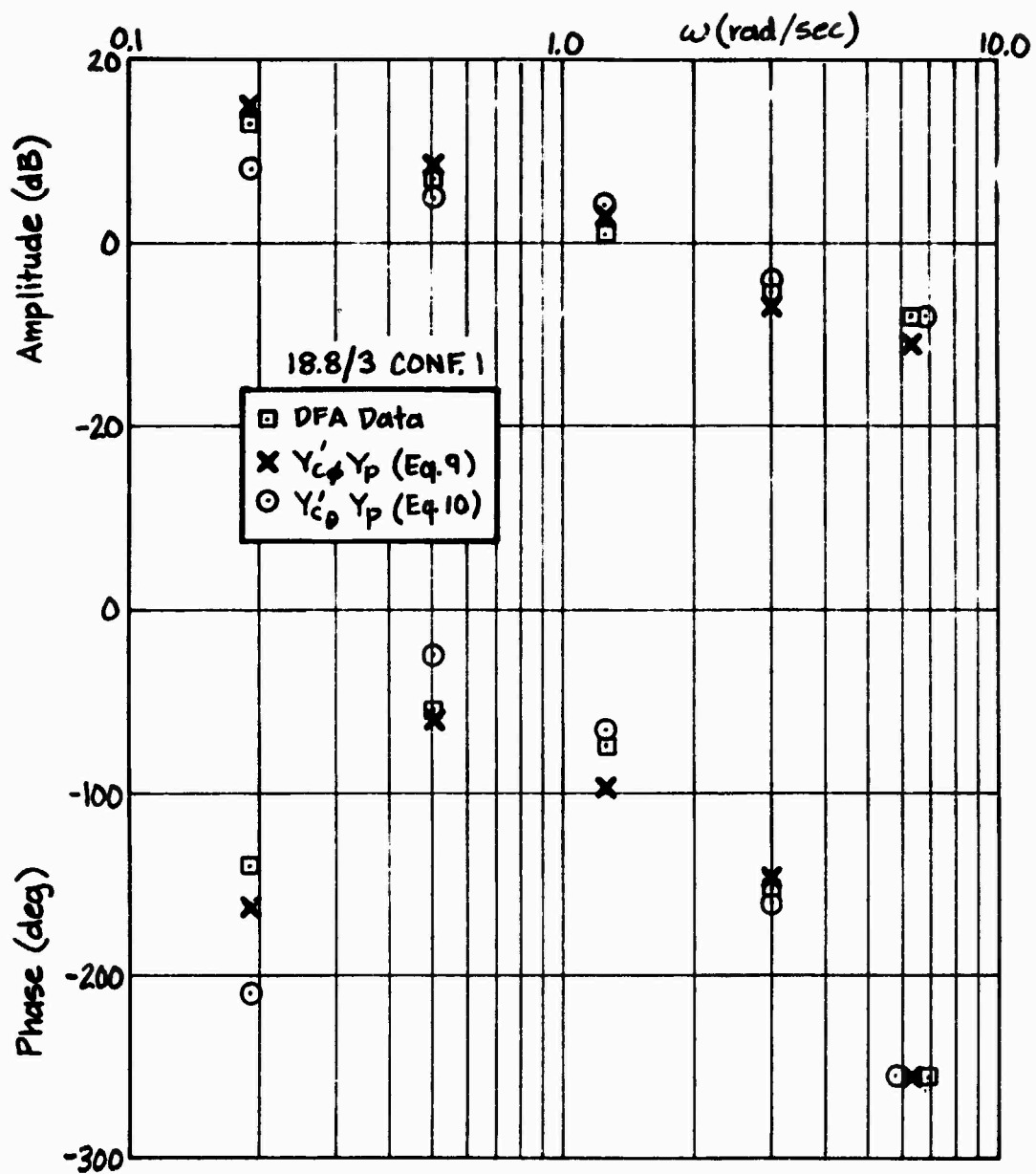
Figure 67. $Y_{c_\theta}^{\bullet} Y_p$ Comparisons, Pilot ML

single-loop analysis approach of the preceding Subsection B-1 remains valid. Further, since the roll closure only modifies the low-frequency pitch dynamics it may again be concluded that the closure sequence adopted by the pilot is pitch as inner (tightest) loop and roll as outer (lowest gain) loop.

C. HEADING PILOT MEASURES AND MODEL

The heading pilot measures were obtained by inserting the forcing function command as target bank angle but with the target free to displace in heading (i.e., $\psi_T = (g/U_o s)\varphi_T$, see Fig. 27 c). Repeat runs were made recording ψ_e and φ_e separately to facilitate modeling the dynamics of each loop. The heading and roll pilot models are thus subject to the following assumptions:

1. The run-to-run process is stationary.

2. The roll loop is closed as an inner loop to heading.

3. Coupling from lateral to longitudinal motion is sufficiently slight that the pitch closure does not alter the lateral dynamics appreciably.

The $Y_{p_\psi} Y'_{c_\psi}$ data points obtained from the ψ_e measures for five runs with the Configuration 1 (18.8°/3°) airframe dynamics are plotted in Fig. 68. It should be noted from the legend that these data reflect two different piloting techniques. In three runs the pilots were instructed to use only ailerons for lateral control. In two runs they were allowed to use rudder if they desired. Rudder was not considered beneficial in this task and was used sparingly, if at all. However, this appears partially responsible for the considerably greater scatter than obtained in the previous pitch and roll measurements. The rather surprising aspect of the data is the heading crossover above 1 rad/sec. The data are quite consistent in this factor. Past measures of heading control in landing or similar tasks have generally indicated crossovers considerably below 1 rad/sec. With the exception of three amplitude points at 3 rad/sec the data is in good agreement with the crossover model (slope 6 dB/octave).

The effective airframe Y'_{c_ψ} of Fig. 68 is dependent upon the inner roll loop closure. As previously indicated, the feedforward φ_c path of Fig. 27c was purposely opened to determine the effect of this path on overall loop dynamics as measured by ψ_e. The data points for Run 1102-18 of Fig. 68 reflect the absence of this bank angle cue and it is apparent that the
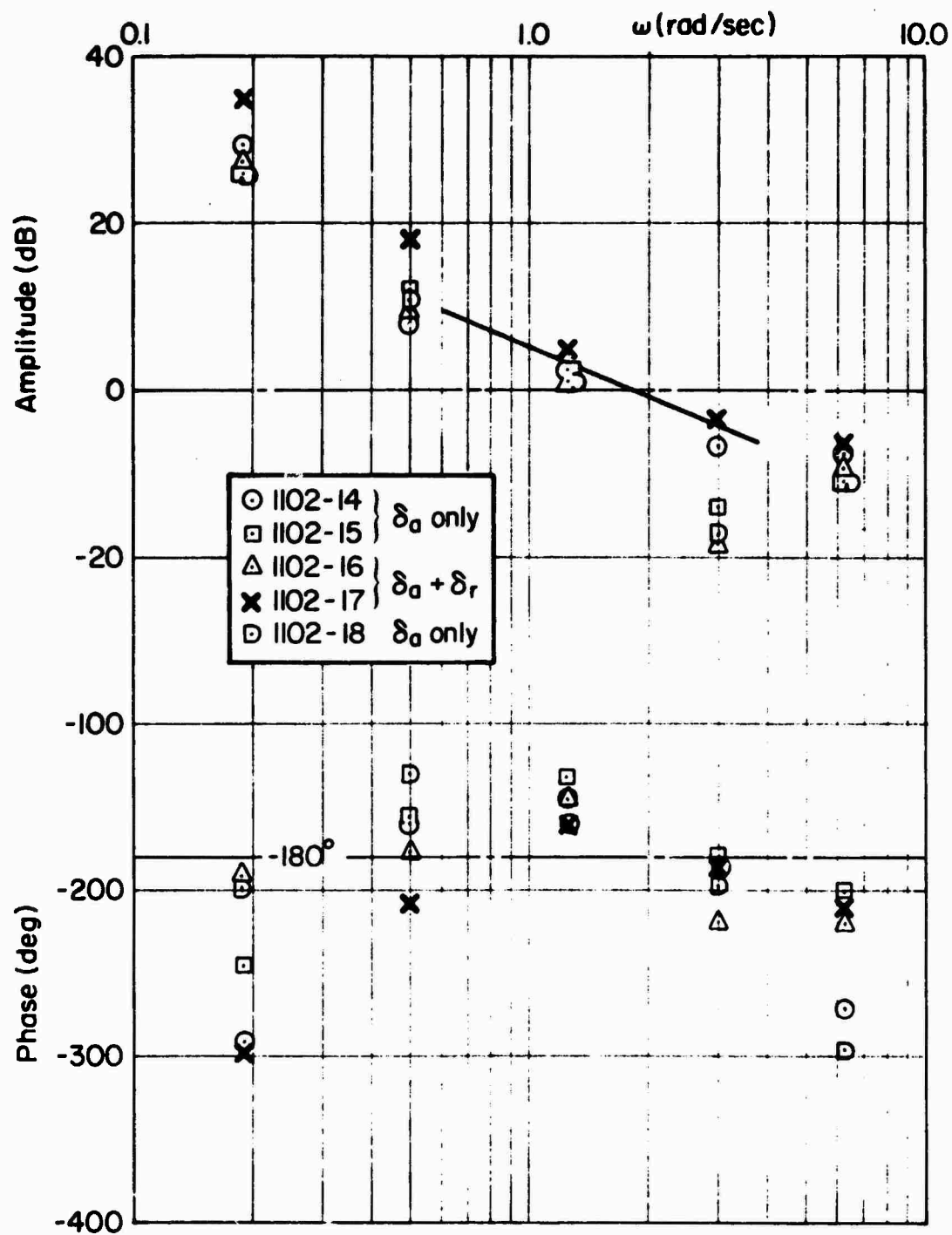
128

Figure 68. Measured $Y_{p_\psi} Y'_{c_\psi}$ with Inner φ Loop Closed

removal has little effect on the heading describing function data. It is therefore concluded that the pilot pays little attention to target bank angle during heading tracking. This is supported further by comparing the $Y_{p_\varphi} Y_c$ data points obtained from the φ_e/φ measures for the three loop (ψ, φ, θ) tracking task (Fig. 27c) with those for the two (φ, θ) loop task (Fig. 27a). The describing function data for these two cases, two runs each, are plotted in Fig. 69. The three-loop data indicate considerably less amplitude ratio at the lowest frequency and much less phase lag at the two lower frequencies. This is consistent with the pilot not tracking in roll when this is the inner loop. Therefore, it is not necessary to adopt the low-frequency lag-lead equalization which was central to the roll tracking task.

Based upon the comparison of data in Fig. 69, a simplified inner-loop roll pilot model was selected as shown in Eq. 13:

$$Y_{p_\varphi} = \frac{960(.6)}{[.3, 10](15)} e^{-.4s} \tag{13}$$

This reflects the first-order lead and third-order neuromuscular lags identified in Eq. 7 but the low-frequency lag-lead is eliminated and the gain is reduced by roughly a factor of four. The time delay has also been reduced slightly on the basis that it would be necessary for the pilot to reduce his high-frequency lags if the outer (ψ) loop is to be stable with a closure above 1 rad/sec. The resulting multiloop structure and dynamics are shown in Fig. 70. The open-loop, ψ/ψ_e, amplitude and phase plot for this loop structure is shown in Fig. 71. Also shown in Fig. 71 are the describing function data points of Fig. 68 shifted in amplitude to correspond to an outer loop $K_{p_\psi} = 0.625$. The derived model is considered to provide an excellent fit[*] to the data points measured during the simulation.

Again, this multiloop model reflects a minimum equalization, minimum effort, approach on the part of the pilot. Apparently, he is using the the inner loop primarily to damp the dutch roll nuisance mode. For example, the open-loop ζ_d is 0.296 whereas the closed inner loop $\zeta_d' = 0.38$. This decreases

---

[*]It is to be reemphasized that no attempt has been made here to model the low-frequency phase droop due to the "α effect."
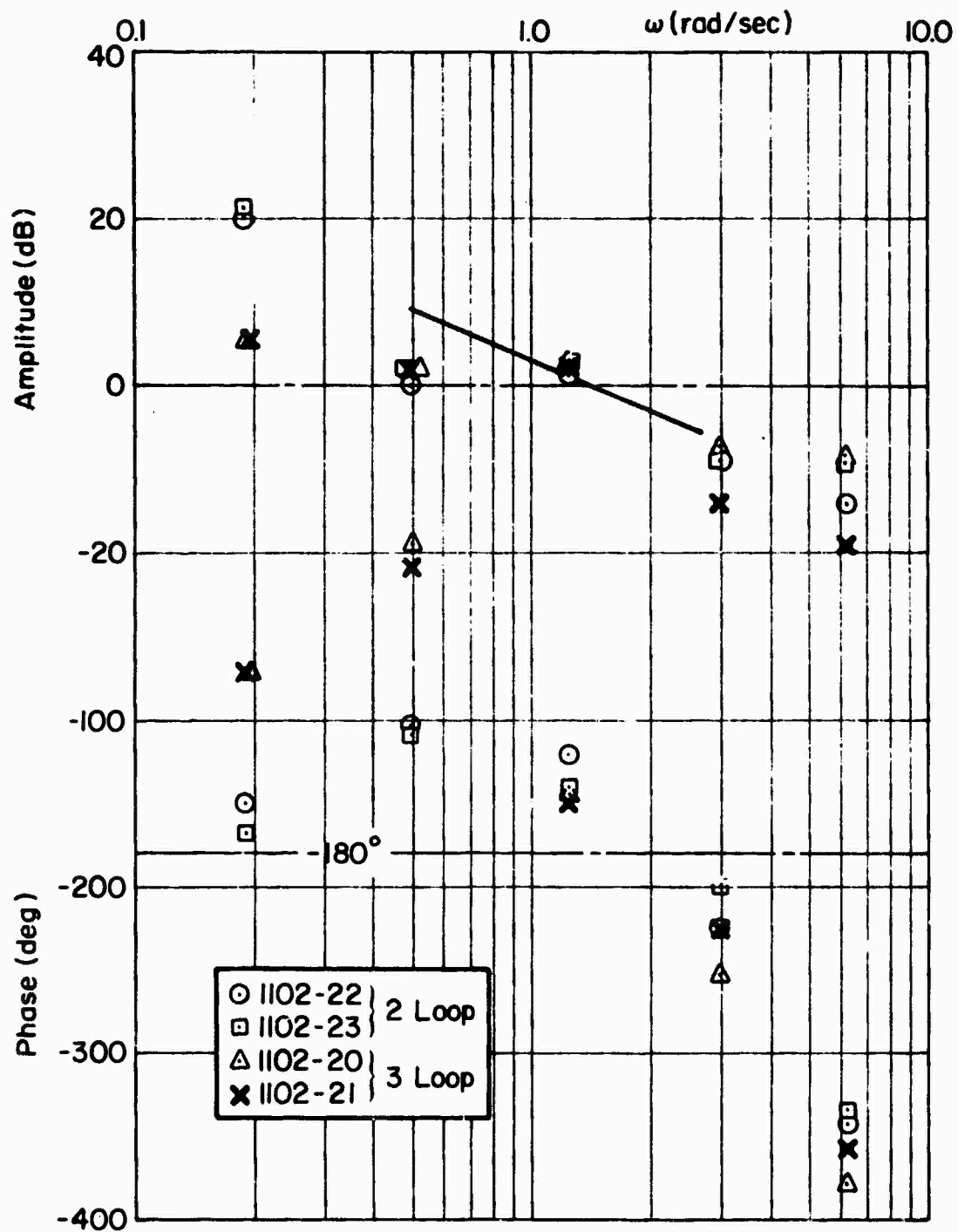
Figure 69. $Y_{p_\phi} Y_{c_\phi}$ Obtained from Describing Function Analyzer

Figure 70. Dynamic and Loop Structure for Heading Tracking Task Analysis
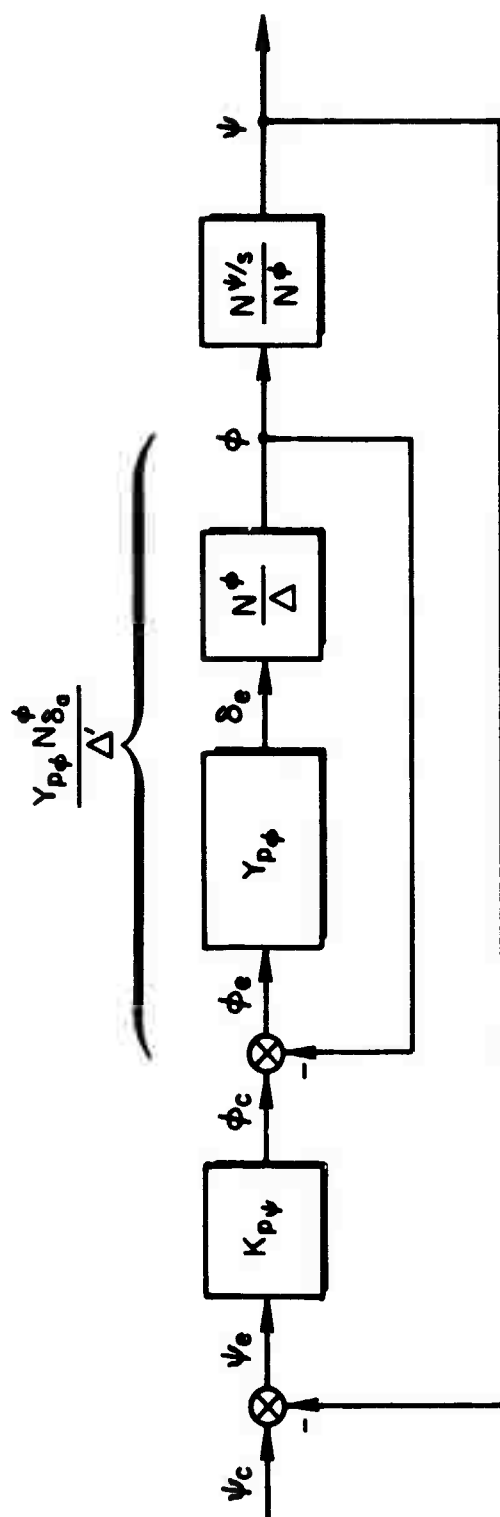
$N^\phi = .431 \; [.246, .56][.185, 1.92]$

$N^\psi = .031 \; (.438) \; [.358, .941][.197, 2.11]$

$\Delta = [.97, .238][.296, 1.03][.185, 1.96]$

$\Delta' = (2.409) \; [.352, .475][.173, 1.77][.113, 2.10][.268, 10.7][.964, 14.82]$
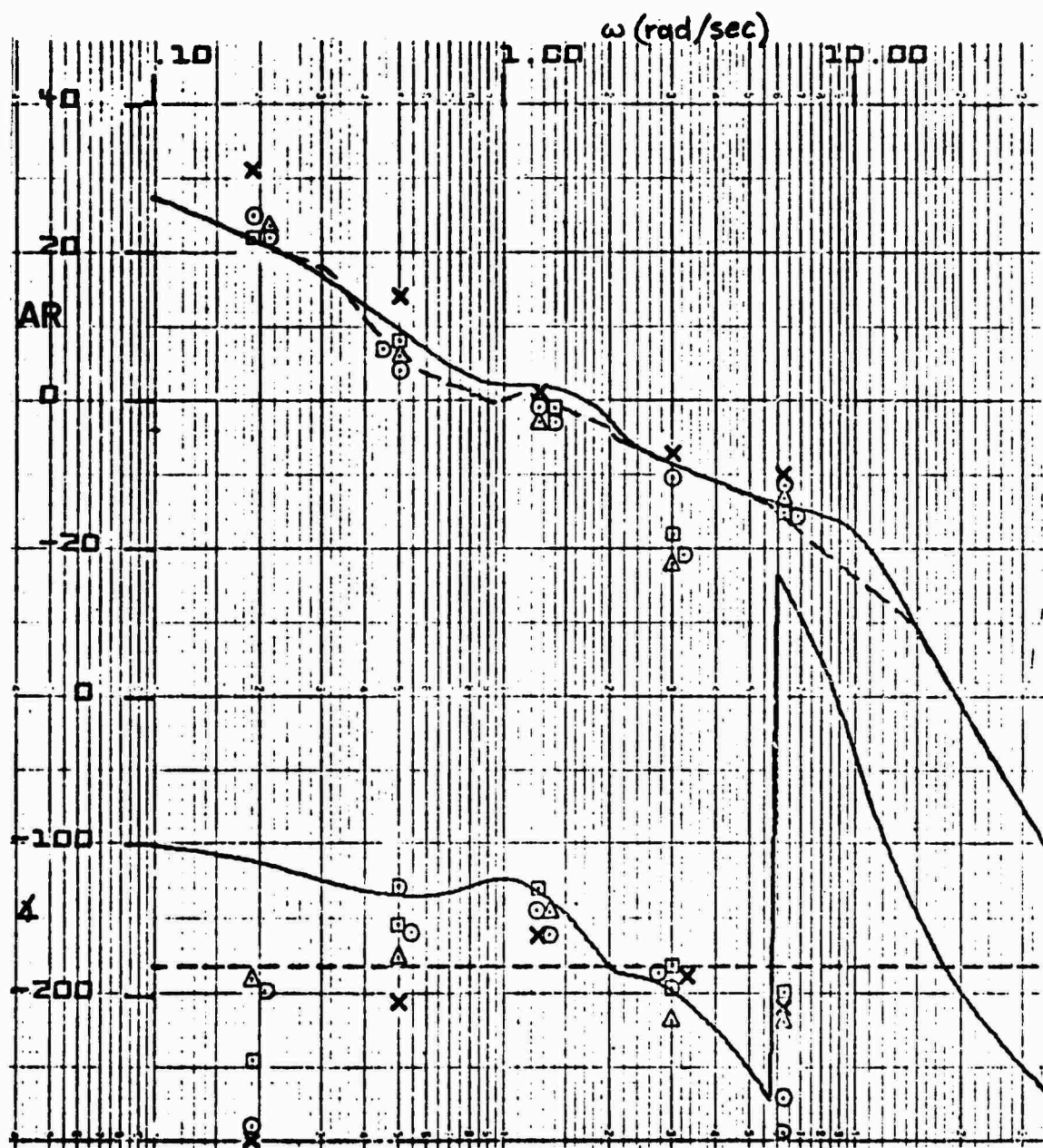
Figure 71. Open-Loop ψ/ψ_e with Inner Loop Closed

133

the amplitude peak at dutch roll sufficiently that the outer ψ loop can be closed tightly (above 1 rad/sec) without the necessity for additional equalization. The ψ loop with its high dc gain then provides good flight path control.

D. SUMMARY AND CONCLUSIONS

Multiloop, multi-input, multi-output pilot measurements have been made for an air-to-air tracking task with aircraft dynamics representative of impending stall/departure. These measures have allowed identification of the effect of impending stall/departure on pitch control, coupled versus uncoupled lateral-longitudinal airframe dynamics, and inner versus outer loop applications on pilot dynamic parameters.

The crossover model was found to apply in all loop closures, including multiloop situations, except when the controlled element exhibits a right half plane pole. In the latter case the crossover is achieved at an amplitude ratio slope somewhat less than 6 dB/octave.

The detailed pilot models obtained for the two-loop, coupled lateral-longitudinal airframe tracking task reflect the precision pilot model form except for the adoption of a second-order series lead in the pitch task. The presence (and degree) of coupling principally influences the low-frequency lag-lead equalization adopted by the pilot. This is adjusted within and between axes to effectively decouple the airframe motion with the least pilot effort (equalization).

Based upon the open-loop pitch airframe dynamics used here it would not be suspected that the pilot would adopt second-order lead equalization for either coupled or uncoupled cases. This apparently is a result of the requirement to prevent pitch (θ or α) overshoot which would trigger a departure. Thus, the pilot adopts equalization based on crossover, phase, and penalty criteria. While there are some previous pilot parameter measurement data which also reflect generation of second-order lead, these are insufficient to generate pilot rating functionals or to even predict the adoption of such equalization.

Considerably more data must be obtained before a paper pilot type model can be devised for the pre-departure flight regime. Most past effort has been

134

devoted to tasks and controlled elements where the airframe has relatively good dynamics, i.e., operation well within the nominal flight envelope, and concern is related to identification of the 3.5 boundary. This high-angle-of-attack task has involved operation at (if not beyond) the permissible flight envelope boundary with attendant airframe dynamics which have been shown in the previous sections to rate in the 6 to 9 region at best.

It was found in the heading tracking task that the pilot was not making use of target bank angle information in the manner usually professed by fighter pilots, i.e., match target bank. One possible explanation is that this technique is used mainly for gross maneuvers and that once in a precise tracking position the pilot switches to a "pointing" mode — which this simulation has shown can accomplish a heading crossover of greater than 1 rad/sec even with relatively poor lateral airframe dynamics. If the target were to make a sudden large bank angle change it is likely the pilot would immediately switch to a "match bank angle" mode to minimize either error or reacquisition time.

SECTION VI

CONCLUSIONS AND RECOMMENDATIONS

The foregoing analysis and simulation has traced the nose slice departure of t e A-7 aircraft through a chain of events which evolve from unsymmetric flight (directional mistrim or miscoordination in maneuvers). This results in sideslip and shed vorticies which give rise to aerodynamic moments, $N_\alpha^\prime$ and $\mathcal{L}_\alpha^\prime$. A nonlinear kinematic coupling also occurs between sideslip and yawing or rolling of the aircraft to give rise to pseudo-derivatives, Z_p and Z_r. These combined coupling effects result in a right half plane zero ($1/T_{\theta_3}$ or ω_θ) in the pitch-attitude-to-elevator numerator. Pitch attitude control by the pilot then drives the aircraft unstable. The instability starts as a first-order divergence in coupled lateral, directional, and longitudinal motion. However, pilot control via elevator initially restrains the longitudinal divergence so the motion appears mainly in the lateral-directional degrees-of-freedom.

This somewhat peculiar control-divergence phenomenon is analogous to the longitudinal divergence which occurs when an aircraft is on the "backside" of the thrust required curve. In the latter case the altitude numerator has a right half plane (non-minimum phase) zero and control of altitude via elevator causes a divergence. However, the divergence is not reflected in altitude (or flight path) but rather in speed.

A quasi-linearized five-degrees-of-freedom model containing the coupling terms $\mathcal{L}_\alpha^\prime$, $N_\alpha^\prime$, Z_p, and Z_r and with only six lateral-directional derivatives varied as a function of angle-of-attack and sideslip provided a good simulation of the A-7 high angle-of-attack and nose slice departure characteristics.

Based on the nine dynamic configurations examined, it is concluded that nose slice characteristics and pilot comments best relate to the longitudinal parameters $1/T_{\theta_3}$ and ω_θ. These are strongly influenced by the derivative $N_\alpha^\prime$. The conventional lateral parameters, $N_{\beta_{dyn}}$ and ω_φ, certainly contribute to, but are not the key factors in, the A-7 nose slice. However, it appears that when these lateral parameters become negative at the same time the longitudinal parameters are in the right half plane the rapidity and/or severity of nose slice departure is increased.

136

In the fixed base simulation the nose slice onset could only be detected when the target aircraft was in view. Pilot attempts to oppose nose slice lead to saturation of lateral-directional control. If system dynamics or control characteristics do not change appreciably as departure is approached, the lack of cues can induce the pilot to continue control activity until the departure is well developed and thus lead to a more severe departure. The configuration having the best lateral-directional characteristics but also the least changes in dynamics with α was downgraded severely because of inadequate warning. In this respect a steady (graceful) degradation in handling and a slow but firm nose slice provided the best warning and time to react.

The principal means of recovery is to open the pitch attitude loop, i.e., let go of the stick, at the first indication of nose slice. The use of lateral-directional control generally aggravates, rather than assists, recovery. One key to successful recovery with minimal pilot workload or compensation is that the aircraft be trimmed, stick force zero, at an angle-of-attack for which the lateral-phugoid and dutch roll are stable. Therefore, the open-loop parameter $N_{\beta_{dyn}}$ is a key factor in recovery.

Data and pilot ratings obtained for the stick release only recoveries probably relate mostly to 1 g, straight-ahead stall maneuvers. With few exceptions these involved minimum penetration into stall/departure, were readily recoverable control free, and received Cooper-Harper ratings of 3 to 6 from one pilot and 3 to 7 for the other (using stick push). Data and ratings obtained for all other types of recoveries (e.g., B, C, D) probably relate better to actual tracking and maneuvering situations in which inadvertent departure — or delay of departure — is encountered. These cases consistently resulted in Cooper-Harper ratings of 6 to 10. The very significant difference between these two sets of ratings may reflect actual flight situations in which stall and/or spin characteristics obtained from intentional entries (including application of pro-spin controls) tend to be considerably milder than those obtained from inadvertent entries.

The resulting pilot ratings could not be correlated with any single flying quality parameter. The departure characteristics were most dependent upon closed loop (i.e., pitch numerator) parameters with some influence

137

from open loop parameters. Where recovery was possible it was most dependent upon airframe open loop parameters (i.e., denominator and stick trim) but the possibility of successful recovery was also highly dependent upon pilot technique, agressiveness, sensitivity to cues, etc.

All configurations investigated here exhibited good pitch control and response characteristics. If a configuration exhibiting pitch-up, loss of longitudinal control effectiveness, or any other impairment of longitudinal control, were to be employed the results might be considerably different from those obtained here.

The results of this study indicated the conventional closed-loop pilot/ vehicle analysis approach, while appropriate for pre-departure, is not appropriate for actual departure and recovery. Immediately prior to departure the lateral-directional control (if employed at all) tended toward steady or trim type application against the motion of the nose slice. Following departure the preferred method of recovery was to release all controls. Thus, the pilot provided no inputs and the recovery was achieved through open-loop, airframe-alone stability and damping. Again, if control was applied during the recovery, the preferred technique was to hold constant forward stick to assure decrease in α and to prevent pitch up due to inertia coupling. As the aircraft motion subsided the stick was returned to neutral. Thus a closed loop pilot model, per se, does not appear appropriate for departure/recovery application.

In the pre-departure phase where closed-loop considerations are valid, it was found that the pilot adopts a second order lead in pitch attitude control — apparently in an attempt to cancel short period pitch attitude excursions which might trigger departure. This second-order complex lead generation has been observed before; however, there are insufficient pilot rating data to establish a functional. The vast amount of data obtained for first order lead generation is not applicable. Much more data is required from departure type conditions before trends can be established between pilot parameters, pilot ratings, and performance measures.

A key problem with ratings exists because loss-of-control is involved. That is, accomplishment of the primary task, whatever it may be, has resulted in the aircraft approaching stall/departure. If the task is

138

pursued, it presumably will result in departure — loss of control. Departure prevention then requires abandonment of the primary task and shifting full priority to safety of flight. Thus, Level 3 flying qualities are involved — and, in fact, the question is establishment of the Level 3 boundary, i.e., loss of control. On the Cooper-Harper scale this is the boundary between 9 and 10 (there is no 9.5). If an airplane will depart, then there is no question regarding the existence of the Cooper-Harper boundary, but merely a question of how much of the potential flight envelope must be traded for flight safety. Thus a mission performance, usable load factor, flight safety, or some related index becomes paramount.

In a limited investigation of wing-rock, an attempt to change the departure characteristic of the A-7 aircraft from nose slice to wing rock proved partially sucessful. Scaling of five key stability derivatives ($\mathcal{L}_r'$, $\mathcal{L}_\beta'$, N_α', N_β', and M_β') to resemble those of the F-4 did result in an oscillatory characteristic; however, it did not have the predominate roll characteristic of wing rock.

This investigation has only been a first cut at a most complex problem area. However, it has yielded considerable insight to the nose slice phenomenon. It is recommended that the approach be continued and expanded in a number of ways:

1. Investigate a larger population of aircraft to validate and/or refine the key parameters identified here.

2. Develop literal expression for the coupled lateral-longitudinal transfer function parameters which result from unsymmetric flight.

3. Investigate possible limits of (or for) rudder maneuvering at high angle-of-attack.

4. Investigate the influence of single- and multi-axis, high-gain, high-authority augmentation systems.

5. Expand the pilot describing function data base for these coupled, limit-of-control situations.

6. Expand the simulation to six degrees-of-freedom and investigate the influence of additional aerodynamic nonlinearities (e.g., C_{L_α}, C_{m_q}, etc.).

It would also be highly desirable to investigate the influence of motion cues on pilot detection of departure onset and assessment of departure-recovery dynamic characteristics. But unfortunately the rapid large yaw and lateral acceleration of nose slice may not be compatible with practical displacement limits of most moving base simulators. The motion washout necessary to prevent hitting displacement limits might negate completely the desired acceleration cue.

REFERENCES

1. Weissman, Robert, _Development of Design Criteria for Predicting Departure Characteristics and Spin Susceptibility of Fighter Type Aircraft_, AIAA Paper No. 72-984, Sept. 1972.

2. Greer, H. Douglas, _Summary of Directional Divergence Characteristics of Several High Performance Aircraft Configurations_, NASA TN D-6993, Nov. 1972.

3. Anglin, Ernie L., _Static Force Tests of a Model of a Twin-Jet Fighter Airplane for Angles of Attack from -10 Deg to 110 Deg and Sideslip Angles from -40 Deg to 40 Deg_, NASA TN D-6425, Aug. 1971.

4. Bihrle, William Jr., and Arthur C. Heyman, _The Spin Behavior of Aircraft_, Final Report, Vols. I through IV, Grumman Aircraft, GAEC Report No. 394-68-1, Dec. 1967.

5. Moul, M. T., and J. W. Paulson, _Dynamic Lateral Behavior of High-Performance Aircraft_, NASA RM L58E16, Aug. 1958.

6. Ashkenas, I. L., H. R. Jex, and D. T. McRuer, _Pilot-Induced Oscillations: Their Cause and Analysis_, Systems Technology, Inc., TR-239-2, June 1964.

7. Anderson, R. O., _A New Approach to the Specification and Evaluation of Flying Qualities_, AFFDL-TR-69-120, June 1970.

8. Anderson, R. O., A. J. Connors, and J. D. Dillow, _Paper Pilot Ponders Pitch_, AFFDL/FGC-TM-70-1, Nov. 1970.

9. Teper, G. L., _An Assessment of the Paper Pilot — An Analytical Approach to the Specification and Evaluation of Flying Qualities_, Systems Technology, Inc. TR-1006-1, Nov. 1971.

10. McRuer, Duane T., Irving L. Ashkenas, and C. L. Guerre, _A Systems Analysis View of Longitudinal Flying Qualities_, WADD TR-60-43, Jan. 1960.

11. Shirley, Richard S., _Motion Cues in Man-Vehicle Control_, MIT, MVT-68-1, Jan. 1968.

12. MIL-F-8785B(ASG), _Flying Qualities of Piloted Airplanes_, 7 Aug. 1969.

13. Harper, R. P. Jr., and G. E. Cooper, _A Revised Pilot Rating Scale for the Evaluation of Handling Qualities_, AGARD Specialists Meeting on Stability and Control, Cambridge, England, Sept. 1966.

14. Johnston, D. E., R. L. Stapleford, G. L. Teper, and G. Chuck, _Investigation of Improved Weapon Delivery by Means of Aircraft Handling Quality Modifications_, Systems Technology, Inc., TR-173-1, Apr. 1969.

15. Naylor, J. L., and R. Jones, General Mathematical Investigation of the Stability of the Motion of an Aeroplane, (V) Numerical Illustrations in the Case of Side-slipping Without Turning, Advisory Committee for Aeronautics, R and M No. 258, Sept. 1916.

16. Porter, R. F., and J. P. Loomis, "Examination of an Aerodynamic Coupling Phenomenon," J. of Aircraft, Vol. 2, No. 6, Nov.-Dec. 1965, pp. 553-556.

17. Shields, M. E., A. W. Shaw, and J. D. Louthan, "VAC Experience in the Stall/Post-Stall and Spin Flight Regimes," Proceedings, Stall/Post-Stall/Spin Symposium, Wright-Patterson AFB, Dec. 1971, pp. I-1 through I-23.

18. Bell, M. A., and J. D. Etheridge, A-7 Accelerated Stall Departure Study, Vought Aeronautics Div., LTV, Rept. No. 2-53310/IR-5598, Apr. 1971.

19. Wykes, J. H., An Analytical Study of the Dynamics of Spinning Aircraft, Part III: Calculated and Flight Test Spin Characteristics of an F-100F with Strakes, WADC TR-58-381, Feb. 1960.

20. Chambers, Joseph R., and Ernie L. Anglin, Analysis of Lateral-Directional Stability Characteristics of a Twin-Jet Fighter Airplane at High Angles of Attack, NASA TN D-5361, Aug. 1969.

21. Grafton, Sue B., and Charles E. Libbey, Dynamic Stability Derivatives of a Twin-Jet Fighter Model for Angeles of Attack from -10 Deg to 110 Deg, NASA TN D-6091, Jan. 1971.

22. Hall, W. E. Jr., Identification of Aircraft Stability Derivatives for the High Angle of Attack Regime, Systems Control, Inc., Tech. Rept. No. 1, June 1973.

23. Carleton, David L., Stability and Control Derivatives for the F-4E Aircraft, FTC-TD-69-9, Sept. 1969.

24. Unpublished flight traces, McDonnell Douglas Co., St. Louis, Mo., 1973.

25. Hoey, Robert G., and Chris Nagy, A-7 Stall/Departure Simulation, AFFTC, Flight Test Technology Branch, Office Memo, Apr. 1972.

26. Allen, R. W., and H. R. Jex, "A Simple Fourier Analysis Technique for Measuring the Dynamic Response of Manual Control System," IEEE Trans. on Systems, Man, and Cybernetics, Vol. SMC-2, No. 5, Nov. 1972, pp. 638-643.

27. Peters, Richard A., and R. Wade Allen, Operation Manual, Describing Function Analyzer, Model 1003 Serial 1001, Systems Technology, Inc., WP-406-2, Oct. 1970.

28. McRuer, Duane, "The Development of Pilot-in-the-Loop Analysis," J. Aircraft, Vol. 10, No. 9, Sept. 1973, pp. 515-524.

29. McRuer, Duane T., and Ezra S. Krendel, Mathematical Models of Human Pilot Behavior, AGARDograph No. 188, Jan. 1974.

30. McRuer, Duane, Dunstan Graham, Ezra Krendel, and William Reisener, Jr., Human Pilot Dynamics in Compensatory Systems — Theory, Models, and Experiments with Controlled Element and Forcing Function Variations, AFFDL-TR-65-15, July 1965.

31. Hogge, J. R., and R. E. Magdaleno, Describing Function Measuresments for High Angle of Attack, Systems Technology, Inc., WP-1033-2, May 1974.